

Manuscript Details

| | |
|--------------------------|--|
| Manuscript number | EARTH_2018_481 |
| Title | Intraplate magmatism at a convergent plate boundary, the case of the Cenozoic northern Adria magmatism |
| Article type | Review Article |

Abstract

The complex European–Adria geodynamic framework, which led to the formation of the Alpine belt, is considered responsible for the orogenic magmatism that occurred in the Central Alps along the Periadriatic/Insubric Line (late Eocene–early Oligocene) and the anorogenic magmatism that occurred in the Southeastern Alps (late Paleocene–early Miocene). While subduction–related magmatic activities are expected near convergent margins, the presence of the intraplate–related magmatic products is still puzzling. Therefore, in this work new geochemical and geochronological data of magmatic products from the Veneto Volcanic Province (VVP, north–east Italy) are provided in order to constrain the Cenozoic intraplate magmatism of the Southeastern Alps. The VVP is formed by dominant basic–ultrabasic (from nephelinites to tholeiites) magmatic products and by localized acid (latitic, trachytic, and rhyolitic) volcanic and sub–volcanic bodies. Trace element patterns and ratios suggest that the mantle source of the basanitic magma types was a phlogopite–bearing garnet lherzolite, while those of the tholeiitic magma types was an anhydrous (i.e., without residual phlogopite and amphibole) garnet lherzolite. All the basic–ultrabasic VVP magmatic products exhibit enrichments in Ba, Sr, and P, indicating the mantle sources could be metasomatized by carbonatitic melts. According to the biostratigraphic records and our new $^{40}\text{Ar}/^{39}\text{Ar}$ ages, VVP eruptions occurred in several pulses, reflecting the extensional phases experienced by the Eastern Alpine domain. The volcanism started in the late Paleocene in the western sector of the VVP where activity was widespread also during the Eocene (45.21 ± 0.11 Ma – 38.73 ± 0.44 Ma). In the eastern sector eruptions took place only in the early Oligocene (32.35 ± 0.09 Ma – 32.09 ± 0.29 Ma) and in the early Miocene (~ 22 – 23 Ma). Previously, as suggested for neighboring orogenic magmatism, also the anorogenic magmatic activities were interpreted as resulting from mantle upwellings through slab window(s) following the European slab break–off occurred ~ 35 Ma. However, considering i) new tomographic images evidencing a continuous subvertical slab beneath the Central Alps, and ii) the onset of magmatic activity in the VVP in the late Paleocene (i.e., before the slab break–off) and its continuation until Miocene, we propose an alternative geodynamic scenario to explain the anorogenic magmatism. The westward rollback of the European slab caused the retreat and steepening of the sinking plate. As a consequence, the sub–slab mantle material escaped and upwelled from the front of the slab and created a poloidal mantle flow. The latter induced the breakdown of carbonates in calcareous metasediments and carbonated metabasics within the subducting oceanic slab, providing carbonatitic melts, which could be responsible for the metasomatism of the VVP mantle sources. After that, the poloidal mantle flow also induced i) the extensional deformation in the overriding Adria microplate and ii) the decompressional melting of VVP mantle sources, iii) triggering the magmatism with intraplate affinity. During these processes, the Adria microplate also rotated counterclockwise, allowing the poloidal mantle flow to affect different portions of the overlying lithosphere and generating up to five eruptive centers within the VVP.

| | |
|---|--|
| Keywords | Intraplate magmatism; $^{40}\text{Ar}/^{39}\text{Ar}$ geochronology; Poloidal mantle flow; Southeastern Alps; Veneto Volcanic Province |
| Corresponding Author | Costanza Bonadiman |
| Corresponding Author's Institution | University of Ferrara, Department of Physics and Earth Sciences |
| Order of Authors | Valentina Brombin, Costanza Bonadiman, Fred Jourdan, Guido Roghi, Massimo Coltorti, Laura E. Webb, Sara Callegaro, Giuliano Bellieni, Giampaolo De Vecchi, Roberto Sedeà, Andrea Marzoli |
| Suggested reviewers | Gilles Chazot, Marco Brenna, Maurizio Mazzucchelli, Alberto Zanetti |

Submission Files Included in this PDF

File Name [File Type]

Brombin et al-cover letter.docx [Cover Letter]

Brombin et al. _ abstract.docx [Abstract]

Brombin et al-manuscript.docx [Manuscript File]

Fig. 01.jpg [Figure]

Fig. 02.jpg [Figure]

Fig. 03.jpg [Figure]

Fig. 04.jpg [Figure]

Fig. 05a.jpg [Figure]

Fig. 05b.jpg [Figure]

Fig. 06.jpg [Figure]

Fig. 07.jpg [Figure]

Fig. 08.jpg [Figure]

Fig. 09.jpg [Figure]

Fig. 10.jpg [Figure]

Brombin_On-line Supplementary material.docx [Supporting File]

To view all the submission files, including those not included in the PDF, click on the manuscript title on your EVISE Homepage, then click 'Download zip file'.

Research Data Related to this Submission

There are no linked research data sets for this submission. The following reason is given:
Data will be made available on request

Dear Editor,

Please find enclosed the manuscript: **Intraplate magmatism at a convergent plate boundary, the case of the Cenozoic northern Adria magmatism** by Valentina Brombin, Costanza Bonadiman, Fred Jourdan, Guido Roghi, Massimo Coltorti, Laura E. Webb, Sara Callegaro, Giuliano Bellieni, Giampaolo De Vecchi, Roberto Sedeà, and Andrea Marzoli for a potential publication in Earth-Science Reviews.

The manuscript presents new geochemical and geochronological data of Cenozoic intraplate-related ultrabasic, basic, and acid magmatic products from the Veneto Volcanic Province, a magmatic province of the Southeastern Alpine domain (north-east Italy). Such products were investigated in order to explain the occurrence of magmatic products with anorogenic signature in the Southeastern Alps domain, during the Alpine orogenesis.

The new major and trace element geochemical data of the Southeastern Alps magmatic products allowed to constrain the potential nature and evolution of their mantle source(s), while the combination of the biostratigraphic data and the new high-resolution $^{40}\text{Ar}/^{39}\text{Ar}$ ages allowed to reconstruct the temporal evolution of the Veneto Volcanic Province magmatism.

Finally, both geochemical and geochronological data were used to review the intriguing geodynamic scenario of the Alpine domain, to explain the occurrence of anorogenic magmatic events in a subduction-dominated geological setting.

For all these aspects, we believe this work may be considered for publication with Earth-Science Reviews. This manuscript is an original work, which has not been published and is not under consideration for publication elsewhere.

All the authors have seen the manuscript and agree about its submission to Earth-Science Reviews.

Even if we have no particular preferences about potential reviewers, we suggest the following scientists: Maurizio Muzzucchelli (University of Modena and Reggio Emilia, Italy); Marco

Brenna (Univesity of Otago, New Zealand); Gilles Chazot (Université de Bretagne Occidentale, UBO, France); Alberto Zanetti (IGG-CNR, Pavia, Italy).

Thank you very much for your consideration and handling.

For the authors,

Costanza Bonadiman

A handwritten signature in cursive script, reading "Costanza Bonadiman". The signature is written in black ink and is positioned below the printed name. There is a horizontal line above the signature, likely indicating where the signature was placed on the original document.

Intraplate magmatism at a convergent plate boundary, the case of the Cenozoic northern Adria magmatism

Valentina Brombin^a, Costanza Bonadiman^{a*}, Fred Jourdan^b, Guido Roghi^c, Massimo Coltorti^a,
Laura E. Webb^d, Sara Callegaro^e, Giuliano Bellieni^f, Giampaolo De Vecchi^f, Roberto Sedeaf^f
Andrea Marzoli^{c,f}

^a *Dipartimento di Fisica e Scienze della Terra, Università di Ferrara, Italy*

^b *Western Australian Argon Isotope Facility, School of Earth and Planetary Sciences & JdL Centre, Curtin University, Perth, Western Australia, Australia;*

^c *Istituto di Geoscienze e Georisorse, CNR, Padova, Italy*

^d *Department of Geology, University of Vermont, Vermont, USA;*

^e *Centre for Earth Evolution and Dynamics, University of Oslo, Norway;*

^f *Dipartimento di Geoscienze, Università di Padova, Italy*

* Corresponding author: bdc@unife.it

ABSTRACT

The complex European–Adria geodynamic framework, which led to the formation of the Alpine belt, is considered responsible for the orogenic magmatism that occurred in the Central Alps along the Periadriatic/Insubric Line (late Eocene–early Oligocene) and the anorogenic magmatism that occurred in the Southeastern Alps (late Paleocene–early Miocene). While subduction–related magmatic activities are expected near convergent margins, the presence of the intraplate–related magmatic products is still puzzling. Therefore, in this work new geochemical and geochronological data of magmatic products from the Veneto Volcanic Province (VVP, north–east Italy) are provided in order to constrain the Cenozoic intraplate magmatism of the Southeastern Alps. The VVP is formed by dominant basic–ultrabasic (from nephelinites to tholeiites) magmatic products and by localized acid (latitic, trachytic, and rhyolitic) volcanic and sub–volcanic bodies. Trace element patterns and ratios suggest that the mantle source of the basanitic magma types was a phlogopite–bearing garnet lherzolite, while those of the tholeiitic magma types was an anhydrous (i.e., without residual phlogopite and amphibole) garnet lherzolite. All the basic–ultrabasic VVP magmatic products exhibit enrichments in Ba, Sr, and P, indicating the mantle sources could be metasomatized by carbonatitic melts. According to the biostratigraphic records and our new $^{40}\text{Ar}/^{39}\text{Ar}$ ages, VVP eruptions occurred in several pulses, reflecting the extensional phases experienced by the Eastern Alpine domain. The volcanism started in the late Paleocene in the western sector of the VVP where activity was widespread also during the Eocene (45.21 ± 0.11 Ma – 38.73 ± 0.44 Ma). In the eastern sector eruptions took place only in the early Oligocene (32.35 ± 0.09 Ma – 32.09 ± 0.29 Ma) and in the early Miocene (~ 22 – 23 Ma). Previously, as suggested for neighboring orogenic magmatism, also the anorogenic magmatic activities were interpreted as resulting from mantle upwellings through slab window(s) following the European slab break–off occurred ~ 35 Ma. However, considering i) new tomographic images evidencing a continuous subvertical slab beneath the Central Alps, and ii) the onset of magmatic activity in the VVP in the late Paleocene (i.e., before the slab break–off) and its continuation until Miocene, we propose an alternative geodynamic scenario to explain the anorogenic magmatism. The westward rollback of the European slab caused the retreat and steepening of the sinking plate. As a consequence, the sub–slab mantle material escaped and upwelled from the front of the slab and created a poloidal mantle flow. The latter induced the breakdown of carbonates in calcareous metasediments and carbonated metabasics within the subducting oceanic slab, providing

carbonatitic melts, which could be responsible for the metasomatism of the VVP mantle sources. After that, the poloidal mantle flow also induced i) the extensional deformation in the overriding Adria microplate and ii) the decompressional melting of VVP mantle sources, iii) triggering the magmatism with intraplate affinity. During these processes, the Adria microplate also rotated counterclockwise, allowing the poloidal mantle flow to affect different portions of the overlying lithosphere and generating up to five eruptive centers within the VVP.

1
2
3 1 **Intraplate magmatism at a convergent plate boundary, the case of the Cenozoic northern Adria**
4
5 2 **magmatism**
6
7
8 3

9
10 4 Valentina Brombin^a, Costanza Bonadiman^{a*}, Fred Jourdan^b, Guido Roghi^c, Massimo Coltorti^a,
11
12 5 Laura E. Webb^d, Sara Callegaro^e, Giuliano Bellieni^f, Giampaolo De Vecchi^f, Roberto Sedeaf^f
13
14 6 Andrea Marzoli^{c,f}

15
16 7 *^a Dipartimento di Fisica e Scienze della Terra, Università di Ferrara, Italy*

17
18 8 *^b Western Australian Argon Isotope Facility, School of Earth and Planetary Sciences & JdL Centre,*
19
20 9 *Curtin University, Perth, Western Australia, Australia;*

21
22 10 *^c Istituto di Geoscienze e Georisorse, CNR, Padova, Italy*

23
24 11 *^d Department of Geology, University of Vermont, Vermont, USA;*

25
26 12 *^e Centre for Earth Evolution and Dynamics, University of Oslo, Norway;*

27
28 13 *^f Dipartimento di Geoscienze, Università di Padova, Italy*

29
30
31 14

32
33 15 * Corresponding author: bdc@unife.it
34
35
36
37
38
39
40
41
42
43
44
45
46
47
48
49
50
51
52
53
54
55
56
57
58
59
60

61
62
63 **16 ABSTRACT**
64

65 17 The complex European–Adria geodynamic framework, which led to the formation of the Alpine belt,
66 18 is considered responsible for the orogenic magmatism that occurred in the Central Alps along the
67 19 Periadriatic/Insubric Line (late Eocene–early Oligocene) and the anorogenic magmatism that
68 20 occurred in the Southeastern Alps (late Paleocene–early Miocene). While subduction–related
69 21 magmatic activities are expected near convergent margins, the presence of the intraplate–related
70 22 magmatic products is still puzzling. Therefore, in this work new geochemical and geochronological
71 23 data of magmatic products from the Veneto Volcanic Province (VVP, north–east Italy) are provided
72 24 in order to constrain the Cenozoic intraplate magmatism of the Southeastern Alps. The VVP is formed
73 25 by dominant basic–ultrabasic (from nephelinites to tholeiites) magmatic products and by localized
74 26 acid (latitic, trachytic, and rhyolitic) volcanic and sub–volcanic bodies. Trace element patterns and
75 27 ratios suggest that the mantle source of the basanitic magma types was a phlogopite–bearing garnet
76 28 lherzolite, while those of the tholeiitic magma types was an anhydrous (i.e., without residual
77 29 phlogopite and amphibole) garnet lherzolite. All the basic–ultrabasic VVP magmatic products exhibit
78 30 enrichments in Ba, Sr, and P, indicating the mantle sources could be metasomatized by carbonatitic
79 31 melts.

80 32 According to the biostratigraphic records and our new $^{40}\text{Ar}/^{39}\text{Ar}$ ages, VVP eruptions occurred in
81 33 several pulses, reflecting the extensional phases experienced by the Eastern Alpine domain. The
82 34 volcanism started in the late Paleocene in the western sector of the VVP where activity was
83 35 widespread also during the Eocene (45.21 ± 0.11 Ma – 38.73 ± 0.44 Ma). In the eastern sector
84 36 eruptions took place only in the early Oligocene (32.35 ± 0.09 Ma – 32.09 ± 0.29 Ma) and in the early
85 37 Miocene ($\sim 22 - 23$ Ma).

86 38 Previously, as suggested for neighboring orogenic magmatism, also the anorogenic magmatic
87 39 activities were interpreted as resulting from mantle upwellings through slab window(s) following the
88 40 European slab break–off occurred ~ 35 Ma. However, considering i) new tomographic images
89 41 evidencing a continuous subvertical slab beneath the Central Alps, and ii) the onset of magmatic
90
91
92
93
94
95
96
97
98
99
100
101
102
103
104
105
106
107
108
109
110
111
112
113
114
115
116
117
118
119
120

121
122
123 42 activity in the VVP in the late Paleocene (i.e., before the slab break-off) and its continuation until
124
125 43 Miocene, we propose an alternative geodynamic scenario to explain the anorogenic magmatism. The
126
127 44 westward rollback of the European slab caused the retreat and steepening of the sinking plate. As a
128
129
130 45 consequence, the sub-slab mantle material escaped and upwelled from the front of the slab and
131
132 46 created a poloidal mantle flow. The latter induced the breakdown of carbonates in calcareous
133
134 47 metasediments and carbonated metabasics within the subducting oceanic slab, providing carbonatitic
135
136 48 melts, which could be responsible for the metasomatism of the VVP mantle sources. After that, the
137
138 49 poloidal mantle flow also induced i) the extensional deformation in the overriding Adria microplate
139
140 50 and ii) the decompressional melting of VVP mantle sources, iii) triggering the magmatism with
141
142 51 intraplate affinity. During these processes, the Adria microplate also rotated counterclockwise,
143
144 52 allowing the poloidal mantle flow to affect different portions of the overlying lithosphere and
145
146
147 53 generating up to five eruptive centers within the VVP.
148

149 54

150
151 55 **KEYWORDS**

152
153 56 Intraplate magmatism; $^{40}\text{Ar}/^{39}\text{Ar}$ geochronology; Poloidal mantle flow; Southeastern Alps; Veneto
154
155 57 Volcanic Province
156

121
122
123
124
125
126
127
128
129
130
131
132
133
134
135
136
137
138
139
140
141
142
143
144
145
146
147
148
149
150
151
152
153
154
155
156
157
158
159
160
161
162
163
164
165
166
167
168
169
170
171
172
173
174
175
176
177
178
179
180

181
182
183 **58 1. INTRODUCTION**
184

185 59 Synchronous orogenic (or subduction-related) and anorogenic (or intraplate-like) magmatic events
186
187 60 can occur near subductive zones (*e.g.*, Okete–Alexandra Volcanic Province in New Zealand, Briggs
188
189 61 and McDonough 1990; Cook et al., 2005; Faccini et al., 2018; north–west Turkey, Aldanmaz et al.,
190
191 2006; Perşani volcanic field and South Harghita, in south-east Carpathian, Seghedi et al., 2011;
192 62 Faccini et al., 2018; Kurdistan Province, western Iran, Allen et al., 2013; Trans–Mexican Volcanic
193
194 63 Belt, Neumann et al., 2016; Payenia Volcanic Province in Argentina, Pallares et al., 2016). Calc–
195
196 64 alkaline volcanism is expected at convergent margins (*e.g.*, Fytikas et al., 1984; de Boer et al., 1988;
197
198 65 Bradley et al., 2003; Kay et al., 2007; Aragón et al., 2013), whereas many interpretations have been
199
200 66 proposed to explain the apparently unusual occurrence of magmatism with intraplate geochemical
201
202 67 signatures in collisional settings. These magmas have been related to i) upwelling of a mantle plume
203
204 68 through a slab window after a slab detachment (*e.g.*, Ferrari, 2004); ii) activation of extensional
205
206 69 faulting in the foreland after a collisional event (*e.g.*, Verma, 2002; Aldanmaz et al., 2006); and iii)
207
208 70 lateral and frontal ingress of asthenosphere into the mantle wedge region induced by sinking and
209
210 71 rollback of the slab (*e.g.*, Ferrari et al., 2001; Faccenna et al., 2011; Neumann et al., 2016).
211
212 72

213 73 In order to contribute to this (global scale) debate we investigated the relationship between the Alpine
214
215 74 regional tectonic evolution and the alkaline to tholeiitic magmatic activity that affected the
216
217 75 Southeastern Alps from Paleocene to Miocene. Such activity generated the Veneto Volcanic Province
218
219 76 (VVP), one of the widest magmatic districts of the Adria microplate (Fig. 1). The VVP magmas are
220
221 77 characterized by an intraplate geochemical signature, whereas contemporaneous middle Eocene-early
222
223 78 Oligocene sub-alkaline to calc-alkaline basic plutons and dikes along the Periadriatic/Insubric Line
224
225 79 in the Central Alps display a subduction fingerprint (*i.e.*, Bergell, Triangia, Adamello; Brack, 1981,
226
227 80 1984; Kagami et al., 1991; von Blanckenburg, 1992; Callegari and Brack, 2002; Oberli et al., 2004;
228
229 81 Harangi et al., 2006; Conticelli et al., 2009; Schaltegger et al., 2009; Alagna et al., 2010; Bergomi et
230
231 82 al., 2015; Fig. 1a). The Periadriatic Cenozoic subduction-related magmatism of the Central Alps is
232
233 83 generally related to upwelling of asthenospheric mantle material through a slab window after the late
234
235
236
237
238
239
240

241
242
243
244
245
246
247
248
249
250
251
252
253
254
255
256
257
258
259
260
261
262
263
264
265
266
267
268
269
270
271
272
273
274
275
276
277
278
279
280
281
282
283
284
285
286
287
288
289
290
291
292
293
294
295
296
297
298
299
300

84 Eocene Adria–Europe continental collision (~ 35 Ma; Stampfli et al., 1998, 2002; Rosenbaum and
85 Lister, 2005). The mantle flow heated the supra-subduction hydrated mantle wedge, causing melting
86 of the subcontinental lithosphere (Bergomi et al., 2015). According to the literature, the slab break–
87 off occurrence may explain also the alkaline magmatism in the Southeastern Alps: mantle diapirs
88 were sucked into the slab window and upwelled towards shallower levels heating the overriding
89 lithospheric plate to the point of triggering partial melting (Macera et al., 2003; Bergomi et al., 2015).
90 However, this interpretation is not consistent with the late Paleocene onset of the Southeastern Alps
91 magmatism, *i.e.* before the supposed slab break–off, as suggested by biostratigraphic data. Aiming to
92 unravel the interaction between the alkaline magmatism and the Alpine orogenesis, we combine the
93 literature biostratigraphic data with new high–resolution $^{40}\text{Ar}/^{39}\text{Ar}$ ages of magmatic products from
94 the Southeastern Alps. In doing this, we also present new major and trace element geochemical data
95 of the Southeastern Alps magmatic products to constrain the potential nature and evolution of their
96 mantle source(s).

98 2. A BRIEF DESCRIPTION OF GEOLOGICAL EVOLUTION OF THE ALPS

99 Both orogenic and anorogenic igneous activities within the Alpine realm are connected with the
100 relative movements of the European plate and Adria microplate, which are still debated after a century
101 of detailed structural work. Convergence of the two plates is considered to have started in the Early
102 Cretaceous as a result of the final closure of the Meliata Ocean, a back–arc basin, which separated
103 the two continental plates since the early Permian (Stampfli et al., 1998, 2002; Rosenbaum et al.,
104 2002; Dézes et al., 2004; Schmid et al., 2004, Rosenbaum and Lister, 2005). The convergence of the
105 Adria microplate and European plate marks the onset of the Alpine orogenesis, which occurred along
106 the northern margin of the Adria microplate (Stampfli et al., 1998, 2002; Rosenbaum et al., 2002;
107 Schmid et al., 2004, Rosenbaum and Lister, 2005). In particular, orogenic processes took place first
108 in the Eastern Alps (peak of high–pressure metamorphism at ~ 100–90 Ma) and then in the Western
109 Alps (peak of high–pressure metamorphism at ~ 85–60 Ma) (Manzotti et al., 2014 and references

301
302
303
304
305
306
307
308
309
310
311
312
313
314
315
316
317
318
319
320
321
322
323
324
325
326
327
328
329
330
331
332
333
334
335
336
337
338
339
340
341
342
343
344
345
346
347
348
349
350
351
352
353
354
355
356
357
358
359
360

therein). During the Paleocene (at ~ 65–55 Ma), convergence ceased for a period of 10 My due to Adria–Europe continental collision in the Eastern Alps after the subduction of the easternmost portion of Piedmont–Liguria Ocean beneath the advancing orogenic wedge (Stampfli et al., 1998, 2002; Rosenbaum et al., 2002; Dézes et al., 2004; Schmid et al., 2004; Rosenbaum and Lister, 2005). Since the early Eocene the reprise of the Adria–Europe convergence led to the subduction and final closure of the Piedmont–Liguria Ocean and Valais Ocean in the Western Alps domain at ~ 45 Ma and ~ 35 Ma, respectively (Rubatto et al., 1998; Stampfli et al., 1998, 2002; Rosenbaum and Lister, 2005). According to literature, the subducted oceanic lithospheric slab of the Central and Eastern Alps detached from the European foreland lithosphere after closure of the Valais Ocean (*e.g.*, von Blanckenburg and Davies, 1995; Stampfli et al., 1998, 2002; Dézes et al., 2004). During the Eocene with the ongoing Adria–Europe collision, E–W extension developed parallel to the belt in the Eastern Alps (Ratschbacher et al., 1989; Zampieri et al., 1995). Such rifting phase extended also into the Central Alps, in the Oligocene from ~ 34 to ~ 28 Ma (Ring, 1994; Nievergelt et al., 1996; Challandes et al., 2003; Glodny et al., 2008; Pleuger et al., 2008; Steck, 2008; Beltrando et al. 2010; Ring and Gerdens, 2016; Schmid et al., 2017). This extensional phase of the overriding plate was probably induced by the rollback of the retreating SE–dipping slab (Rosenbaum and Lister, 2005). From ~ 30 Ma until the Oligocene–Miocene boundary (~ 23 Ma), the extensional processes stopped and large-scale coarse clastic sedimentation occurred in the Eastern Alps in response to an accretionary event (Frisch et al., 2000; Rosenbaum and Lister, 2005). Another phase of extension occurred during the early and middle Miocene due to the onset of lateral tectonic extrusion at the Oligocene–Miocene boundary, which rearranged the structural pattern and created the present elongated shape of the Eastern Alps (Ratschbacher et al., 1991; Frisch et al., 2000). This lateral tectonic extrusion is ascribed to a combination of gravity–driven orogenic collapse because of an over–thickened lithosphere, and tectonic escape along conjugate fault zones driven by tangential forces due to continuing N–S convergence between the Adriatic microplate and the European plate (Ratschbacher et al., 1991; Frish et al., 2000). However, the amount of Oligocene extension was limited, focused in the eastern Tauern

361
362
363
364
365
366
367
368
369
370
371
372
373
374
375
376
377
378
379
380
381
382
383
384
385
386
387
388
389
390
391
392
393
394
395
396
397
398
399
400
401
402
403
404
405
406
407
408
409
410
411
412
413
414
415
416
417
418
419
420

136 Window ([Fig. 1a](#)) and to the east of it, whereas Miocene extension occurred at a larger scale
137 ([Ratschbacher et al., 1991](#)).

138
139 **3. THE CENOZOIC CENTRAL AND SOUTHEASTERN ALPINE MAGMATISM**

140 Cenozoic magmatism within the Alpine realm is variable in time and space reflecting the changing
141 geodynamic framework during the convergence of the Adria microplate and the European plate
142 ([Bassi et al., 2008](#)). In the Central Alps, the magmatic activity was orogenic and essentially intrusive
143 along the Periadriatic/Insubric line ([Fig. 1a](#)), represented by sub-alkaline and calc-alkaline basic
144 intrusive bodies and basaltic and andesitic dikes with calc-alkaline to shoshonitic affinity. Based on
145 radioisotopic ages, the climax of such magmatism ranged from ~ 34 to ~ 28 Ma ([von Blanckburg](#)
146 [and Davis, 1995](#); [Rosenberg, 2004](#)). However, the first evidence of igneous activity dates back at ~
147 42 Ma with the emplacement of the southern Adamello batholith and coeval dikes ([Schaltegger et al.,](#)
148 [2009](#); [Schoene et al., 2012](#); [Bergomi et al., 2015](#)). On the contrary, in the Southeastern Alps the
149 magmatic activity was anorogenic with effusive to subvolcanic character. It occurred in an elongated
150 NNW-SSE area of about 1500 km², defining from north-west to south-east five main volcanic
151 districts: Val d'Adige, Lessini Mts., Marosticano, Berici Hills, and Euganean Hills ([Beccaluva et al.,](#)
152 [2007](#)). Together, these districts constituted a Cenozoic magmatic province in the Southeastern alpine
153 domain known in literature as Veneto Volcanic Province (VVP; *e.g.*, [De Vecchi and Sedeà, 1995](#);
154 [Beccaluva et al., 2001, 2007](#); [Macera et al., 2003, 2008](#); [Visonà et al., 2007](#); [Fig. 1, 1a](#)).

421
422
423
424
425
426
427
428
429
430
431
432
433
434
435
436
437
438
439
440
441
442
443
444
445
446
447
448
449
450
451
452
453
454
455
456
457
458
459
460
461
462
463
464
465
466
467
468
469
470
471
472
473
474
475
476
477
478
479
480

Figure 1. Simplified geological map of the Veneto Volcanic Province (VVP; De Vecchi and Sedeà, 1995), showing the locations of the samples collected for this work. Ages (in Ma) of the magmatic rocks occurring in the VVP are framed with blue dashed line (literature data) and red continuous line (this work). Ages in italics are derived from mini-plateaus (50–70% ³⁹Ar released) and are considered minimum ages (see explanation in section 9, and in section S2 of Supplementary materials). Red stars are ⁴⁰Ar/³⁹Ar ages, blue diamonds are U–Pb ages, blue triangles are Rb–Sr ages, blue circles are K–Ar dates, and black squares are samples of this work for which ⁴⁰Ar/³⁹Ar analyses were not performed. Previously published ages for Lessini Mts. are from Savelli and Lipparini (1979) and Visonà et al. (2007); ages for Euganean Hills are from Zantendeschi (1994) and Bartoli et al. (2014); ages for Marosticano area are from Savelli and Lipparini (1979). Inset a) present-day location of VVP in the Italian peninsula, in relation to European, African plates and Adria microplate (modified from Carminati and Doglioni, 2012) and locations of Periadriatic basic and acid plutons, in blue and in black, respectively, along the Periadriatic/Insubric line. For comparative purpose, in this work only the Periadriatic basic plutons of the Central Alps were considered. Abbreviation for plutons: B = Bergell, T = Triglia, A = Adamello, R = Rensen, VdR = Vedrette di Ries. **[2 columns fitting]**

481
482
483
484
485
486
487
488
489
490
491
492
493
494
495
496
497
498
499
500
501
502
503
504
505
506
507
508
509
510
511
512
513
514
515
516
517
518
519
520
521
522
523
524
525
526
527
528
529
530
531
532
533
534
535
536
537
538
539
540

3.1 Geological outline

Magmatic activity started in the VVP already in the Paleocene (Beccaluva et al., 2007; Bassi et al., 2008), along the Jurassic Trento carbonate platform, which encompassed the Val d'Adige and Lessini Mts. areas (Winterer and Bosellini, 1981; Dewey et al., 1989; Zampieri et al., 1995). After the Adria–Europe collision in the Eastern Alps (~ 65 Ma; Stampfli et al., 1998, 2002; Rosenbaum et al., 2002; Dézes et al., 2004; Schmid et al., 2004; Rosenbaum and Lister, 2005), extension developed (Ratschbacher et al., 1989). As a consequence in the Southeastern Alpine domain the rigid Trento platform block–faulted forming a horst and graben structure, called the Alpone–Agnò Graben (Zampieri, 1995). Until the middle Eocene the extensional tectonics of the new NNW–SSE transtensional fault systems and the Alpone–Agnò Graben controlled the deposition of limestone and the volcanic activity, which manifested with short–lived pulses (Barbieri et al., 1991) in the Monte Baldo area for the Val d'Adige district and along the Lessini Mts. district (Luciani, 1989). Therefore, in the troughs of the horst and graben structure basic–ultrabasic hyaloclastites, volcanoclastics, subaqueous, and subaerial lava flows were accumulated and interbedded between the Scaglia Rossa (Upper Cretaceous–late Paleocene) and the Eocene limestones, or within the latter (Fig. 2). According to biostratigraphic data the magmatic activity occurred later in the eastern VVP districts (*i.e.*, Euganean Hills and Marosticano areas; Piccoli et al., 1976, 1981; Luciani, 1989; Savelli and Lipparini, 1979). From the late Eocene to early Oligocene basic volcanic deposits were interbedded with marls of the Euganean Hills pelagic environment (De Vecchi et al., 1976; Piccoli et al., 1976, 1981; Fig. 2). In the early Oligocene, the Euganean magmatism changed and was dominated by rhyolites, trachytes and subordinately by trachyandesites (latites) and basalts, which formed mainly subvolcanic bodies and less abundant lava flows (De Vecchi et al., 1976; Piccoli et al., 1976, 1981). In the middle Oligocene, the magmatic activity resumed in the Marosticano (Fig. 2) and Lessini Mts. districts in a subaqueous environment as testified by the marine sediments (sandstones, calcarenites and limestones; Gavioli, 1972; Savelli and Lipparini, 1979) interbedded with the volcanic deposits (Fig. 2). Sparse Oligocene explosive and effusive volcanic activity is documented also in the Berici

541
542
543
544
545
546
547
548
549
550
551
552
553
554
555
556
557
558
559
560
561
562
563
564
565
566
567
568
569
570
571
572
573
574
575
576
577
578
579
580
581
582
583
584
585
586
587
588
589
590
591
592
593
594
595
596
597
598
599
600

199 Hills (west of the Euganean Hills; Bassi et al., 2008). At the end of the late Oligocene, the
200 Marosticano and Lessini Mts. areas emerged (Frasconi Ritondale Spano and Bassani, 1973) shortly
201 before eruption of the last subaerial volcanic products at the beginning of the Miocene (Savelli and
202 Lipparini, 1979). These volcanic deposits are overlain by coralline calcarenites of early Miocene age
(Frasconi Ritondale Spano, 1969; Savelli and Lipparini, 1979; [Fig. 2](#)), testifying to a new
204 transgression event.

601
602
603
604
605
606
607
608
609
610
611
612
613
614
615
616
617
618
619
620
621
622
623
624
625
626
627
628
629
630
631
632
633
634
635
636
637
638
639
640
641
642
643
644
645
646
647
648
649
650
651
652
653
654
655
656
657
658
659
660

Figure 2. Simplified Upper Cretaceous to lower Miocene stratigraphy of the studied areas: Monte Baldo northern sector (Val d'Adige district; Luciani, 1989; De Vecchi and Sedea, 1995), Eastern Lessini Mts. (De Vecchi and Sedea, 1995; Bassi et al., 2008), Euganean Hills (Piccoli et al., 1976, 1981), and Marosticano (Frascari Ritondale Spano and Bassani, 1973; De Vecchi and Sedea, 1995; Bassi et al., 2008). Ages and uncertainties are reported in Ma. Ages in italics are derived from mini-plateaus (50–70% ³⁹Ar released) and are considered minimum ages only (see explanation in section 9 and in the section S2 of Supplementary materials). Ages derived from pre-erupted zircons from Lessini Mts. and Euganean Hills districts are considered maximum ages (see explanation in section 4). Previously published geochronological data for eastern Lessini Mts. are from Borsi et al. (1969), Savelli and Lipparini (1979), and Visonà et al. (2007), for Euganean Hills are from Borsi et al. (1969), Zantendeschi (1994), and Bartoli et al. (2014), and for Marosticano are from Savelli and Lipparini (1979). In the figure the main geodynamic events, extension phases, and coarse clastic sedimentation occurred in Central and Eastern Alps are reported, as well as the climax of the orogenic Periadriatic Central Alps magmatism. **[2 columns fitting]**

661
662
663
664
665
666
667
668
669
670
671
672
673
674
675
676
677
678
679
680
681
682
683
684
685
686
687
688
689
690
691
692
693
694
695
696
697
698
699
700
701
702
703
704
705
706
707
708
709
710
711
712
713
714
715
716
717
718
719
720

4. PREVIOUS GEOCHRONOLOGICAL STUDIES OF VVP

The integration of stratigraphic records with reliable radioisotopic ages allows to i) better constrain the distribution and the timeframe of such highly variable, but temporally short, magmatic activity and ii) infer the geodynamic evolution of this magmatic province. Previously obtained geochronological data are mainly K–Ar ages on basic–ultrabasic whole–rocks (Borsi et al., 1969; Savelli and Lipparini, 1979; Fig. 1). These K–Ar data yielded eruption ages of 42.5 ± 1.5 to 20.4 ± 0.8 Ma for the Lessini Mts., 42.0 ± 1.5 Ma for the Euganean Hills, and from 33.7 ± 1.2 to 20.4 ± 0.8 Ma for the Marosticano district. However, the reliability of such ages is questionable, as the K–Ar dating technique is not able to recognize (and correct for) non–atmospheric $^{40}\text{Ar}/^{36}\text{Ar}$ ratios and alteration effects (Oostingh et al., 2017). Zantendeschi (1994) dated Euganean trachytes and rhyolites using the whole–rock Rb–Sr method (Fig. 1), the obtained eruption ages span from 34 ± 2 to 28 ± 1 Ma. These ages also must be treated with caution, as the ^{87}Rb decay constant is still poorly defined and Rb/Sr isotopic system is prone to secondary alteration (Begemann et al., 2001; Schmitz et al., 2003). The most recent radioisotopic data available (Fig. 1) are U–Pb ages obtained using a sensitive high–resolution ion microprobe (SHRIMP) on zircons hosted i) in a porphyritic basanite lava and in two altered dykes of the Lessini Mts. (Visonà et al., 2007) and ii) in magmatic enclaves within trachytes of the Euganean Hills (Bartoli et al., 2014). These ages may be interpreted as maximum ages of eruptions as the analysed zircons were not crystallized directly from the erupted magma. The Lessini Mts. zircons yielded Eocene ages spanning from 51.1 ± 1.5 to 44.9 ± 2.8 Ma (Visonà et al., 2007), even if it should be considered that these data are not concordant. Zircons from the Euganean Hills xenoliths yielded Oligocenic ages of 31.9 ± 1.3 Ma and 30.6 ± 1.5 Ma (Bartoli et al., 2014). From this overview on the currently available geochronological data and related uncertainties, it is clear that more accurate age data are essential for the temporal reconstruction of the VVP magmatism. In this work, new high–resolution ages were obtained using the $^{40}\text{Ar}/^{39}\text{Ar}$ systematic on groundmass samples on mineral separates, which is currently widely accepted as an accurate dating technique (McDougall and Harrison, 1999).

721
722
723
724
725
726
727
728
729
730
731
732
733
734
735
736
737
738
739
740
741
742
743
744
745
746
747
748
749
750
751
752
753
754
755
756
757
758
759
760
761
762
763
764
765
766
767
768
769
770
771
772
773
774
775
776
777
778
779
780

247
248
249
250
251
252
253
254
255
256
257
258
259
260
261
262
263
264
265
266
267
268
269
270
271
272

5. SAMPLING

Following biostratigraphic information we selected our samples in order to encompass most of the time range of the VVP magmatism. From Val d'Adige and Lessini Mts., the two oldest magmatic districts, samples were collected from basic–ultrabasic lava flows and volcanic necks. BAL1 and BAL7, two out of three samples of Val d'Adige district, are from the northeastern part of Monte Baldo (Table 1; Fig. 1). BAL1 was collected nearly at the top of a subaqueous lava flow interbedded between middle and late Eocene limestones (Calcare di Torbole and Calcare di Nago; Fig. 2), whereas BAL7 was sampled from a thin sill between Cretaceous–Paleocene (Scaglia Rossa) and middle Eocene limestones (Calcare di Torbole; Fig. 2). The third sample from Val d'Adige district, BI14, was collected from a volcanic neck exposed in a quarry near Rovereto (Table 1; Fig. 1). The sampling for Lessini Mts. district was focused near the famous Bolca Fossil–Lagerstätte area (Papazzoni et al., 2014, and references therein). Sample TER1 (Table 1; Fig. 1) was collected from a lava flow interbedded with red clays of unknown age, whereas sample BOL1 (Table 1; Fig. 1) was collected from the volcanic neck preserved near the mentioned fossiliferous area. This neck cuts 10–20 m of freshwater–brackish sediments of probable Ypresian age (Barbieri and Medizza, 1969; Medizza, 1980; Sorbini, 1989; Giusberti, et al., 2014).

The Euganean Hills are the only VVP magmatic district where basic, intermediate, and acid magmas erupted or intruded at shallow–depth forming lava flows and subvolcanic bodies (mainly laccoliths) during late Eocene–Oligocene (Fig. 2). We have sampled and analysed rocks in order to investigate the entire range of the lithologies. Samples EU1AB, EU53, EU52, EU8B, and EU13A represent the least differentiated products of the Euganean sample suite. The basaltic andesite lava flow EU1AB was collected from an outcrop in the western part of the Euganean Hills (Table 1; Fig. 1). The basaltic andesite sample EU53 was collected from a subvolcanic body at the center of the Euganean Hills, and basaltic trachyandesite EU52 from an intrusion cutting this basaltic andesite body (Table 1; Fig. 1). The basaltic trachyandesite EU8B and the latite EU13A were collected from subvolcanic bodies

781
782
783
784
785
786
787
788
789
790
791
792
793
794
795
796
797
798
799
800
801
802
803
804
805
806
807
808
809
810
811
812
813
814
815
816
817
818
819
820
821
822
823
824
825
826
827
828
829
830
831
832
833
834
835
836
837
838
839
840

273 (Monte Oliveto and Monte Cecilia), in the eastern and southern sectors of the Euganean Hills,
274 respectively (Table 1; Fig. 1). Samples EU4, EU5B, and EU9 represent the most acid products
275 available for the Euganean Hills. The trachyte EU4 (Monte Merlo quarry, northern sector of the
276 Euganean Hills; Table 1; Fig. 1), the rhyolite EU5B (Monte Alto, eastern sector; Table 1; Fig. 1), and
277 the rhyolite EU9 (Monte Ricco, southeastern sector; Table 1; Fig. 1), were collected from laccoliths
278 intruded in the Euganean Marls Formation (Oligocene; Piccoli et al., 1976, 1981; Fig. 2).
279 Finally, for the Marosticano district, where one of the last VVP magmatic events occurred, we
280 sampled two specimens (LB1 and 25B). These samples were collected from the ultrabasic volcanic
281 neck cutting the middle Oligocene marine sediments of the Salcedo formation at Monte Glosio
282 (Savelli and Lipparini, 1979; Table 1; Figs. 1, 2).

6. ANALYTICAL METHODS

285 Whole-rock major and trace elements were determined by Wavelength Dispersive X-Ray
286 Fluorescence Spectrometry (WDXRF) at the University of Ferrara (IT; ARL Advant-XP
287 spectrometer) and at the University of Padova (IT; Philips PW1404). Rb, Sr, Y, Zr, Nb, Hf, Ta, Th,
288 U, and rare-earth elements (REEs) were performed with Inductively Coupled Plasma-Mass
289 Spectrometry (ICP-MS) at the University of Ferrara (Thermo Series X-I spectrometer) and at the
290 University of Bretagne Occidentale, Brest (FR; Thermo Element2). Clinopyroxene compositions
291 were determined by means of a CAMECA SX50 electron microprobe at the IGG-CNR of Padova.
292 For $^{40}\text{Ar}/^{39}\text{Ar}$ geochronological analyses, after irradiation in TRIGA Reactor at the Oregon State
293 University (USA) or US Geological Survey nuclear reactor (Denver, USA), groundmass and mineral
294 separates were analysed by laser step-heating with i) ARGUS VI (samples BAL1, BAL7, TER1,
295 BOL1, LB1, and EU52) and ii) MAP 215-50 (samples EU4, EU5B, EU8B, and EU13A) mass
296 spectrometers at Curtin University within the Western Australian Argon Isotope Facility (WAAIF)
297 of the John de Laeter Centre and iii) Nu Instruments Noblesse magnetic sector noble gas mass

841
842
843
844
845
846
847
848
849
850
851
852
853
854
855
856
857
858
859
860
861
862
863
864
865
866
867
868
869
870
871
872
873
874
875
876
877
878
879
880
881
882
883
884
885
886
887
888
889
890
891
892
893
894
895
896
897
898
899
900

298 spectrometer (samples BI14 and 25B) at the Noble Gas Lab of the University of Vermont. Extended
299 analytical procedures and details are reported in [section S1 of the Supplementary materials](#).

300 301 **7. PETROGRAPHY AND ROCK CLASSIFICATION**

302 Samples BAL7, BI14 (Val d'Adige district), BOL1 (Lessini Mts. district), LB1, and 25B
303 (Marosticano district) are classified as basanites in the total alkali vs. silica (TAS) diagram (Le Maitre
304 et al., 2002; [Fig. 3](#)) and they are nepheline-normative ([Table 1](#)). These rocks show porphyritic texture
305 with large (up to 1 mm across) phenocrysts of euhedral olivine and smaller clinopyroxene
306 (prevalently diopside; up to 0.5 mm across) as dominant phenocrysts set in a microcrystalline
307 groundmass constituted by acicular plagioclase, clinopyroxene, and oxides. Interestingly, BOL1,
308 LB1, and 25B host small (3–4 mm) spinel peridotite xenoliths, probably fragments of the bigger (5–
309 15 cm) counterparts already discovered in alkaline basalts of the Val d'Adige, Lessini Mts., and
310 Marosticano districts (Morten et al., 1989; Siena and Coltorti, 1989, 1993; Beccaluva et al., 2001;
311 Gasperini et al., 2006; Brombin et al., 2018). These fragments were extracted from the samples before
312 proceeding with the chemical analyses.

313 BAL1 (Val d'Adige district) and TER1 (Lessini Mts. district) are two basalts according to the TAS
314 classification ([Fig. 3](#)), in particular the first sample is olivine/hyperstene normative, while the second
315 one is quartz-normative ([Table 1](#)). They have intergranular texture characterized by elongated and
316 euhedral plagioclase (up to 2 mm across) and subhedral–anhedral clinopyroxene, olivine and oxides
317 filling spaces between plagioclase crystals. The presence of scarce iddingsite (substituting for olivine)
318 and amygdules of secondary hydrothermal minerals are indicative of slight alteration. According to
319 the TAS diagram, EU1AB and EU53 (Euganean Hills district) are classified as basaltic andesites
320 ([Fig. 3](#)). Both samples are quartz-normative ([Table 1](#)) and they have clinopyroxene, plagioclase, and
321 oxides as phenocrysts and in the groundmass.

322 EU52 and EU8B (Euganean Hills district) are classified as basaltic trachyandesites in the TAS
323 diagram ([Fig. 3](#)). EU52 is nepheline-normative, while EU8B is quartz-normative ([Table 1](#)). The

901
902
903 324 phenocrysts of these two samples are plagioclase, amphibole and clinopyroxene in a microcrystalline
904
905 325 groundmass of plagioclase and oxides. The plagioclase phenocrysts (up to 2 mm across in EU8B and
906
907 326 up to 5 mm across in EU52) are generally euhedral with occasional sieved-textured centers (EU8B).
908
909
910 327 The clinopyroxene phenocrysts (up to 1 mm across) are subhedral with rounded edges. Only EU52
911
912 328 exhibits large (up to 5 mm across) euhedral amphibole without any sign of alteration.
913
914 329 Sample EU13A (Euganean Hills district) is classified as latite (Fig. 3) and it is quartz-normative
915
916 330 (Table 1). It contains medium-grained (0.5–1.5 mm across) plagioclase, biotite, and clinopyroxene
917
918 331 in a microcrystalline groundmass of plagioclase feldspar, and oxides. The plagioclase phenocrysts
919
920 332 (up to 1.5 mm across) are generally euhedral; a sieved-textured core is also present. The
921
922 333 clinopyroxene crystals (1 mm across) are subhedral with rounded edges. Biotite (1 mm across) is
923
924 334 subhedral and partly replaced by oxides along the rims.
925
926
927 335 EU4, EU5B, and EU9 (Euganean Hills district) are the most felsic samples of the entire suite.
928
929 336 According to the TAS diagram, EU4 is a trachyte, whereas EU5B and EU9 are rhyolites (Fig. 3). All
930
931 337 of them are quartz-normative (Table 1). They exhibit glomeroporphyritic texture and the phenocrysts
932
933 338 are predominantly alkali feldspar (sanidine, up to 5 mm across), plagioclase (up to 5 mm across), and
934
935 339 biotite (1–2 mm across) in a microcrystalline groundmass consisting of alkali feldspar and Fe–Ti
936
937 340 oxides. Only in EU4 phenocrysts of amphibole (1–2 mm across) are present. The glomerocrysts, up
938
939 341 to 1 cm in diameter, are both monomineralic (alkali feldspar) or formed by plagioclase and alkali
940
941 342 feldspar in the same cluster. Crystals within these glomerocrysts are subhedral with rounded corners
942
943 343 on the edges of grains.
944

945
946 344

947
948
949
950
951
952
953
954
955
956
957
958
959
960

961
962
963
964
965
966
967
968
969
970
971
972
973
974
975
976
977
978
979
980
981
982
983
984
985
986
987
988
989
990
991
992
993
994
995
996
997
998
999
1000
1001
1002
1003
1004
1005
1006
1007
1008
1009
1010
1011
1012
1013
1014
1015
1016
1017
1018
1019
1020

Figure 3. Total Alkali vs. Silica (TAS) classification diagram (Le Maitre et al., 2002) of the magmatic products from Val d'Adige, Lessini Mts., Marosticano, and Euganean Hills studied in this work (large symbols) and in literature (small symbols). Val d'Adige compositions are from Beccaluva et al. (2007); Lessini Mts., and Marosticano compositions are from Macera et al. (2003) and Beccaluva et al. (2007); Euganean Hills compositions are from Milani et al. (1999) and Macera et al. (2003). The fields for trachybasalt and trachyandesite are labelled here “potassic trachybasalt” and “latite”, respectively, as most of the samples of this study display $(\text{Na}_2\text{O} - \text{K}_2\text{O}) \leq 2.0$ and are therefore potassic, as defined by Le Maitre (2002). The alkaline–tholeiitic discrimination line is from Irvine and Baragar (1971). **[1 column fitting]**

8. GEOCHEMISTRY

Bulk major and trace element compositions of the analysed magmatic rocks are reported in [Tables 1 and 2](#). On the TAS diagram ([Fig. 3](#)) this group of magmatic rocks overlaps with those previously published for the VVP (Milani et al., 1999; Macera et al., 2003; Beccaluva et al., 2007), spanning a wide range of compositions from alkaline to subalkaline and encompassing ultrabasic, basic, intermediate, and acid rocks.

The basic–ultrabasic rocks span a relatively wide range in terms of SiO₂ (42.01 to 53.22 wt.%; [Table 1](#)), MgO (12.26 to 3.85 wt.%; [Table 1](#)), and mg# [69.64 to 43.06, where mg# is defined as $100 \times \text{Mg}/(\text{Mg} + \text{Fe}^{2+})_{\text{mol}}$, Fe³⁺/Fe²⁺ being 0.15; [Table 1](#)] reflecting the different degree of evolution for the VVP lithologies (*i.e.*, from basanites to basaltic trachyandesites). The analysed samples have predominantly alkaline affinities with the majority of the samples having potassic affinity [(Na₂O – K₂O) ≤ 2.0 wt.%] with (Na₂O – K₂O) ranging from 0 to 1.72 wt.%. Only BI14, EU53, and EU1AB have sodic affinity [(Na₂O – K₂O) = 2.51 - 3.48 wt.%]. Chondrite–normalized rare earth element (REE) patterns are generally parallel for all basic–ultrabasic rocks ([Fig. 4a](#)). These patterns are strongly light REE (LREE) enriched with a significant LREE to heavy REE (HREE) fractionation [(La/Yb)_N = 5.5 to 24.3; (Dy/Lu)_N = 1.8 to 2.4; [Fig. 4a](#)]. Irrespective to the lithology, samples from Val d’Adige, Lessini Mts., Euganean Hills (EU1AB and EU53), and Marosticano exhibit negative Rb and K anomalies and spikes for Ba, Sr, and P in the primitive mantle–normalized incompatible trace element diagram ([Fig. 4b](#)). Basaltic trachyandesite EU52 (Euganean Hills) mimics the general trace element features of the basic–ultrabasic samples. However, it lacks significant Sr and P spikes and it is depleted in Ba, consistently with its more evolved character and with possible feldspar and apatite fractionation ([Fig. 4b](#)).

The intermediate–acid rocks have higher SiO₂ (55.63 to 72.00 wt.%; [Table 1](#)) and lower MgO (3.14 to 0.14 wt.%; [Table 1](#)) contents with respect to the previous group, consistent with their more evolved nature. All the samples of this group have potassic affinity [(Na₂O – K₂O) = 0 -1.55]. No trace element analyses were performed for this group, as in this work we preferred to focus on the geochemistry of

1081
1082
1083
1084
1085
1086
1087
1088
1089
1090
1091
1092
1093
1094
1095
1096
1097
1098
1099
1100
1101
1102
1103
1104
1105
1106
1107
1108
1109
1110
1111
1112
1113
1114
1115
1116
1117
1118
1119
1120
1121
1122
1123
1124
1125
1126
1127
1128
1129
1130
1131
1132
1133
1134
1135
1136
1137
1138
1139
1140

381 basic-ultrabasic samples that can shed light on their mantle sources, while more evolved rocks may
382 be significantly affected by fractional crystallization.

383

| Sample | BAL1 | BAL7 | BI14 | TER1 | BOL1 | EU1AB | EU53 | EU52 | EU8B |
|--------------------------------|--------------------------------|--------------------------------|--------------------------------|--------------------------------|--------------------------------|--------------------------------|--------------------------------|--------------------------------|--------------------------------|
| Rock | Basalt | Basanite | Basanite | Basalt | Basanite | Basaltic andesite | Basaltic andesite | Basaltic trachyandesite | Basaltic trachyandesite |
| District | Val d'Adige | Val d'Adige | Val d'Adige | Lessini Mts. | Lessini Mts. | Euganean Hills | Euganean Hills | Euganean Hills | Euganean Hills |
| Coordinates | 45°47'02.12"N 10°54'18.26"E | 45°44'37.00"N 10°53'04.00"E | 45°47'02.12"N 10°54'18.26"E | 45°35'34.05"N 11°12'58.89"E | 45°35'51.84"N 11°12'31.34"E | 45°19'40.08"N 11°38'58.00"E | 45°32'87.00"N 11°68'48.00"E | 45°32'87.88"N 11°68'48.75"E | 45°19'07.08"N 11°46'31.04"E |
| SiO ₂ | 46.83 | 42.62 | 42.01 | 48.72 | 43.00 | 52.00 | 53.22 | 51.70 | 55.63 |
| TiO ₂ | 2.75 | 3.71 | 3.22 | 2.80 | 3.44 | 2.45 | 2.37 | 2.75 | 2.01 |
| Al ₂ O ₃ | 14.59 | 13.04 | 14.65 | 13.53 | 13.21 | 14.85 | 14.83 | 16.29 | 15.53 |
| Fe ₂ O ₃ | 14.61 | 14.56 | 13.11 | 11.00 | 14.35 | 10.02 | 11.24 | 10.43 | 8.82 |
| MnO | 0.20 | 0.19 | 0.17 | 0.36 | 0.19 | 0.12 | 0.12 | 0.12 | 0.13 |
| MgO | 6.94 | 8.96 | 8.28 | 10.77 | 9.55 | 6.25 | 6.22 | 3.85 | 3.41 |
| CaO | 10.39 | 11.03 | 10.34 | 9.93 | 10.23 | 9.50 | 8.66 | 6.12 | 6.47 |
| Na ₂ O | 2.24 | 3.09 | 4.98 | 1.09 | 3.06 | 3.10 | 3.24 | 4.35 | 4.23 |
| K ₂ O | 0.75 | 1.37 | 1.42 | 1.17 | 1.45 | 0.59 | 0.43 | 3.23 | 2.68 |
| P ₂ O ₅ | 0.70 | 1.53 | 1.81 | 0.64 | 0.97 | 0.35 | 0.26 | 0.97 | 0.59 |
| Tot | 100.01 | 100.10 | 100.00 | 100.00 | 99.45 | 99.23 | 100.59 | 99.81 | 99.50 |
| LOI | 3.02 | 1.10 | 2.17 | 3.30 | 0.55 | 3.69 | 3.11 | 0.83 | 2.34 |
| mg# | 49.32 | 55.77 | 56.40 | 66.72 | 57.69 | 56.10 | 53.13 | 43.06 | 44.20 |
| Quartz | - | - | - | 1.4 | - | 2.6 | 4.4 | - | 2.6 |
| Nepheline | - | 7.9 | 18.3 | - | 8.2 | - | - | 0.43 | - |
| Diopside | 16.2 | 22.3 | 21.6 | 13.4 | 21.8 | 16.5 | 13.6 | 7.2 | 10.6 |
| Hyperstene | 16.1 | - | - | 30.9 | - | 18.1 | 19.6 | - | 11.6 |
| Olivine | 6.0 | 18.0 | 15.3 | - | 19.5 | - | - | 11.2 | 0- |

mg# = 100 x Mg/(Mg+Fe²⁺)_{mol} considering Fe³⁺/Fe²⁺ 0.15

Table 1. Whole-rock major element compositions (wt.%) and CIPW normative compositions of magmatic products from Val d'Adige, Lessini Mts., Euganean Hills, and Marosticano.

1182
 1183
 1184
 1185
 1186
 1187
 1188
 1189
 1190
 1191
 1192
 1193
 1194
 1195
 1196
 1197
 1198
 1199
 1200
 1201
 1202
 1203
 1204
 1205
 1206
 1207
 1208
 1209
 1210
 1211
 1212
 1213
 1214
 1215
 1216
 1217
 1218
 1219
 1220
 1221
 1222

| Sample | EU13A | EU4 | EU5B | EU9 | LB1 | 25B |
|--------------------------------|--------------------------------|--------------------------------|--------------------------------|--------------------------------|--------------------------------|--------------------------------|
| Rock | Latite | Trachyte | Rhyolite | Rhyolite | Basanite | Basanite |
| District | Euganean Hills | Euganean Hills | Euganean Hills | Euganean Hills | Marosticano | Marosticano |
| Coordinates | 45°15'07.02"N 11°41'27.00"E | 45°20'20.09"N 11°39'06.09"E | 45°19'16.00"N 11°45'24.00"E | 45°14'57.02"N 11°44'28.07"E | 45°76'72.83"N 11°67'78.97"E | 45°76'72.00"N 11°67'78.00"E |
| SiO ₂ | 56.90 | 65.52 | 69.86 | 72.00 | 43.22 | 44.02 |
| TiO ₂ | 2.00 | 0.69 | 0.39 | 0.32 | 3.47 | 3.12 |
| Al ₂ O ₃ | 15.68 | 16.51 | 15.41 | 14.81 | 11.52 | 12.80 |
| Fe ₂ O ₃ | 7.27 | 3.71 | 2.05 | 1.26 | 13.12 | 10.95 |
| MnO | 0.09 | 0.06 | 0.09 | 0.03 | 0.19 | 0.16 |
| MgO | 3.14 | 0.72 | 0.17 | 0.14 | 11.29 | 12.26 |
| CaO | 5.68 | 1.59 | 0.65 | 0.49 | 11.85 | 10.89 |
| Na ₂ O | 4.11 | 5.23 | 4.80 | 4.63 | 3.06 | 3.22 |
| K ₂ O | 3.59 | 5.11 | 5.77 | 5.56 | 1.36 | 1.53 |
| P ₂ O ₅ | 0.57 | 0.30 | 0.07 | 0.03 | 0.97 | 1.06 |
| Tot | 99.03 | 99.44 | 99.26 | 99.27 | 100.05 | 100.00 |
| LOI | 1.64 | 0.35 | 0.66 | 0.14 | 1.17 | 1.08 |
| mg# | 46.95 | 28.45 | 14.52 | 18.54 | 63.81 | 69.64 |
| Quartz | 3.5 | 10.3 | 17.6 | 22.3 | - | - |
| Nepheline | - | - | - | - | 11.0 | 10.4 |
| Diopside | 9.0 | - | - | - | 31.5 | 25.1 |
| Hyperstene | 9.8 | 5.6 | 2.6 | 1.5 | - | - |
| Olivine | - | - | - | - | 17.9 | 20.1 |

mg# = 100 x Mg/(Mg+Fe²⁺)_{mol} considering Fe³⁺/Fe²⁺ 0.15

390
 391
 392
 393

Table 1 (continued). Whole-rock major element compositions (wt.%) of magmatic products from Val d'Adige, Lessini Mts., Euganean Hills, and Marosticano.

1223
 1224
 1225
 1226
 1227
 1228
 1229
 1230
 1231
 1232
 1233
 1234
 1235
 1236
 1237
 1238
 1239
 1240
 1241
 1242
 1243
 1244
 1245
 1246
 1247
 1248
 1249
 1250
 1251
 1252
 1253
 1254
 1255
 1256
 1257
 1258
 1259
 1260
 1261
 1262
 1263

| Sample | BAL7 | TER1 | BOL1 | EU1AB | EU53 | EU52 | LB1 |
|----------|-------------|--------------|--------------|-------------------|-------------------|-------------------------|-------------|
| Rock | Basanite | Basalt | Basanite | Basaltic andesite | Basaltic andesite | Basaltic trachyandesite | Basanite |
| District | Val d'Adige | Lessini Mts. | Lessini Mts. | Euganean Hills | Euganean Hills | Euganean Hills | Marosticano |
| Rb | 29.6 | 27.8 | 37.4 | 17.0 | 15.0 | 71.0 | 46.6 |
| Ba | 860 | 664 | 553 | 348 | 264 | 777 | 777 |
| Th | 6.80 | 5.87 | 5.99 | 2.95 | 2.85 | 10.1 | 6.85 |
| U | 1.77 | 1.34 | 1.42 | 0.83 | 0.82 | 2.56 | 2.00 |
| Nb | 124 | 74.3 | 91.4 | 28.0 | 21.0 | 96.6 | 118 |
| Ta | 4.47 | 2.52 | 3.74 | 1.38 | 1.43 | 4.64 | 4.67 |
| La | 66.6 | 39.0 | 47.0 | 18.4 | 13.7 | 72.4 | 57.5 |
| Ce | 131 | 75.8 | 96.1 | 38.5 | 28.5 | 128 | 109 |
| Pr | 15.5 | 8.37 | 11.5 | 4.68 | 3.71 | 14.4 | 12.1 |
| Sr | 1744 | 736 | 1060 | 473 | 349 | 929 | 1071 |
| Nd | 67.4 | 35.6 | 52.0 | 20.4 | 16.9 | 55.9 | 53.3 |
| Zr | 413 | 235 | 354 | 175 | 168 | 456 | 382 |
| Hf | 8.29 | 5.01 | 7.58 | 3.93 | 4.03 | 9.11 | 7.91 |
| Sm | 12.6 | 6.73 | 10.1 | 5.36 | 4.85 | 10.9 | 9.68 |
| Eu | 3.86 | 2.16 | 3.13 | 1.83 | 1.75 | 3.25 | 2.91 |
| Gd | 11.7 | 6.66 | 9.32 | 5.55 | 5.47 | 8.82 | 8.92 |
| Tb | 1.64 | 0.99 | 1.38 | 0.83 | 0.85 | 1.19 | 1.27 |
| Dy | 7.20 | 4.63 | 6.23 | 4.48 | 4.77 | 6.15 | 5.61 |
| Y | 40.8 | 28.7 | 35.4 | 24.1 | 24.0 | 34.6 | 31.5 |
| Ho | 1.28 | 0.88 | 1.10 | 0.83 | 0.88 | 1.10 | 1.00 |
| Er | 3.05 | 2.22 | 2.62 | 1.97 | 2.20 | 2.64 | 2.42 |
| Yb | 2.21 | 1.84 | 1.93 | 1.56 | 1.70 | 2.03 | 1.78 |
| Lu | 0.31 | 0.27 | 0.27 | 0.21 | 0.23 | 0.27 | 0.25 |

All trace elements (ppm) were analysed by ICP-MS except Ba (XRF).

Table 2. Trace element (ppm) compositions of magmatic products from Val d'Adige, Lessini Mts., Euganean Hills, and Marosticano.

1264
1265
1266
1267
1268
1269
1270
1271
1272
1273
1274
1275
1276
1277
1278
1279
1280
1281
1282
1283
1284
1285
1286
1287
1288
1289
1290
1291
1292
1293
1294
1295
1296
1297
1298
1299
1300
1301
1302
1303
1304
1305
1306
1307
1308
1309
1310
1311
1312
1313
1314
1315
1316
1317
1318
1319
1320
1321
1322

Figure 4. Chondrite-normalized rare earth elements (a) and primitive mantle-normalized trace element patterns (b) for basic-ultrabasic rocks from Val d'Adige, Lessini Mts., Euganean Hills, and Marosticano. The least evolved Euganean Hills samples are also shown for comparison. Previously published trace element compositions for basic-ultrabasic rocks from Val d'Adige, Lessini Mts., Euganean Hills, and Marosticano (Macera et al., 2003; Beccaluva et al., 2007) are reported as a shaded area. Ocean Island Basalt composition (OIB; Sun and McDonough, 1989) is shown with a black dashed line. The average trace element compositions of orogenic calc-alkaline and sub-alkaline magmas of the Periadriatic Central Alps magmatism are from Bergomi et al. (2015) and are shown with a black continuous line. Normalizing factors are from McDonough and Sun (1995).

9. $^{40}\text{Ar}/^{39}\text{Ar}$ GEOCHRONOLOGICAL RESULTS

Detailed $^{40}\text{Ar}/^{39}\text{Ar}$ results of the analysed magmatic rocks are reported in [Tables 3, 4](#). Groundmass samples of BAL1, BAL7, TER1, BOL1, and LB1 as well as amphibole and plagioclase separates of EU52 were analysed with a new generation noble gas multicollector mass spectrometer (ARGUS VI). Instead, mineral separates (*i.e.*, biotite, feldspar, sanidine) from EU8B, EU13A, EU4, EU5B, and EU9 were analysed with the MAP215–50 mass spectrometer. EU1AB and EU53, two basaltic andesites from the Euganean Hills district, could not be dated due to the lack of fresh K–rich minerals. Many analysed samples are characterized by $^{40}\text{Ar}/^{36}\text{Ar}$ ratios, which are above or below the atmospheric value (298.56 ± 0.31 ; Lee et al., 2006). Supra-atmospheric intercepts are indicative of excess ^{40}Ar whereas sub-atmospheric ratios are too low to be due to isotopic fractionation (Oostingh et al., 2017) and are rather interpreted in term of hydrothermal alteration signature (Baksi, 2006). In addition, many samples yielded only mini–plateaus (50–70% cumulative ^{39}Ar ; Jourdan et al., 2007). The latter are less robust than their plateau counterparts and should be treated with caution. They might indicate the true crystallization age, but they might equally represent minimum age values, not too far from the crystallization age (Oostingh et al., 2017). The complete description of the dating result is reported in [section S2 of Supplementary materials](#).

For Val d’Adige, the basalt BAL1 and basanite BAL7 $^{40}\text{Ar}/^{36}\text{Ar}$ intercepts are similar and slightly sub–atmospheric (BAL1 = 266 ± 23 and BAL7 = 264 ± 15 ; [Table 3](#); [Fig. 5 a, c](#)), which allow equally calculating a plateau age of 41.69 ± 0.37 Ma ([Table 3](#); [Fig. 5b](#)) and a mini–plateau age of 41.98 ± 0.20 Ma ([Table 3](#); [Fig. 5d](#)), respectively.

TER1 and BOL1 were analysed for the Lessini Mts. district and yielded different $^{40}\text{Ar}/^{36}\text{Ar}$ and intercept ages. The basalt TER1 shows sub–atmospheric $^{40}\text{Ar}/^{36}\text{Ar}$ intercept (253 ± 25 ; [Table 3](#); [Fig. 5e](#)) defining a mini–plateau age of 45.21 ± 0.11 Ma ([Fig. 5f](#)). The $^{40}\text{Ar}/^{36}\text{Ar}$ intercept of basanite BOL1 is 278 ± 19 ([Table 3](#); [Fig. 5g](#)), close to the atmospheric $^{40}\text{Ar}/^{36}\text{Ar}$ ratio. This sample yielded a mini–plateau age of 38.73 ± 0.44 Ma ([Table 3](#); [Fig. 5h](#)).

1382
1383
1384
1385
1386
1387
1388
1389
1390
1391
1392
1393
1394
1395
1396
1397
1398
1399
1400
1401
1402
1403
1404
1405
1406
1407
1408
1409
1410
1411
1412
1413
1414
1415
1416
1417
1418
1419

432 For the basaltic trachyandesite EU52 both amphibole and plagioclase were analysed. The amphibole
433 is characterized by a $^{40}\text{Ar}/^{36}\text{Ar}$ intercept (295 ± 14 ; [Table 3](#); [Fig. 5i](#)) indistinguishable from
434 atmosphere, and yielded a mini-plateau age of 32.35 ± 0.09 Ma ([Fig. 5j](#)). The plagioclase $^{40}\text{Ar}/^{36}\text{Ar}$
435 intercept value is supra-atmospheric (397 ± 19 ; [Table 3](#); [Fig. 5k](#)), indicating excess ^{40}Ar . Using the
436 latter value, we obtained a plateau age of 32.16 ± 0.06 Ma ([Table 3](#); [Fig. 5l](#)). The alkali-feldspar
437 separate of the basaltic trachyandesite EU8B shows a value of 305 ± 99 ([Table 3](#); [Fig. 5m](#)) for the
438 $^{40}\text{Ar}/^{36}\text{Ar}$ intercept, which is indistinguishable from the atmospheric ratio and allows calculating a
439 plateau age of 32.17 ± 0.32 Ma ([Table 3](#); [Fig. 5n](#)). The feldspar separate of the latite EU13A yielded
440 a $^{40}\text{Ar}/^{36}\text{Ar}$ intercept of 349 ± 136 ([Fig. 5o](#)) and a plateau age of 32.34 ± 0.51 Ma ([Fig. 5p](#)). The
441 $^{40}\text{Ar}/^{36}\text{Ar}$ intercept age for the biotite separate of trachyte EU4 is 328 ± 43 ([Table 3](#); [Fig. 5q](#)) and
442 defines a plateau age of 32.09 ± 0.29 Ma ([Fig. 5r](#)). Also for the sanidine separate of rhyolite EU5B
443 the $^{40}\text{Ar}/^{36}\text{Ar}$ intercept is slightly supra-atmospheric (343 ± 58 ; [Fig. 5s](#)); the calculated plateau age is
444 32.30 ± 0.52 Ma ([Table 3](#); [Fig. 5t](#)). The sanidine separate of rhyolite EU9 shows a $^{40}\text{Ar}/^{36}\text{Ar}$ intercept
445 value (315 ± 68 ; [Table 3](#); [Fig. 5u](#)) indistinguishable from atmosphere and we obtained a plateau age
446 of 32.17 ± 0.27 Ma ([Table 3](#); [Fig. 5v](#)). It is clear that irrespective to the lithology all analysed
447 Euganean samples yielded nearly indistinguishable ages, allowing to calculate a mean weighted age
448 of 32.21 ± 0.09 Ma.

1420
1421
1422
1423
1424
1425
1426
1427
1428

449 The basanite from the Marosticano district, LB1, yielded the youngest integrated age of the VVP
450 samples analysed at WAAIF using the ARGUS VI mass spectrometer. It did not return isochron and
451 plateau age, but almost all the steps indicate apparent ages between 20.5 and 23.2 Ma ([Table 3](#); [Fig.](#)
452 [5w, x](#)).

1429
1430
1431
1432
1433
1434
1435
1436
1437
1438
1439
1440

453 Two additional basanites BI14 and 25B, from Val d'Adige and Marosticano, respectively, were
454 analysed at the Noble Gas Geochronology Laboratory of the University of Vermont using the Nu
455 Instruments Noblesse magnetic sector noble gas mass spectrometer with the purpose to expand the
456 VVP geochronological dataset. Sample BI14 yielded a $^{40}\text{Ar}/^{36}\text{Ar}$ intercept of 207 ± 138 and a mini-
457 plateau age of 40.73 ± 0.48 Ma ([Table 4](#); [Fig. 6a, b](#)). This age is similar to those recorded by BAL1

1441
1442
1443
1444
1445
1446
1447
1448
1449
1450
1451
1452
1453
1454
1455
1456
1457
1458
1459
1460
1461
1462
1463
1464
1465
1466
1467
1468
1469
1470
1471
1472
1473
1474
1475
1476
1477
1478
1479
1480
1481
1482
1483
1484
1485
1486
1487
1488
1489
1490
1491
1492
1493
1494
1495
1496
1497
1498
1499

and BAL7. As occurred for LB1, also the Marosticano basanite 25B did not provide ages (Table 4; Fig. 6c, d). However, for both Marosticano samples almost all the steps indicate apparent ages of ~ 22 – 23 Ma (Fig. 6d).

| General characteristics | | | | Isochron characteristics | | | | | Plateau characteristics | | | |
|-------------------------|-------------------------|------------|-------------|---|----|---|------|-------|------------------------------------|-------------------------------------|------|-------|
| Sample | Lithology | Instrument | Separate | Inverse isochron age (Ma, $\pm 2\sigma$) | n | $^{40}\text{Ar}/^{36}\text{Ar}$ intercept ($\pm 2\sigma$) | MSWD | P (%) | Plateau age (Ma, $\pm 2\sigma$) | Total ^{39}Ar released (%) | MSWD | P (%) |
| <i>Val d'Adige</i> | | | | | | | | | | | | |
| BAL1 | Basalt | ARGUS VI | Groundmass | 41.70 \pm 0.82 | 16 | 266 \pm 23 | 0.78 | 69 | 41.69 \pm 0.37 | 75 | 0.39 | 98 |
| BAL7 | Basanite | ARGUS VI | Groundmass | <i>41.95 \pm 0.46</i> | 15 | 264 \pm 15 | 0.82 | 64 | <i>41.98 \pm 0.20</i> | 60 | 0.25 | 100 |
| <i>Lessini Mts.</i> | | | | | | | | | | | | |
| TER1 | Basalt | ARGUS VI | Groundmass | <i>45.21 \pm 0.15</i> | 12 | 253 \pm 25 | 1.00 | 44 | <i>45.21 \pm 0.11</i> | 57 | 0.83 | 61 |
| BOL1 | Basanite | ARGUS VI | Groundmass | <i>40.60 \pm 1.76</i> | 17 | 278 \pm 19 | 0.75 | 74 | <i>38.73 \pm 0.44</i> | 62 | 0.99 | 46 |
| <i>Euganean Hills</i> | | | | | | | | | | | | |
| EU52 | Basaltic trachyandesite | ARGUS VI | Amphibole | <i>32.37 \pm 0.12</i> | 10 | 295 \pm 14 | 0.52 | 85 | <i>32.35 \pm 0.09</i> | 67 | 0.48 | 89 |
| | | | Plagioclase | 32.16 \pm 0.08 | 21 | 397 \pm 19 | 0.65 | 87 | 32.16 \pm 0.06 | 100 | 0.58 | 93 |
| EU8B | Basaltic trachyandesite | MAP 215–50 | Feldspar | 32.11 \pm 0.98 | 15 | 305 \pm 99 | 0.85 | 61 | 32.17 \pm 0.32 | 100 | 0.79 | 68 |
| EU13A | Latite | MAP 215–50 | Feldspar | 31.96 \pm 1.13 | 14 | 349 \pm 136 | 0.52 | 91 | 32.34 \pm 0.51 | 88 | 0.53 | 91 |
| EU4 | Trachyte | MAP 215–50 | Biotite | 31.83 \pm 0.50 | 14 | 328 \pm 43 | 0.88 | 57 | 32.09 \pm 0.29 | 100 | 0.97 | 48 |
| EU5B | Rhyolite | MAP 215–50 | Sanidine | 31.87 \pm 0.79 | 15 | 343 \pm 58 | 0.86 | 59 | 32.30 \pm 0.52 | 100 | 1.00 | 45 |
| EU9 | Rhyolite | MAP 215–50 | Sanidine | 32.02 \pm 0.67 | 14 | 315 \pm 68 | 0.51 | 91 | 32.17 \pm 0.27 | 100 | 0.48 | 94 |
| <i>Marosticano</i> | | | | | | | | | | | | |
| LB1 | Basanite | ARGUS VI | Groundmass | No isochron age | | | | | No plateau age | | | |

Data in italics are derived from mini-plateaus (50–70% ^{39}Ar released) and are considered minimum ages only, bold font represents statistically significant plateau ages. Mean square weighted deviation (MSWD) for isochron, plateau, and mini-plateau, number of analyses included in the isochron, $^{40}\text{Ar}/^{36}\text{Ar}$ intercept, percentage of ^{39}Ar degassed used in the plateau calculation, probability (P) for isochron, plateau and mini-plateau are indicate. Analytical uncertainties on the ages and $^{40}\text{Ar}/^{36}\text{Ar}$ intercepts are quoted at 2 sigma (2σ) confidence levels.

Table 3. Summary table of $^{40}\text{Ar}/^{39}\text{Ar}$ results for Val d'Adige, Lessini Mts., Euganean Hills, and Marosticano samples analysed at Western Australian Argon Isotope Facility (WAAIF).

| General characteristics | | | Isochron characteristics | | | | Plateau characteristics | | | |
|-------------------------|-----------|-----------|---|---|---|------|----------------------------------|-------------------------------------|------|-------|
| Sample | Lithology | Separate | Inverse isochron age (Ma, $\pm 2\sigma$) | n | $^{40}\text{Ar}/^{36}\text{Ar}$ intercept ($\pm 2\sigma$) | MSWD | Plateau age (Ma, $\pm 2\sigma$) | Total ^{39}Ar released (%) | MSWD | P (%) |
| <i>Val d'Adige</i> | | | | | | | | | | |
| BI14 | Basanite | Groudmass | 42.2 \pm 8.2 | 7 | 207 \pm 138 | 11.3 | 40.73 \pm 0.48 | 57 | 0.8 | 45 |
| <i>Marosticano</i> | | | | | | | | | | |
| 25B | Basanite | Groudmass | No isochron age | | | | No plateau age | | | |

Data in italics are derived from mini-plateau (50–70% ^{39}Ar released) and are considered minimum ages only. Mean square weighted deviation (MSWD) for isochron and mini-plateau, number of analyses included in the isochron, $^{40}\text{Ar}/^{36}\text{Ar}$ intercept, percentage of ^{39}Ar degassed used in the plateau calculation and probability (P) for mini-plateau are indicated. Analytical uncertainties on the ages and $^{40}\text{Ar}/^{36}\text{Ar}$ intercept are quoted at 2 sigma (2σ) confidence levels.

Table 4. Summary table of $^{40}\text{Ar}/^{39}\text{Ar}$ results for Val d'Adige, and Marosticano samples analysed at the Noble Gas Geochronology Laboratory of the University of Vermont with Nu Instruments Noblesse magnetic sector noble gas mass spectrometer.

1582
1583
1584
1585
1586
1587
1588
1589
1590
1591
1592
1593
1594
1595
1596
1597
1598
1599
1600
1601
1602
1603
1604
1605
1606
1607
1608
1609
1610
1611
1612
1613
1614
1615
1616
1617
1618
1619
1620
1621
1622
1623
1624
1625
1626
1627
1628
1629
1630
1631
1632
1633
1634
1635
1636
1637
1638
1639
1640
1641

Figure 5. $^{39}\text{Ar}/^{40}\text{Ar}$ vs. $^{36}\text{Ar}/^{40}\text{Ar}$ inverse isochrons and $^{40}\text{Ar}/^{39}\text{Ar}$ apparent age and K/Ca spectra, plotted against the cumulative percentage of ^{39}Ar released for VVP rocks analysed at Curtin University. Plateau ages (bold) are inverse isochron intercept corrected. Mini-plateaus (50–70% cumulative ^{39}Ar) are indicated in italics. Mean square weighted deviation (MSWD) and probability of fit (P) are indicated. Errors on plateau ages are quoted at 2σ and do not include systematic errors (*i.e.*, uncertainties on the age of the monitor and on the decay constant). These plots are obtained at Curtin University within the Western Australian Argon Isotope Facility (WAAIF) of the John de Laeter Centre using ARGUS VI and MAP 215–50 mass spectrometers. Abbreviations: gm = groundmass; bt = biotite; san = sanidine; fsp = feldspar; pl = plagioclase; amph = amphibole. **[2 pages, 2 columns fitting]**

Figure 6. $^{39}\text{Ar}/^{40}\text{Ar}$ vs. $^{36}\text{Ar}/^{40}\text{Ar}$ plot and $^{40}\text{Ar}/^{39}\text{Ar}$ apparent age and K/Ca spectra, plotted against the cumulative percentage of ^{39}Ar released for VVP rocks analysed at University of Vermont. The mini-plateau age is inverse isochron intercept ($^{40}\text{Ar}/^{39}\text{Ar}$) corrected and indicated in italics. Mean square weighted deviation (MSWD) and probability of fit (P) are reported. Error on the plateau age is quoted at 2σ . These plots are obtained at the Noble Gas Geochronology Laboratory of the University of Vermont with Nu Instruments Noblesse magnetic sector noble gas mass spectrometer. Abbreviations: gm = groundmass. **[1 column fitting]**

10. DISCUSSION

10.1 Temperature and pressure of mineral crystallization

Crystallization temperature and pressure are calculated mainly through analysis of mineral and whole rock pairs using the recent Fe–Mg cation exchange reaction [$K_{\text{Fe-Mg}} = (\text{Fe}^{\text{clinopyroxene}}/\text{Fe}^{\text{melt}}) \times (\text{Mg}^{\text{melt}}/\text{Mg}^{\text{clinopyroxene}})$]; [Table 5](#)] (Putirka, 2008; Neave and Putirka, 2017). For each VVP district, we used equilibrium clinopyroxene–melt pairs having pyroxene–melt $K_{\text{Fe-Mg}}$ close to 0.27 ± 0.03 , as indicated by Putirka et al. (2003). Furthermore, the difference between predicted and observed diopside+hedenbergite (DiHd) values should approach zero as indicated by Neave and Putirka (2017; see also Putirka et al., 2009) and Mollo et al. (2013; 2017). Calculated clinopyroxene crystallization temperatures and pressure for all VVP districts are reported in [Table 5](#) and in Figure 7. For Val d’Adige, Lessini Mts, and Marosticano calculated temperature ranges are similar (Val d’Adige: $T = 1142^\circ\text{C} - 1174^\circ\text{C}$; Lessini Mts. $T = 1148 - 1204^\circ\text{C}$; Marosticano: $T = 1209 - 1219^\circ\text{C}$; [Table 5](#); [Fig. 7](#)) and higher than those for Euganean Hills ($T = 1129 - 1162^\circ\text{C}$; [Table 5](#); [Fig. 7](#)). Lessini Mts. clinopyroxene–melt pairs record the highest pressure values ($P = 0.4 - 0.8$ GPa; [Table 5](#); [Fig. 7](#)), while those from the Euganean Hills are the lowest ($P = 0.1 - 0.4$ GPa; [Table 5](#); [Fig. 7](#)). Val d’Adige and Marosticano clinopyroxenes record narrow pressure ranges (Val d’Adige: $P = 0.3 - 0.6$ GPa; Marosticano: $P = 0.5 - 0.6$; [Table 5](#); [Fig. 7](#))

It is interesting to note that several of the investigated rocks (*e.g.*, samples BOL1, LB1, and 25B) contain small fragments of mantle peridotite xenoliths, implying that magmas rose rapidly from the mantle to the surface. Therefore, it can be proposed that the highest calculated pressure, measured in Lessini Mts. (~ 0.8 GPa) likely corresponds to the topmost mantle and can be used to infer the depth of the Moho during the VVP activity. Hence, the estimated depth of the Moho under the magmatic region is ~ 26 km, in accordance with geophysical data indicating relatively thin continental crust of ~ 28 km under the VVP (Ansorge et al., 1992; Giese and Bunn, 1992; Grad et al., 2009).

1702
 1703
 1704
 1705
 1706
 1707
 1708
 1709
 1710
 1711
 1712
 1713
 1714
 1715
 1716
 1717
 1718
 1719
 1720
 1721
 1722
 1723
 1724
 1725
 1726
 1727
 1728
 1729
 1730
 1731
 1732
 1733
 1734
 1735
 1736
 1737
 1738
 1739
 1740
 1741
 1742

| Sample | Lithology | Cpx | | Clinopyroxene compositions | | | | | | | | | | | Determined pressures and temperatures | | | |
|-----------------------|-------------------|-------|---------|----------------------------|------------------|--------------------------------|--------------------|------|------|------|-------------------|------------------|--------------------------------|-------|---------------------------------------|---------|------------|------------|
| | | | | SiO ₂ (wt.%) | TiO ₂ | Al ₂ O ₃ | FeO _{tot} | MnO | MgO | CaO | Na ₂ O | K ₂ O | Cr ₂ O ₃ | Tot | T (°C) Eqn. 33 | P (GPa) | DiHd error | Kd (Fe-Mg) |
| <i>Val d'Adige</i> | | | | | | | | | | | | | | | | | | |
| BAL7 | Basanite | cpx 1 | point 1 | 47.93 | 2.25 | 4.73 | 6.57 | 0.06 | 14.2 | 22.6 | 0.36 | 0.0 | 0.02 | 98.76 | 1142 | 0.3 | 0.02 | 0.28 |
| | | | point 2 | 48.20 | 2.26 | 4.64 | 6.39 | 0.14 | 14.5 | 22.5 | 0.38 | 0.0 | 0.03 | 98.70 | 1150 | 0.4 | 0.01 | 0.28 |
| | | cpx 2 | point 1 | 48.64 | 2.23 | 4.35 | 6.55 | 0.10 | 14.4 | 22.4 | 0.42 | 0.0 | 0.00 | 99.23 | 1137 | 0.3 | 0.05 | 0.28 |
| | | | point 2 | 47.77 | 2.34 | 4.96 | 6.61 | 0.12 | 14.3 | 22.0 | 0.37 | 0.0 | 0.00 | 98.57 | 1167 | 0.5 | -0.01 | 0.29 |
| | | | point 3 | 48.02 | 2.14 | 4.91 | 6.45 | 0.11 | 14.4 | 22.0 | 0.39 | 0.0 | 0.02 | 98.51 | 1174 | 0.6 | -0.03 | 0.29 |
| | | | point 4 | 48.49 | 2.12 | 4.43 | 6.22 | 0.09 | 14.5 | 22.4 | 0.35 | 0.0 | 0.00 | 98.71 | 1151 | 0.4 | 0.00 | 0.28 |
| <i>Lessini Mts.</i> | | | | | | | | | | | | | | | | | | |
| TER1 | Basalt | cpx 1 | point 1 | 50.29 | 1.07 | 3.36 | 5.15 | 0.11 | 15.8 | 22.7 | 0.31 | 0.0 | 0.39 | 99.28 | 1195 | 0.6 | -0.15 | 0.30 |
| | | | point 2 | 50.38 | 1.12 | 3.47 | 5.10 | 0.11 | 15.7 | 23.2 | 0.31 | 0.0 | 0.35 | 99.83 | 1185 | 0.5 | -0.14 | 0.30 |
| | | | point 3 | 49.47 | 1.60 | 4.26 | 6.10 | 0.13 | 14.9 | 22.7 | 0.29 | 0.0 | 0.02 | 99.53 | 1204 | 0.7 | -0.16 | 0.30 |
| BOL1 | Basanite | cpx 1 | point 1 | 47.88 | 1.98 | 5.32 | 6.56 | 0.10 | 14.3 | 22.0 | 0.55 | 0.0 | 0.08 | 98.84 | 1190 | 0.8 | -0.08 | 0.30 |
| | | | point 2 | 47.92 | 1.99 | 4.88 | 6.14 | 0.07 | 14.5 | 22.5 | 0.71 | 0.0 | 0.00 | 98.80 | 1148 | 0.4 | -0.01 | 0.29 |
| <i>Euganean Hills</i> | | | | | | | | | | | | | | | | | | |
| EU1A B | Basaltic andesite | cpx 1 | point 1 | 49.14 | 2.11 | 4.12 | 8.65 | 0.15 | 14.8 | 19.8 | 0.32 | 0.0 | 0.49 | 99.73 | 1136 | 0.2 | 0.03 | 0.28 |
| | | | point 1 | 50.23 | 1.95 | 3.18 | 10.48 | 0.20 | 13.1 | 19.6 | 0.33 | 0.0 | 0.05 | 99.20 | 1143 | 0.3 | -0.01 | 0.28 |
| | | cpx 2 | point 2 | 49.68 | 1.87 | 2.88 | 13.71 | 0.22 | 11.9 | 19.1 | 0.37 | 0.0 | 0.05 | 99.95 | 1132 | 0.1 | 0.02 | 0.27 |
| | | | point 1 | 50.93 | 1.19 | 3.61 | 7.64 | 0.11 | 15.4 | 19.7 | 0.42 | 0.0 | 0.74 | 99.81 | 1162 | 0.4 | -0.03 | 0.28 |
| | | cpx 3 | point 2 | 50.09 | 1.33 | 3.44 | 7.45 | 0.20 | 15.3 | 20.2 | 0.32 | 0.0 | 0.73 | 99.15 | 1141 | 0.2 | -0.01 | 0.28 |
| | | | point 3 | 50.58 | 1.43 | 3.18 | 8.17 | 0.14 | 15.4 | 20.0 | 0.31 | 0.0 | 0.33 | 99.58 | 1141 | 0.2 | 0.04 | 0.27 |
| | | | point 4 | 50.34 | 1.96 | 3.77 | 8.85 | 0.13 | 14.2 | 20.3 | 0.34 | 0.0 | 0.22 | 100.1 | 1142 | 0.3 | -0.01 | 0.28 |
| | | | | | | | | | | 2 | 4 | | 1 | | 8 | | | |

1743
1744
1745
1746
1747
1748
1749
1750
1751
1752
1753
1754
1755
1756
1757
1758
1759
1760
1761
1762
1763
1764
1765
1766
1767
1768
1769
1770
1771
1772
1773
1774
1775
1776
1777
1778
1779
1780
1781
1782
1783

| | | | | | | | | | | | | | | | | | | | |
|--------------------|------------|----------|------------|------------|-------|------|------|------|-----------|-----------|-----------|----------|----------|-------|-------|------|-------|-------|------|
| | | | point 5 | 49.49 | 1.88 | 3.69 | 9.43 | 0.17 | 14.3 4 | 19.7 5 | 0.30 | 0.0 3 | 0.18 | 99.26 | 1140 | 0.2 | -0.01 | 0.28 | |
| | | | point 6 | 49.31 | 2.12 | 3.65 | 9.71 | 0.17 | 14.0 8 | 19.9 3 | 0.32 | 0.0 0 | 0.13 | 99.44 | 1129 | 0.1 | 0.01 | 0.28 | |
| <i>Marosticano</i> | | | | | | | | | | | | | | | | | | | |
| | LB1 | Basanite | cpx 1 | point 1 | 44.47 | 3.44 | 7.56 | 7.12 | 0.12 | 13.0 8 | 22.1 3 | 0.43 | 0.0 0 | 0.22 | 98.57 | 1219 | 0.6 | 0.00 | 0.30 |
| | | | cpx 2 | point 1 | 49.64 | 1.08 | 3.87 | 5.17 | 0.08 | 15.8 7 | 22.1 4 | 0.52 | 0.0 0 | 0.24 | 98.61 | 1209 | 0.5 | -0.05 | 0.30 |

Table 5. Clinopyroxene compositions in wt.% from Val d'Adige, Lessini Mts., Euganean Hills, and Marosticano magmatic products and calculated temperatures and pressures using the equation 33 from Putirka (2008) and the equation from Neave and Putirka (2017), respectively. Only clinopyroxenes with the appropriate range in $K_{\text{Fe-Mg}}^{\text{cpx/melt}}$ values ($K_{\text{Fe-Mg}} = 0.27 \pm 0.03$; Putirka et al., 2003; Putirka, 2008) and DiHd error ($\text{DiHd}_{\text{predicted-observed}}$; Neave and Putirka, 2017; Mollo et al., 2013, 2017) approaching zero are presented.

The corresponding whole rock compositions are in [Table 1](#).

Abbreviations: cpx = clinopyroxene; DiHd = Diopside+Hedenbergite solid solution.

1784
1785
1786
1787
1788
1789
1790
1791
1792
1793
1794
1795
1796
1797
1798
1799
1800
1801
1802
1803
1804
1805
1806
1807
1808
1809
1810
1811
1812
1813
1814
1815
1816
1817
1818
1819
1820
1821
1822
1823
1824
1825
1826
1827
1828
1829
1830
1831
1832
1833
1834
1835
1836
1837
1838
1839
1840
1841
1842
1843

Figure 7. Clinopyroxene/melt equilibrium temperatures (°C) and pressures (GPa) of Val d'Adige, Lessini Mts., Euganean Hills, and Marosticano magmatic products calculated from equation 33 of Putirka (2008) and the equation from Neave and Putirka (2017), respectively.

10.2 The mantle source of VVP magmatism

Most analysed magmatic products of the VVP show mg# significantly lower than typical primary magmas (Table 1), *i.e.*, they have undergone at least some fractional crystallization before being erupted to the surface. However, at least a few rocks have mg# higher than 60 and, as mentioned before, host millimeter to centimeter-sized fragments of peridotite xenoliths, which point to fast transport of magma from mantle depths to the surface. Conservatively, we consider only the trace elements contents of the less evolved VVP samples exhibiting MgO > 8 wt.% and mg# > 55 (BAL7, TER1, BOL1, and LB1) to constrain the nature and evolution of their mantle source. The selected samples are characterized by low LILE/HFSE, LREE/HFSE ratios, and high-Nb contents (Fig. 4a, b). Notably, also slightly more evolved basic samples, including those from the Euganean Hills, display similar trace element features. These trace element and REE patterns are clearly distinct from those of the Periadriatic Central Alps calc-alkaline and sub-alkaline products with arc signature (Bergomi et al., 2015; Fig. 4a, b) and are instead consistent with the within-plate signature already noticed by previous studies on the VVP (Milani et al., 1999; Beccaluva et al., 2007; Macera et al., 2008; Fig. 4a, b). In fact, Beccaluva et al., (2001, 2007) invoked an Ocean Island Basalts (OIB)-like mantle source (Sun and McDonough, 1989) for these magmas, justifying the deviations of VVP samples from typical OIB trace element patterns (Fig. 4b), with the identification of a spinel lherzolite enriched with hydrated-carbonated components as potential source. However, large uncertainties were attributed to the mantle region where melting occurred.

Using the geochemical features of the sample suite of this study we determined i) the depth of partial melting; ii) the mineralogical and geochemical features of melting mantle; and iii) the geodynamic evolution that may be responsible for the enrichment/depletion processes in the VVP mantle source region.

10.2.1 The depth of the VVP mantle partial melting

The trace elements patterns and ratios of the selected VVP basic-ultrabasic rocks were at first used

1904
1905
1906
560 to constrain the depth of the VVP mantle source, *i.e.*, if it was in the garnet or in the spinel stability
1907
1908
561 field. The steep middle (M)–HREE profiles of the selected VVP samples suggest a possible presence
1909
1910
562 of garnet in the mantle source, as this mineral progressively takes up the HREE over MREE
1911
1912
563 ($Kd_{Sm}^{garnet/melt}/Kd_{Yb}^{garnet/melt} \sim 10^{-3}$; *e.g.*, van Westrenen et al., 2001; Niu et al., 2011). When garnet is
1914
1915
564 no longer stable, clinopyroxene becomes the sole peridotitic phase that can accommodate REE
1916
1917
565 (Hellebrand et al., 2002). This mineral has an almost equal partition coefficient for MREE and HREE
1918
1919
566 during melting ($Kd_{Sm}^{clinopyroxene/melt}/Kd_{Yb}^{clinopyroxene/melt}$ close 1.0; Green et al., 2000; Niu et al., 2011),
1920
1921
567 imposing melt REE profiles with almost flat M–HREE patterns. Taking this into account, values of
1922
1923
568 $(Sm/Yb)_N$ higher than 1.0 are considered evidence for garnet signature in OIBs (Niu et al., 2011).
1924
1925
569 Such consideration may apply also to VVP basic–ultrabasic samples [$(Sm/Yb)_N = 3.9$ to 6.1].
1926
1927
570 Lanthanum is highly incompatible during melting and difficult to accommodate in both garnet and
1928
1929
571 clinopyroxene. This implies that any fertile or moderately fertile mantle source in the early stages of
1930
1931
572 melting, produces melts with positive fractionated REE pattern [$(La/Yb)_N \gg 1$] in both garnet or
1932
1933
573 spinel stability fields. However, by combining REE ratios such as La/Yb and Dy/Yb, it is possible to
1934
1935
574 constrain the presence or absence of garnet in the mantle source and consequently inferring the
1936
1937
575 melting depth (*e.g.*, Thirlwall et al., 1994). In fact, Dy/Yb is fractionated in the presence of residual
1938
1939
576 garnet and this effect is seen for relatively high degrees of melting (Bogaard and Wörner, 2003). On
1940
1941
577 the contrary, the presence of spinel in the source does not significantly fractionate La, Dy, and Yb as
1942
1943
578 these elements are all moderately incompatible in this mineral. Therefore, in the spinel stability field,
1944
1945
579 La/Yb is only slightly fractionated for small degrees of melting, and Dy/Yb is not fractionated at all
1946
1947
580 (Bogaard and Wörner, 2003).
1948
1949
581 La/Yb vs. Dy/Yb of melts calculated for non-modal batch melting model (Shaw, 1970) are compared
1950
1951
582 to the selected basic–ultrabasic VVP magmatic products (Fig. 8) to confine the chemical composition
1952
1953
583 and mineralogy of the VVP magma source(s), as well as to estimate the degree of partial melting.
1954
1955
584 The calculated melts were obtained for fertile and/or moderately fertile lherzolites (modal
1956
1957
585 clinopyroxene 15–20%; Table 6) with garnet or spinel in the peridotite assemblage. In addition, we
1958
1959
1960
1961
1962
1963

1964
1965
1966
1967
1968
1969
1970
1971
1972
1973
1974
1975
1976
1977
1978
1979
1980
1981
1982
1983
1984
1985
1986
1987
1988
1989
1990
1991
1992
1993
1994
1995
1996
1997
1998
1999
2000
2001
2002
2003
2004
2005
2006
2007
2008
2009
2010
2011
2012
2013
2014
2015
2016
2017
2018
2019
2020
2021
2022
2023

586 modelled also the possible presence of metasomatic phases (i.e, phlogopite and amphibole) in the
587 lherzolitic source. The relative starting and melting modes of (phlogopite-bearing) garnet and
588 (phlogopite-bearing) spinel lherzolites are reported in [Table 6](#). In Figure 8 the selected VVP samples
589 as well as basic–ultrabasic magmatic products from previous studies (Beccaluva et al., 2007) lie
590 closer to the melting curves of the garnet peridotites rather than of the spinel peridotites. In particular,
591 the basanitic samples and the majority of the alkaline primary lavas from Lessini Mts. (data from
592 Beccaluva et al., 2007) cluster around 3–4% of melting of a phlogopite enriched-garnet mantle
593 source. On the other hand, the basalt TER1, which can be classified as tholeiite for its normative
594 character (see [Table 1](#)), and the tholeiitic samples from the Lessini Mts. (data from Beccaluva et al.,
595 2007) require slightly higher melting degrees (about 5–6%), and perhaps an anhydrous (*i.e.*,
596 phlogopite and amphibole–free) source.

597 This melting model and the REE patterns clearly indicate that for the selected samples partial melting
598 occurred dominantly within the garnet–peridotite stability field, *i.e.*, at depths higher than about 70
599 km (*e.g.*, Green and Ringwood, 1970; Frost, 2008; Ziberna et al., 2013). Geophysical data indicate
600 the depth of lithosphere–asthenosphere boundary under the VVP at ~100km (Panza and Suhaldoc,
601 1990), therefore we infer that melting occurred within the deep lithosphere. This is also consistent
602 with the inferred presence in the VVP mantle source of phlogopite (see section 10.2.2), a mineral that
603 would rapidly melt out in the asthenospheric mantle wedge (Frost, 2006 and references therein)
604 overlying the subducting European slab.

605 Unlike VVP basanites and basalt, the calc–alkaline and sub–alkaline basic dykes and intrusive rocks
606 from the Periadriatic Central Alps magmatism exhibit flat HREE profile (Bergomi et al. 2015; Fig.
607 4a, b) more consistent with a spinel-bearing peridotite. This implies a relatively shallower melting
608 depth for the orogenic compared to the intraplate VVP magmas.

2024
2025
2026
2027
2028
2029
2030
2031
2032
2033
2034
2035
2036
2037
2038
2039
2040
2041
2042
2043
2044
2045
2046
2047
2048
2049
2050
2051
2052
2053
2054
2055
2056
2057
2058
2059
2060
2061
2062
2063
2064

| | olivine | orthopyroxene | clinopyroxene | spinel | garnet | phlogopite |
|---|---------|---------------|---------------|--------|--------|------------|
| Garnet lherzolite | | | | | | |
| Mode of the source | 0.57 | 0.16 | 0.14 | — | 0.13 | — |
| Melting mode | 0.03 | 0.03 | 0.44 | — | 0.50 | — |
| Spinel lherzolite | | | | | | |
| Mode of the source | 0.56 | 0.22 | 0.19 | 0.03 | — | — |
| Melting mode | 0.10 | 0.20 | 0.68 | 0.02 | — | — |
| Phlogopite-bearing garnet lherzolite | | | | | | |
| Mode of the source | 0.60 | 0.14 | 0.15 | — | 0.03 | 0.08 |
| Melting mode | 0.10 | 0.10 | 0.30 | — | 0.34 | 0.16 |
| Phlogopite-bearing spinel lherzolite | | | | | | |
| Mode of the source | 0.58 | 0.15 | 0.18 | 0.03 | — | 0.06 |
| Melting mode | 0.10 | 0.10 | 0.54 | 0.10 | — | 0.16 |

Table 6. Source and melting mineral phases used in the non-modal batch model. Mineral modes of garnet lherzolite and spinel lherzolite in primitive mantle are taken from McDonough and Rudnick (1998). Mineral modes of phlogopite-bearing garnet lherzolite and phlogopite-bearing spinel are modified from Pfänder et al. (2018 and reference therein). Values are weight fractions.

2065
2066
2067
2068
2069
2070
2071
2072
2073
2074
2075
2076
2077
2078
2079
2080
2081
2082
2083
2084
2085
2086
2087
2088
2089
2090
2091
2092
2093
2094
2095
2096
2097
2098
2099
2100
2101
2102
2103
2104
2105
2106
2107
2108
2109
2110
2111
2112
2113
2114
2115
2116
2117
2118
2119
2120
2121
2122
2123

Figure 8. Dy/Yb vs. La/Yb in selected basic–ultrabasic VVP samples (large symbols) and alkaline and tholeiitic Lessini Mts. magmatic products from Beccaluva et al. (2007; small symbols) having MgO > 8 wt.% and mg# > 55. Also shown are non–modal batch partial melting curves for different mantle sources: i) garnet lherzolite (thick continuous line); ii) spinel lherzolite (thin continuous line); iii) phlogopite–bearing garnet lherzolite (thick dashed line); iv) phlogopite–bearing spinel lherzolite (thin dashed line). The partition coefficients are from GERM (<http://earthref.org/>). The source and melting mineral modes are reported in Table 6. Mineral modes of garnet lherzolite and spinel lherzolite in primitive mantle are taken from McDonough and Rudnick (1998). Mineral modes of phlogopite-bearing garnet lherzolite and phlogopite-bearing spinel are modified from Pfänder et al. (2018 and reference therein). The source compositions for phlogopite–garnet lherzolite and phlogopite–spinel lherzolite are modified from Pfänder et al. (2018); the source compositions for garnet lherzolite and spinel lherzolite are those of the primitive mantle from McDonough and Sun (1995). Numbers on model curves indicate the percentage of melting.

10.2.2 Is phlogopite really the K (Rb)–bearing residual phase in the VVP mantle source?

Although all the selected basic–ultrabasic samples have potassic affinity, on the primitive–mantle normalized multi–element diagram K and Rb are depleted, whereas Ba is enriched with respect to neighboring elements (Fig. 4b). Such features suggest the presence of a residual K (Rb)–bearing phase (i.e., amphibole and/or phlogopite) in the mantle source region (Greenough et al., 1988; Wilson and Downes, 1992). Previously, we inferred that the partial melting of the VVP mantle source took place probably within the garnet stability field (i.e., at pressures higher than 2.5 GPa; Robinson and Wood, 1998). The stability field of amphibole in upper mantle rocks ranges from 0.5 to 4 GPa at temperatures in the range of 970–1170°C (e.g., Konzett et al., 1997; Frost, 2006; Mandler and Grove, 2016), whereas that of phlogopite ranges from 1 to 9 GPa and temperatures in the range of 800–1500°C (e.g., Sato et al., 1997; Konzett and Ulmer, 1999; Conceição and Green, 2004; Sokol et al., 2017). Therefore, both phases are thus stable at the mantle depths where VVP magmas formed. However, the calculated crystallization temperatures, based on the empirical equation of Putirka (2008) for the clinopyroxene/melt equilibrium, range from ~ 1150 to ~ 1220°C for the selected VVP basanites (Table 5), slightly lower than the temperature of ~ 1250°C obtained by Beccaluva et al. (2007) for the same lithotype. The temperatures of crystallization of the VVP clinopyroxenes are generally above than the stability temperature of amphibole. Taking this into account and considering its chemical–physical properties (Zanazzi and Pavese, 2002; Gemmi et al., 2008; Gatta et al., 2011) phlogopite appears to be the most likely potassic residual mantle phase. The hypothesis of amphibole as residual phase in the VVP mantle source is also ruled out by the REE patterns of VVP samples. Calcic amphiboles have affinity for the MREE (Gd to Ho) relative the HREE (Er to Lu; Tiepolo et al., 2007; Meyzen et al., 2016). Therefore, basanitic melts derived from an amphibole–bearing mantle source are fingerprinted by a typical convex–upward pattern in the MREE (Meyzen et al., 2016), which is absent in the VVP samples. Further evidence for the presence of phlogopite as the K-bearing residual phase is the Ba/Rb ratio. Both Rb and Ba are more compatible in phlogopite ($D_{\text{Rb}}^{\text{phlogopite/melt}} = 1.44$, $D_{\text{Ba}}^{\text{phlogopite/melt}} = 1.03$; LaTourette et al., 1995; Furman and Graham, 1999; Tiepolo et al.,

2183
2184
2185
654 2007) than in amphibole ($D_{\text{Rb}}^{\text{amphibole/melt}} = 0.15$, $D_{\text{Ba}}^{\text{amphibole/melt}} = 0.29$; LaTourette et al., 1995;
2186
2187
655 Furman and Graham, 1999; Schmidt et al., 1999). Considering these partition coefficients, residual
2188
2189
656 amphibole would produce melts enriched in Ba/Rb (> 50), the opposite being true for phlogopite ($<$
2190
2191
657 20; Furman and Graham, 1999; Tiepolo et al., 2007; Meyzen et al., 2016). The relatively low Ba/Rb
2192
2193
658 (10 to 20) of most VVP basic–ultrabasic products thus supports the presence of residual phlogopite
2194
2195
659 rather than of amphibole within their mantle source.

2196 2197 2198 660 2199 2200 661 **10.2.3 The origin of the VVP mantle source enrichment**

2201
2202
662 In the spider diagrams (Fig. 4a, b) as well as to the K and Rb depletions, the basic–ultrabasic VVP
2203
2204
663 magmatic products exhibit enrichments also in Ba, Sr, and P. The same positive anomalies have been
2205
2206
664 described in within–plate magmatic suites generated from an enriched mantle source metasomatized
2207
2208
665 by CO₂–rich fluids, which are able to carry Ba, Sr, and P (Yaxley et al., 1991; Ionov et al., 1996;
2209
2210
666 Beccaluva et al., 2007; Dixon et al., 2008). For example, Merle et al. (2017) suggested that basic–
2211
2212
667 ultrabasic magmatic rocks from Cameroon, which are geochemically characterized by enrichments
2213
2214
668 in LREE, Ba, Sr, and P and depletions in Zr, were derived from a mantle source that underwent
2215
2216
669 metasomatism from carbonatitic melts.

2217
2218
2219
670 In the case of VVP basic–ultrabasic magmatic rocks, CO₂–rich fluids may have been provided by the
2220
2221
671 subduction of the Tethys oceanic slab, which included calcareous metasediments and carbonated
2222
2223
672 metabasics (Malusà et al., 2018). Following the latter authors, this subduction was “cold” allowing
2224
2225
673 for major amounts of subducted carbonates to survive decarbonation and to be delaminated and stored
2226
2227
674 at depths higher than 180 km, generating a long low velocity layer from Central Southalpine to the
2228
2229
675 Eastern Southalpine domains (Malusà et al., 2018). In fact, according to Maierov et al. (2018) in any
2230
2231
676 collision-subduction process, if the subducted sediments detach from the slab at large depth (> 100
2232
2233
677 km), their exhumation will be hindered by the thick overlying lithosphere and the subducted materials
2234
2235
678 are forced to flow laterally forming a “long sheet” under the upper plate.

2236
2237
679 Malusà et al. (2018) proposed that after the slab carbonates emplacement under the Adria microplate
2238
2239
2240
2241

2242
2243
2244
680 lithosphere, their breakdown occurred, due to the progressive rise of mantle temperatures at the slab
2245
2246
681 interface. The new generated carbonate-rich melts, characterized by low density and viscosity
2247
2248
682 (Frezzotti et al., 2009, Malusà et al., 2018), upwelled and infiltrated the overlying (garnet-bearing)
2249
2250
683 mantle domain. These processes possibly involved the mantle source of the VVP.
2251
2252
684 Several authors (*e.g.*, Aulbach et al., 2004; Su et al., 2010; Meyzen et al., 2016; Sokol et al., 2017)
2253
2254
685 invoked metasomatic processes of silicatic and/or carbonatitic melts and/or fluids to explain the
2255
2256
686 presence of phlogopite in mantle sources. Similarly, we can think that the presence of phlogopite in
2257
2258
687 the VVP mantle source could be responsible for the formation and stabilization of the potassic phase.
2259
2260
688
2261
2262
689 To summarize, the trace element data seem to indicate that VVP magmas were derived by partial
2263
2264
690 melting of metasomatized phlogopite-bearing garnet lherzolite (basanitic magmas) and anhydrous
2265
2266
691 garnet lherzolite (tholeiitic magmas). The metasomatic processes occurred at depth with carbonatitic
2267
2268
692 melts. Except for an ancient carbonatitic signature recorded in Marosticano mantle (Brombin et al.,
2269
2270
693 2018), the Val d'Adige and Lessini Mts. mantle peridotites show no evidence for carbonatitic
2271
2272
694 metasomatism. Therefore, we have not enough elements to constrain the age of the carbonatitic
2273
2274
695 metasomatism recorded in the VVP magmatic products. However, according to Beccaluva et al.
2275
2276
696 (2007), the VVP melts are characterized also by low $^{87}\text{Sr}/^{86}\text{Sr}$ and high $^{144}\text{Nd}/^{143}\text{Nd}$ isotope ratios, as
2277
2278
697 typical of magmas derived from incompatible element depleted mantle sources. Such decoupling of
2279
2280
698 enrichment in trace elements and depletion in isotopic compositions observed for the VVP magmatic
2281
2282
699 products indicates that the carbonatitic metasomatic event must have occurred recently enough to be
2283
2284
700 unable to significantly affect the isotope composition of the VVP magmas. This consideration
2285
2286
701 emphasizes our suggestion that the infiltration of carbonate fluids in the VVP mantle portion could
2287
2288
702 have occurred after the breakdown of carbonates during the subduction of Tethys oceanic slab.
2289
2290
703
2291
2292
704

10.3 The temporal evolution of the magmatic activity of the VVP

2293
2294
2295
2296
2297
2298
2299
2300

2301
2302
2303
705 For basic–ultrabasic rocks older than Quaternary, the dating of mineral separates is preferred over
2304
2305
706 groundmass for which separation of altered from fresh grains is difficult during sample preparation
2306
2307
707 (Jourdan et al., 2007; Verati and Jourdan, 2013). However, due to the lack of relatively abundant and
2308
2309
708 fresh phenocrysts of K-rich minerals in the VVP basanitic and basaltic samples, groundmass dating
2310
2311
709 was carried out. For these samples, slight alteration is suggested by i) the $^{40}\text{Ar}/^{36}\text{Ar}$ intercepts
2312
2313
710 substantially lower than atmospheric values for VVP whole–rock data ($<298.56 \pm 0.31$; [Table 3](#); [Fig.](#)
2314
2315
711 [5a, c, e, g](#)), ii) the absence of proper plateau ages (i.e., $<70\%$ ^{39}Ar released; [Tables 3, 4](#); [Fig. 5d, f, h,](#)
2316
2317
712 [j, x, 6b, c](#)), and iii) convex K/Ca spectra ([Figs. 5b, d, f, h, 6b, d](#)). In view of this, all the obtained mini–
2318
2319
713 plateau ages are considered as minimum crystallization ages. However, the geological significance
2320
2321
714 of these minimum ages is reinforced and confirmed by biostratigraphic data, when available.
2322
2323
715 Therefore, we are confident that the reported whole-rock ages approximately constrain the actual
2324
2325
716 crystallization ages, but we are aware that the true eruption age of a rock that yielded a mini-plateau
2326
2327
717 could lie well outside of the 95% confidence level given by the sample uncertainties. Only
2328
2329
718 Marosticano groundmass data did not define any isochron or plateau ages. However, the age spectra
2330
2331
719 indicating a crystallization age of $\sim 22\text{--}23$ Ma ([Figs. 5w, x, 6c, d](#)) are confirmed by biostratigraphic
2332
2333
720 data supporting a late Oligocene to early Miocene eruption in this district. Ages for the Euganean
2334
2335
721 samples were all obtained on mineral separates and are thus of higher quality. All Euganean samples
2336
2337
722 yielded statistically robust plateau ages based on $> 88\%$ of gas released ([Table 3](#); [Fig. 5l, n, p, r, t, v](#)),
2338
2339
723 only the amphibole separate from EU52 yielded a mini–plateau age (defined by 67% of the released
2340
2341
724 gas; [Table 3](#); [Fig. 5j](#)).

2342
2343
725 Based on the new age determinations and considering the available biostratigraphic data, we
2344
2345
726 reconstructed the temporal evolution of the Cenozoic magmatism occurred in the Southeastern Alpine
2346
2347
727 domain ([Fig. 2](#)). The VVP magmatic activity was discontinuous and took place with several pulses,
2348
2349
728 covering a time–span of about 30 My (from late Paleocene to early Miocene). The oldest activity was
2350
2351
729 always subaqueous, thus difficult to date by the $^{40}\text{Ar}/^{39}\text{Ar}$ technique due to the pervasive alteration of
2352
2353
730 the volcanic products. However, biostratigraphic data constrain the Paleocene onset of VVP
2354
2355
2356
2357
2358
2359

2360
2361
2362
2363 731 magmatism in the Val d'Adige and Lessini Mts., as well as a late Eocene onset in the Euganean Hills
2364
2365 732 (Piccoli et al., 1976, 1981; Savelli and Lipparini, 1979; Luciani, 1989; De Vecchi and Sedeà, 1995;
2366
2367 733 Bassi et al., 2008). The oldest age here obtained with the $^{40}\text{Ar}/^{39}\text{Ar}$ method is Lutetian and is recorded
2368
2369 734 by a basaltic lava flow ($\text{TER1} \geq 45.21 \pm 0.11$ Ma; [Table 3](#); [Figs. 2, 5e, f](#)) from the Lessini Mts. The
2370
2371 735 basanitic neck of the same district records a quite younger age ($\text{BOL1} \geq 38.73 \pm 0.44$ Ma; Bartonian;
2372
2373 736 [Table 3](#); [Figs. 2, 5g, h](#)) consistent with its stratigraphic position, cutting the lava flow from which
2374
2375 737 TER1 was collected. The Val d'Adige district records $^{40}\text{Ar}/^{39}\text{Ar}$ ages similar to those obtained for the
2376
2377 738 Lessini Mts. In particular at Monte Baldo the lava flow (BAL1) and the sill (BAL7) record ages of
2378
2379 739 41.69 ± 0.37 Ma and 41.98 ± 0.20 Ma, respectively while the basanitic neck near Rovereto (BI14)
2380
2381 740 shows an age of 40.73 ± 0.48 Ma ([Tables 3, 4](#); [Figs. 5a–d, 6a, b](#)). These ages are consistent with
2382
2383 741 biostratigraphic ages for the interbedded carbonates ([Fig. 2](#)).
2384
2385
2386 742 All analysed basic to acid Euganean Hills samples yielded indistinguishable ages pointing to a main
2387
2388 743 magmatic phase in this district at $\sim 32.21 \pm 0.09$ Ma (average value). In particular, for the basaltic
2389
2390 744 trachyandesite sample (EU52) both amphibole and plagioclase separates were analysed and the
2391
2392 745 resulting plateau ages are similar (32.35 ± 0.09 Ma and 32.16 ± 0.06 Ma, respectively; [Table 3](#); [Fig.](#)
2393
2394 746 [5j, l](#)). The slight difference between the two ages for this sample may be tentatively attributed to the
2395
2396 747 different closure temperatures of these two minerals, i.e., ~ 550 °C for hornblende and ~ 300 °C
2397
2398 748 plagioclase. This would suggest a relatively slow cooling rate ($\geq 1.3^\circ\text{C}/\text{Ka}$) for the EU52 sub-
2399
2400 749 intrusive body. This relatively slow cooling rate of the magma is easily understandable if we consider
2401
2402 750 that EU52 intruded other basic intrusive units, which were probably nearly synchronous and thus still
2403
2404
2405 751 hot. These host basic units are geochemically equivalent to the tholeiitic basaltic products of the
2406
2407 752 Euganean Hills, while EU52 is representative of the basic alkaline products of this district. The
2408
2409 753 plateau age of EU52 overlaps that of the other dated Euganean basaltic trachyandesite (EU8B = 32.17
2410
2411 754 ± 0.32 Ma; [Table 3](#); [Fig. 5n](#)). The plateau ages for the latitic, trachytic, and rhyolitic Euganean
2412
2413 755 samples range between 32.09 ± 0.29 and 32.34 ± 0.51 Ma ([Table 3](#); [Fig. 5p, r, t, v](#)). Therefore,
2414
2415 756 according to the new geochronological data the peak phase of both basaltic and acidic Euganean
2416
2417
2418

2419
2420
2421 757 magmatism occurred during the Rupelian (lower Oligocene; Fig. 2) in a time-span possibly shorter
2422
2423 758 than 0.3 My.
2424
2425 759 Finally, both the Marosticano samples, collected in Monte Glosio quarry, point to an Aquitanian (early
2426
2427 760 Miocene; ~ 22 Ma) eruption age (Table 3; Figs. 2, 5w, x, 6c, d). According to biostratigraphic studies
2428
2429 761 and field evidences, no eruptions occurred during the Miocene neither in Val d'Adige nor in
2430
2431 762 Euganean Hills. Therefore, the Miocene magmatic products of the eastern Lessini Mts. indicated by
2432
2433 763 biostratigraphic data (Savelli and Lipparini, 1979; Fig. 2) and those of the Marosticano district
2434
2435 764 represent the most recent known magmatic activity in the VVP.
2436
2437 765 The evidence for several VVP magmatic pulses reflects the main extensional phases of the
2438
2439 766 southernmost portion of the Eastern Alps, which were intermitted by episodic accretionary events of
2440
2441 767 the Alpine orogen (Rosenbaum and Lister, 2005). The decompressional melting of the upwelling
2442
2443 768 mantle during extension of continental lithosphere is known as viable mechanism for intraplate
2444
2445 769 magmatism (Pedersen and Ro, 1992). In the Paleocene (65–55 Ma) the Adria–Europe convergence
2446
2447 770 stopped after the continental collision in the Eastern Alps and the following reprise of the convergence
2448
2449 771 was slower than the rollback of the subducting European slab (Stampfli et al., 1998, 2002; Rosenbaum
2450
2451 772 et al., 2002; Dézes et al., 2004; Schmid et al., 2004; Rosenbaum and Lister, 2005). The extension in
2452
2453 773 the overriding plate is promoted when slow convergence rates do not exceed the rates of subduction
2454
2455 774 rollback (Pacanovsky et al., 1999; Jolivet and Faccenna, 2000; Rosenbaum et al., 2002; Heuret and
2456
2457 775 Lallemand, 2005; Rosenbaum and Lister, 2005; Brenna et al., 2015). Therefore, from the Paleocene
2458
2459 776 to the middle Eocene, an extensional regime developed in the Southeastern Alps (Ratschbacher et al.,
2460
2461 777 1989), triggering the magmatism in Val d'Adige (Luciani, 1989; De Vecchi and Sedeà, 1995) and in
2462
2463 778 Lessini Mts. (Borsi et al., 1969; Savelli and Lipparini, 1979; Luciani, 1989; De Vecchi and Sedeà,
2464
2465 779 1995; Bassi et al., 2008) along the transtensional fault systems of the Alpone–Agnò Graben
2466
2467 780 (Zampieri, 1995). From the late Eocene until ~30 Ma an extensional regime developed in the
2468
2469 781 easternmost VVP parts triggering magmatism also in the Euganean Hills (Piccoli et al., 1976, 1981;
2470
2471 782 Zantendeschi et al., 1994; Milani et al., 1999; Bartoli et al., 2014) and Marosticano (Savelli and
2472
2473
2474
2475
2476
2477

2478
2479
2480
2481
2482
2483
2484
2485
2486
2487
2488
2489
2490
2491
2492
2493
2494
2495
2496
2497
2498
2499
2500
2501
2502
2503
2504
2505
2506
2507
2508
2509
2510
2511
2512
2513
2514
2515
2516
2517
2518
2519
2520
2521
2522
2523
2524
2525
2526
2527
2528
2529
2530
2531
2532
2533
2534
2535
2536

Lipparini, 1979). From ~30 Ma to ~23 Ma (Oligocene-Miocene boundary) the extensional processes stopped in the Southeastern Alps (Frisch et al., 2000). The magmatic activity reprised in the early Miocene, but it was quite rare and limited to the easternmost areas. No magmatic activity younger than ~ 20–23 Ma is documented (Savelli and Lipparini, 1979).

10.4 Geodynamic implications of the magmatism in the VVP

According to the new age determinations, the VVP magmatism ranges from 45.21 ± 0.11 Ma (TER1, Lessini Mts. district) to ~ 22 – 23 Ma (LB1 and 25B, Marosticano district). If we consider also the biostratigraphic evidence for early subaqueous activity in Val d’Adige and Lessini Mts., the VVP magmatism probably started from the late Paleocene (Luciani, 1989; De Vecchi and Sedeà, 1995; Bassi et al., 2008). Magmatism in the Central Alps started slightly later, in the Eocene along the Periadriatic/Insubric Line, with the emplacement of the Adamello batholith and its feeder dykes at ~ 42 Ma (Bergomi et al., 2015 and reference therein). However, the climax of the Periadriatic Central Alps orogenic magmatism occurred from 34 Ma to 28 Ma (Bergomi et al., 2015 and reference therein), during the Oligocenic extensional phase that characterized both the Central and the Eastern Alpine domains (Ring, 1994; Nievergelt et al., 1996; Challandes et al., 2003; Glodny et al., 2008; Pleuger et al., 2008; Steck, 2008; Beltrando et al. 2010; Ring and Gerdens, 2016; Schmid et al., 2017). Despite the geographic proximity and despite similar emplacement ages, the Periadriatic Central Alps intrusive bodies and the VVP magmatic products are characterized by quite different geochemical signatures. The first one is characterized by sub-alkaline and calc-alkaline affinities, exhibiting trace element features typical of subduction-related magmas (high LILE/HFSE, high LREE/HFSE ratios, and low-Nb contents; Bellieni, 1980; Bergomi et al., 2015). In particular, the enrichments in LILE, Th and U of the least evolved Periadriatic Central Alps calc-alkaline and sub-alkaline dykes ($MgO > 6$ wt.% and $mg\# > 60$; Fig. 4b), may result from a mantle source contaminated by subducted and recycled continental material, probably the crystalline basement of the Central Southern Alps (Bergomi et al., 2015; Fig. 4b). Contrarily, the VVP magmas span dominant alkaline to rare

2537
2538
2539
809 subalkaline compositions including ultrabasic, basic, intermediate, and acid rocks, with the least
2540
2541
810 evolved magmatic products exhibiting trace element signature typical of intraplate magmas (*e.g.*, high
2542
2543
811 HFSE contents, high LREE/HREE ratios, and relatively low LILE/HFSE ratios). Nb/La ratio when
2544
2545
812 plotted against MgO concentrations, becomes a good proxy to discriminate between arc or intraplate
2546
2547
813 magmatic affinities (Kay et al., 2006b, 2013; Pallares et al., 2016). Low Nb/La can be associated with
2548
2549
814 an arc–magmatism, while high Nb/La reflects intraplate chemical signature. The Periadriatic Central
2550
2551
815 Alps magmatic products show Nb/La values significantly lower than those of VVP magmatic
2552
2553
816 products (0.14–0.45 vs. 0.78–2.08, respectively), confirming a mantle source with an arc affinity for
2554
2555
817 the Periadriatic Central Alps magmatism and a mantle source with an intraplate affinity for the
2556
2557
818 Southeastern Alps (Fig. 9).
2558
2559
819 Despite the clearly different geochemical compositions of the Periadriatic Central Alps and VVP
2560
2561
820 magmatism, both events were explained by the slab break–off model by several authors (*e.g.*, von
2562
2563
821 Blanckenburg and Davies, 1995; Dal Piaz et al., 2003; Macera et al., 2003; Bergomi et al., 2015).
2564
2565
822 According to this model, at ~ 35 Ma, after the Adria–Europe collision in the Western Alps, the
2566
2567
823 subducting oceanic slab detached from the European margin (von Blanckenburg and Davies, 1995;
2568
2569
824 Stampfli et al., 1998, 2002; Dézes et al., 2004). The break–off of the subducting slab allowed
2570
2571
825 asthenospheric upwelling above the supra–subduction hydrated mantle wedge, causing its melting.
2572
2573
826 The occurrence of high seismic velocity anomalies (*i.e.*, “cold” material) observed on tomographic
2574
2575
827 images lying above the mantle transition zone under the Central Alps has been proposed to represent
2576
2577
828 the detached European slab (*e.g.*, Macera et al., 2003; Piromallo and Morelli, 2003; Giacomuzzi et
2578
2579
829 al., 2011; Zhao et al., 2016). According to these tomographic images, such high velocity anomalies
2580
2581
830 are discontinuous, reflecting gaps larger than 100 km (Lippitsch et al., 2003; Piromallo and Morelli,
2582
2583
831 2003). The low–velocity anomalies (*i.e.*, “hot” material) below the VVP could be interpreted as
2584
2585
832 mantle diapirs sucked into these lithospheric gaps and upwelled towards shallower levels inducing
2586
2587
833 partial melting of the surrounding subcontinental lithospheric material and providing an intraplate
2588
2589
834 geochemical signature to the VVP magmatic products (Macera et al., 2003). However, the
2590
2591
2592
2593
2594
2595

2596
2597
2598
835 biostratigraphic ages suggest that the Cenozoic magmatism started in the late Paleocene and also our
2599
2600
836 new radioisotopic ages confirm that the peak activity in the Val d'Adige and Lessini Mts. was Eocene
2601
2602
837 in age (~ 45–38 Ma), i.e., it was formed well before the supposed slab break–off event. Therefore,
2603
2604
838 only the Oligocene magmatic activity from the Euganean Hills may be related to slab detachment.
2605
2606
839 Macera et al. (2003) justified the early VVP eruptions (Paleocene) as the result of the mantle diapir
2607
2608
840 action. On the contrary, Bergomi et al. (2015) proposed a partial melting of supra–subduction mantle
2609
2610
841 wedge in the VVP area in response to the low–angle Alpine subduction that shifted the magmatism
2611
2612
842 into the foreland.
2613
2614
843 Recent high–resolution P wave isotropic tomography (Zhao et al., 2016) and the first P wave
2615
2616
844 anisotropic tomography of the Alps performed (Hua et al., 2017), allow reconstructing the complex
2617
2618
845 mantle structure and dynamics of the Alps and adjacent regions. Isotropic tomography simply
2619
2620
846 provides snapshots of the present crust and upper mantle structures beneath the Alps (Zhao et al.,
2621
2622
847 2016; Hua et al., 2017). On the contrary, seismic anisotropy is produced by the preferred orientation
2623
2624
848 of olivine crystals induced by mantle flow (*e.g.*, Savage, 1999; Savage and Sheehan, 2000; Park and
2625
2626
849 Levin, 2002; Lucente et al., 2006; Savage et al., 2016). Therefore, it reveals information on the actual
2627
2628
850 upper mantle flow field (Long and Silver, 2008; Hua et al., 2017). These new images document a
2629
2630
851 continuous European slab beneath the Central Alps without evidence of any gaps down to 450 km in
2631
2632
852 depth, which rules out the hypothesis of the slab break–off as a viable mechanism for the Cenozoic
2633
2634
853 magmatism in the Alps. In particular, the length of the subducted slab in the Central Alps ranges from
2635
2636
854 450 to 500 km (Hua et al., 2017), which is in accordance with the estimation of the length of a
2637
2638
855 hypothetical continuous subducting slab below the Central Alps and contrasts with the more reduced
2639
2640
856 slab length of 300 km estimated by Piromallo and Faccenna (2004) that was taken as evidence of slab
2641
2642
857 break–off.
2643
2644
858 Furthermore, Freeburn et al. (2017) showed by numerical modelling that magmatism induced by slab
2645
2646
859 break–off occurs only when the latter is shallower than the base of the overriding lithosphere. Such
2647
2648
860 processes are not common as slab break–off occurs typically deeper than the overriding plate
2649
2650
2651
2652
2653
2654

2655
2656
2657
861 thickness (Duretz et al., 2011; van Hunen and Allen, 2011; Freeburn et al., 2017), too deep to generate
2658
2659
862 any decompressional melting of dry upwelling asthenosphere or sufficient thermal perturbations
2660
2661
863 within the overriding lithosphere. These new results allow reconsidering the mechanism generating
2662
2663
864 the magmatic processes in the VVP. In particular, in the frame of our new geochronological results
2664
2665
865 and source modelling, the tomographic results of Zhao et al. (2016) and Hua et al. (2017) provide
2666
2667
866 elements for also an alternative model to explain the Alpine geodynamics. Since the continental
2668
2669
867 collision in the Eastern Alps (65 Ma), the European slab became not only progressively steeper, but
2670
2671
868 also retreated in response to rollback mechanisms (Stampfli et al., 1998, 2002; Rosenbaum et al.,
2672
2673
869 2002; Dézes et al., 2004; Schmid et al., 2004; Rosenbaum and Lister, 2005; Singer et al., 2014;
2674
2675
870 Bergomi et al., 2015; Schlunegger and Kissling, 2015, Kissling and Schlunegger, 2018).

2676
2677
871 Laboratory analogue solutions, 3D experiments, and numerical modelling reproducing the retreating
2678
2679
872 slab movements show that the rollback subduction generates a complex mantle circulation pattern
2680
2681
873 characterized by the presence of poloidal and toroidal mantle flows, escaping from beneath the slab
2682
2683
874 and upwelling from the tip and the lateral edges of the sinking plate, respectively (Fig. 10a; Kincaid
2684
2685
875 and Griffiths, 2003; Funicello et al., 2006; Piromallo et al., 2006; Faccenna et al., 2011, Strak and
2686
2687
876 Schellart, 2014). The poloidal mantle flow can affect areas located far away from the trench, while
2688
2689
877 the toroidal flow produces upwellings located only slightly laterally away from the sub-slab domain
2690
2691
878 (Fig. 10a; Strak and Schellart, 2014). However, the mantle circulation is intermittent: when the slab
2692
2693
879 approaches the upper/lower mantle discontinuity at 660 km, the poloidal circulation reduces
2694
2695
880 significantly, as the slab represents a barrier for material exchange in vertical direction, whereas the
2696
2697
881 toroidal mantle motion is particularly vigorous (Kincaid and Griffiths, 2003; Funicello et al., 2006;
2698
2699
882 Faccenna et al., 2011; Chen et al., 2016). Irrespective of the dominant component (poloidal or
2700
2701
883 toroidal), the subduction-induced mantle flow i) drives deformation, mainly extensional, in the
2702
2703
884 overriding plate (Chen et al., 2016) and ii) triggers volcanism induced by decompressional melting
2704
2705
885 (Faccenna et al., 2011).

2706
2707
886 Taking all of this into account, we speculate that within the Alpine geological setting, the progressive
2708
2709
2710
2711
2712
2713

2714
2715
2716
887 retreat of the European slab caused upwelling of a subduction-induced mantle flow (Fig. 10). This
2717
2718
888 was probably mainly poloidal, as the European slab tip is presently at ~ 450 km (Hua et al., 2017),
2719
2720
889 still far from the 660 km discontinuity. The circulation of this mantle flow could be also the cause of
2721
2722
890 the rising temperature at the slab interface, responsible for the breakdown of the subducted carbonates
2723
2724
891 stored at depth higher than 180 km. Then the carbon-rich melts infiltrated and metasomatized the
2725
2726
892 overlying mantle lithosphere or the mantle wedge. The mantle flow upwelling induced also
2727
2728
893 extensional deformation in the overriding plate and decompressional melting of the phlogopite-
2729
2730
894 bearing and anhydrous (i.e., phlogopite and amphibole-free) garnet lherzolite sources metasomatized
2731
2732
895 by CO₂-rich melts. This process triggered magmatism with intraplate signature instead of arc affinity
2733
2734
896 (Fig. 10). The VVP magmatism occurred in the Paleocene-Eocene in the westernmost side (i.e., Val
2735
2736
897 d'Adige-Lessini Mts. domain) and only since the Oligocene in its eastern areas (i.e., Euganean Hills-
2737
2738
898 Marosticano domain). The southeastward migration and rejuvenation of the magmatism can be
2739
2740
899 accounted for considering that Adria microplate underwent counterclockwise rotation of the order of
2741
2742
900 40–50° since ~ 35 Ma (Lowrie and Alvarez, 1975; Dewey et al., 1989; Rosenbaum et al., 2002; Ring
2743
2744
901 and Gerdens, 2016). Such movement could have controlled the asthenospheric upwelling to affect
2745
2746
902 different portions of the overlying lithosphere.
2747
2748
903 In this work, we ruled out the need of passive upwelling of mantle flow through slab window(s) to
2749
2750
904 explain the occurrence of the VVP magmatism. Although this was not the aim of this work, in the
2751
2752
905 frame of the geodynamic model we also speculate that the Periadriatic orogenic magmatism in Central
2753
2754
906 Alps is related to the dehydration of the subducting oceanic slab, which triggered the partial melting
2755
2756
907 of the overlying spinel-bearing mantle wedge (Fig. 10).
2757
2758
2759
2760
2761
908
2762
2763
2764
2765
2766
2767
2768
2769
2770
2771
2772

2773
2774
2775
2776
2777
2778
2779
2780
2781
2782
2783
2784
2785
2786
2787
2788
2789
2790
2791
2792
2793
2794
2795
2796
2797
2798
2799
2800
2801
2802
2803
2804
2805
2806
2807
2808
2809
2810
2811
2812
2813
2814
2815
2816
2817
2818
2819
2820
2821
2822
2823
2824
2825
2826
2827
2828
2829
2830
2831

Figure 9. MgO (wt.%) vs. Nb/La diagram showing arc (grey field) and intraplate (colored fields) affinities of mantle sources for Val d'Adige, Lessini Mts., Euganean Hills, and Marosticano rocks studied in this work (large symbols) and in previous studies (small symbols delimiting fields). Val d'Adige compositions are from Beccaluva et al., (2007); Lessini Mts. and Marosticano compositions are from Macera et al. (2003) and Beccaluva et al. (2007); Euganean Hills compositions are from Macera et al. (2003) and Milani et al. (1999). **[1 column fitting]**

Figure 10. Schematic model (not in scale) for magmatism in the Central and Southeastern Alpine domains at Eocene/Oligocene. The slab rollback and steepening of the subducted European slab induced the upwelling of a poloidal mantle flow, which causes i) the breakdown of carbonates in calcareous metasediments and carbonated metabasics dragged at depth by the subducting slab (*i.e.* Malusà et al., 2018); ii) extensional deformation within the Adria microplate, and iii) melting of the carbonatitic metasomatized phlogopite-bearing and anhydrous (*i.e.*, phlogopite and amphibole-free) garnet-peridotite sources, which generated the basanitic and the tholeiitic magmas, respectively. In the Central Alps domain, the dehydration of the subducting oceanic slab induced partial melting of the overlying spinel-bearing mantle wedge, which triggered the Periadriatic orogenic magmatism. Inset a) Sketch showing the paths of poloidal and toroidal mantle flows. The poloidal mantle flow escapes from beneath the slab and upwells from its tip, affecting mantle region(s) located far away from the sinking plate; the toroidal flow escapes from the lateral edges of the slab and upwells only in the mantle portion(s) near the slab. **[2 columns fitting]**

11. CONCLUSION

For this work new geochemical and geochronological data are provided to investigate the occurrence of the intraplate magmatism of VVP, which emplaced in an extensional setting (inferred depth Moho: ~ 26 km) at the same time of the Alpine orogeny.

The geothermobarometric and geochemical data of basanitic magmatic products are consistent with ~ 3–4% degree of partial melting of a phlogopite-bearing garnet peridotite mantle source and those of tholeiitic magmatic products are consistent with ~ 5–6% degree of partial melting of an anhydrous (i.e., phlogopite and amphibole-free) garnet peridotite mantle source. All basic–ultrabasic VVP magmatic products exhibit enrichments in Ba, Sr, and P, indicating that the mantle sources could be metasomatized by carbonatitic melts, maybe provided by the breakdown of carbonates in calcareous metasediments and carbonated metabasics dragged at depth by the subducting Tethys slab.

By integrating literature biostratigraphic data with new $^{40}\text{Ar}/^{39}\text{Ar}$ geochronological data of the VVP magmatic products, we reconstructed the temporal evolution of the magmatic activity of this province. In the Paleocene–Eocene the first magmatic activities occurred in the westernmost VVP domain (i.e., Val d’Adige and Lessini Mts.) when an extensional regime was imposed in the Southeastern Alps by the rollback of the subducted oceanic slab. During the Oligocene–Miocene another extensional phase occurred promoting the magmatic activities also in the easternmost VVP domain (i.e., Euganean Hills and Marosticano districts). According to this reconstruction the first VVP eruptions are pre–Oligocene in age, ruling out the hypothesis that the magmatism was due to the upwelling of mantle diapirs through a slab window after the European slab detachment, which occurrence was dated after ~ 35 Ma. Moreover, in accordance with new tomographic images, the present European slab is continuous and nearly vertical, with a tip at ~ 450 km in depth, as expected for a hypothetical continuous subducting slab in the Central Alps. Therefore, in this study a new geodynamic model is proposed:

the progressive retreatment and steepness of the European slab induced the escape of the sub–slab mantle material and its upwelling mainly from the front the slab. The subduction–induced mantle

2891
2892
2893
2894
2895
2896
2897
2898
2899
2900
2901
2902
2903
2904
2905
2906
2907
2908
2909
2910
2911
2912
2913
2914
2915
2916
2917
2918
2919
2920
2921
2922
2923
2924
2925
2926
2927
2928
2929
2930
2931
2932
2933
2934
2935
2936
2937
2938
2939
2940
2941
2942
2943
2944
2945
2946
2947
2948
2949

956 flow caused the increasing temperature at the slab interface and, by consequence, the generation of
957 the metasomatizing CO₂-rich melts after the breakdown of carbonates dragged at depth by the
958 subducting Tethys. The upwelling of the mantle flow also caused the intraplate magmatism in the
959 Alpine collisional setting driving i) extensional deformation in Adria microplate and ii)
960 decompression melting of the carbonatitic metasomatized mantle wedge beneath the VVP. It is also
961 speculated that the migration and rejuvenation of the magmatism southeastward is an effect of the
962 Adria counterclockwise rotation, which started ~ 35 Ma. Finally, we suggest that the coeval
963 Periadriatic orogenic magmatism occurred in the Central Alps is related to the partial melting of the
964 spinel-bearing mantle wedge induced by dehydration of the subducting slab.

966 ACKNOWLEDGMENTS

967 We thank Renzo Tassinari of University of Ferrara and Daria Pasqual of University of Padova for
968 XRF and ICP-MS analyses; Roberto Zorzin for field work and logistical contributions; Adam Frew
969 and Celia Mayers of WAAIF, and Dan Jones of University of Vermont for their assistance during
970 sample preparation and geochronological analyses.

971 Field and laboratory work for this project were supported by the Museo Civico di Storia Naturale di
972 Verona and Regione Veneto.

974 FUNDING

975 V. Brombin was funded by IUSS Mobility Research Programme (VB scholarship for Abroad
976 Mobility for Long Period 04/11/2015) and Young Researcher Grant of the University of Ferrara
977 (Italy) (Pr. No. 101908)

978 C. Bonadiman and A. Marzoli were funded by the Italian Government PRIN 2015-2016 funds (Pr.
979 No. 20158A9CBM).

981 REFERENCES

2950
2951
2952
982 Alagna, K.E., Peccerillo, A., Martin, S., 2010. Tertiary to present evolution of Orogenic magmatism,
2953
2954
983 in Italy. *J. Virt. Expl.* 36: paper 18, in: Beltrando, M., Peccerillo, A., Mattei, M., Conticelli, S.,
2955
2956
984 Doglioni C., (Eds.), *The geology of Italy: tectonics and life along plate margins*, 2010.
2957
2958
985
2959
2960
986 Aldanmaz, E., Köprübaşı, N., Gürer, Ö.F., Kaymakçı, N., Gourgand A., 2006. Geochemical
2961
2962
987 constraints on the Cenozoic, OIB-type alkaline volcanic rocks of NW Turkey: Implications for
2963
2964
988 mantle sources and melting processes. *Lithos* 86, 50–76. <https://doi.org/10.1016/j.lithos.2005.04.003>.
2965
2966
989
2967
2968
990 Allen, M.B., Kheirkhah, M., Neill, I., Emami, M.H., McLeod, C.L., 2013. Generation of arc and
2969
2970
991 within-plate chemical signatures in collision zone magmatism: Quaternary lavas from Kurdistan
2971
2972
992 Province, Iran. *J. Petrol.* 54, 887-911. <https://doi.org/10.1093/petrology/egs090>.
2973
2974
993
2975
2976
994 Ansorge, J., Blundell, D., and Müller, S., 1992. Europe's lithosphere structure, in: Blundell, D.,
2977
2978
995 Freeman, R., Müller, S. (Eds.), *A Continent Revealed: The European Geotraverse*, New York,
2979
2980
996 Cambridge University Press, p. 275.
2981
2982
997
2983
2984
998 Aragón, E., Pinotti, L., D'Eramo, F., Castro, A., Rabbia, O., Coniglio, J., Demartis, M., Hernando,
2985
2986
999 I., Cavarozzi, C.E., Aguilera, Y.E., 2013. The Farallon–Aluk ridge collision with South America:
2987
2988
1000 implications for the geochemical changes of slab window magmas from fore- to back-arc.
2989
2990
1001 *Geoscience Frontiers* 4, 377–388. <https://doi.org/10.1016/j.gsf.2012.12.004>.
2991
2992
1002
2993
2994
1003 Aulbach, S., Griffin, W.L., O'Reilly, S.Y., McCandless, T.E., 2004. Genesis and evolution of the
2995
2996
1004 lithospheric mantle beneath the Buffalo Head Terrane, Alberta (Canada). *Lithos* 77, 413–451.
2997
2998
1005 <https://doi.org/10.1016/j.lithos.2004.04.020>.
2999
3000
1006
3001
3002
1007 Baksi, A.K. 2006. Guidelines for assessing the reliability of $^{40}\text{Ar}/^{39}\text{Ar}$ plateau ages: application to
3003
3004
3005
3006
3007
3008

3009
3010
3011 1008 ages relevant to hotspot tracks. <http://www.mantleplumes.org/ArAr.html>.
3012
3013
3014 1009
3015
3016 1010 Barbieri, G., De Zanche, V., Sedea, R., 1991. Evoluzione del semigraben paleogenico Alpone–Agno
3017
3018 (Monti Lessini). *Rendiconti della Società Geologica Italiana* 14, 5–12.
3019
3020 1012
3021
3022 1013 Barbieri, G., Medizza, F., 1969. Contributo alla conoscenza geologica della regione di Bolca (Monti
3023
3024 1014 Lessini). *Mem. Ist. Geol. Min. Univ. Pad.* 27, 1–36.
3025
3026 1015
3027
3028 1016 Bartoli, O., Meli, S., Bergomi, M.A., Sassi, R., Magaraci, D., Liu, D.Y., 2014. Geochemistry and
3029
3030 1017 zircon U–Pb geochronology of magmatic enclaves in trachytes from the Euganean Hills (NE Italy):
3031
3032 1018 further constraints on Oligocene magmatism in the eastern Southern Alps. *Eur. J. Mineral.* 27, 161–
3033
3034 1019 174. <https://doi.org/10.1127/ejm/2015/0027-2425>.
3035
3036
3037 1020
3038
3039 1021 Bassi, D., Bianchini, G., Mietto, P., Nebelsick, J.H., 2008. Southern Alps: Venetian Pre–Alps, in:
3040
3041 1022 McCann T. (Eds.), *The Geology of Central Europe*, 2. Geol. Soc. London, pp.1087–1092.
3042
3043 1023
3044
3045 1024 Beccaluva, L., Bianchini, G., Bonadiman, C., Coltorti, M., 2007. Intraplate lithospheric and
3046
3047 1025 sublithospheric components in the Adriatic domain: Nephelinite to tholeiite magma generation in the
3048
3049 1026 Paleogene Veneto Volcanic Province, Southern Alps. *Geological Society of America* 418, 131–152.
3050
3051 1027 [https://doi.org/10.1130/2007.2418\(07\)](https://doi.org/10.1130/2007.2418(07)).
3052
3053
3054 1028
3055
3056 1029 Beccaluva, L., Bonadiman, C., Coltorti, M., Salvini, L., Siena, F., 2001. Depletion events, nature of
3057
3058 1030 metasomatizing agent and timing of enrichment processes in lithospheric mantle xenoliths from the
3059
3060 1031 VVP. *J. Petrol.* 42, 173–187. <https://doi.org/10.1093/petrology/42.1.173.0>.
3061
3062 1032
3063
3064
3065
3066
3067

3068
3069
3070
1033 Begemann, F., Ludwig, K.R., Lugmair, G.W., Min, K., Nyquist, L.E., Patchett, P.J., Renne, P.R.,
3071
3072
1034 Shih, C.Y., Villa, I.M., Walker, R.J., 2001. Call for an improved set of decay constants for
3073
3074
1035 geochronological use. *Geochim. Cosmochim. Acta* 65, 111–121. [https://doi.org/10.1016-S0016-](https://doi.org/10.1016/S0016-)
3075
3076
1036 7037(00)00512-3.
3077
3078
1037
3079
3080
1038 Bellieni, G., 1980. The Cima di Villa (Zinsnock) massif: geochemical features and comparisons with
3081
3082
1039 the Vedrette di Ries (Rieserferner) pluton (Eastern Alps, Italy). *Neu. Jb. Mineral., Abh.* 138, 244–
3083
3084
1040 258.
3085
3086
1041
3087
3088
1042 Beltrando, M., Lister, G.S., Rosenbaum, G., Richards, S., Forster, M.A., 2010. Recognizing episodic
3089
3090
1043 lithospheric thinning along a convergent plate margin: the example of the Early Oligocene Alps. *Earth*
3091
3092
1044 *Sci. Rev.* 103, 81–98. <https://doi.org/10.1016/j.earscirev.2010.09.001>.
3093
3094
1045
3095
1046 Bergomi, M.A., Zanchetta, S., Tunesi, A., 2015. The Tertiary dike magmatism in the Southern Alps:
3096
3097
1047 geochronological data and geodynamic significance. *Int. J. Earth Sci.* 104, 449–473.
3098
3099
1048 <https://doi.org/10.1007/s00531-014-1087-5>.
3100
3101
1049
3102
3103
1050 Bogaard, P.J.F., Wörner, G., 2003. Petrogenesis of basanitic to tholeiitic volcanic rocks from the
3104
3105
1051 Miocene Vogelsberg, Central Germany. *J. Petrol.* 44, 569–602.
3106
3107
1052 <https://doi.org/10.1093/petrology/44.3.569>.
3108
3109
1053
3110
3111
1054 Borsi, S., Ferrara, G., Piccoli, G., 1969. Determinazioni col metodo K/Ar dell'età delle eruzioni
3112
3113
1055 euganee. *Rendiconti della Società Italiana di Mineralogia e Petrologia* 25, 27–34.
3114
3115
1056
3116
3117
1057 Brack, P., 1981. Structures in the southwestern border of the Adamello intrusion. *Swiss Bull. Mineral.*
3118
3119
1058 *Petrol.* 61, 37–50. <https://doi.org/10.5169/seals-47129>.
3120
3121
3122
3123
3124
3125
3126

3127
3128
3129
1059
3130
3131
1060 Brack, P., 1984. Geologie der Intrusiva und Nebengesteine des Südwest-Adamello (Nord-Italien).
3132
3133
1061 Ph.D. thesis, Dissertation ETH. Nr. 7612.
3134
3135
1062
3136
3137
1063 Bradley, D.C., Kusky, T., Heaussler, P.J., Goldfarb, R.J., Miller, M.L., Dumuolin, J.A., Nelson, S.W.,
3138
3139
1064 Karl, S.M., 2003. Geological signature of early Tertiary ridge subduction in Alaska. Geol. Soc. Am.
3140
3141
1065 Spec. 371, 19–49. <https://doi.org/10.1130/0-8137-2371-X.19>.
3142
3143
1066
3144
3145
1067 Brenna, M., Cronin, S.J., Kereszturi, G., Sohn, Y.K., Smith, I.E.M., Wijbrans, J., 2015. Intraplate
3146
3147
1068 volcanism influenced by distal subduction tectonics at Jeju Island, Republic of Korea. Bull. Volcanol.
3148
3149
1069 77, 1–16. <https://doi.org/10.1007/s00445-014-0896-5>.
3150
3151
3152
1070
3153
3154
1071 Briggs, R.M., McDonough, W.F., 1990. Contemporaneous convergent margin and intraplate
3155
1072 magmatism, North island, New Zealand. J. Petrol. 31, 813–851.
3156
3157
1073 <https://doi.org/10.1093/petrology/31.4.813>.
3158
3159
1074
3160
3161
3162
1075 Brombin, V., Bonadiman, C., Coltorti, M., Fahnestock, M.F., Bryce, J.G., Marzoli, A., 2018.
3163
3164
1076 Refertilized mantle keel below the Southern Alps domain (North-East Italy): Evidence from
3165
3166
1077 Marosticano refractory mantle peridotites. Lithos 300–301, 72–85.
3167
3168
1078 <https://doi.org/10.1016/j.lithos.2017.11.032>.
3169
3170
1079
3171
3172
3173
1080
3174
3175
1081 Callegari, E., Brack, P., 2002. Geological map of the Tertiary Adamello batholith (Northern Italy).
3176
3177
1082 Explanatory notes and legend. Memorie Scienze Geologiche 54, 19–49.
3178
3179
1083
3180
3181
1084 Carminati, E., Doglioni, C., 2012. Alps vs. Apennines: the paradigm of a tectonically asymmetric
3182
3183
3184
3185

3186
3187
3188
1085 Earth. Earth Sci. Rev. 112, 67–96. <https://doi.org/10.1016/j.earscirev.2012.02.004>.
3189
3190
1086
3191
3192
1087 Challandes, N., Marquer, D., Villa, I.M., 2003. Dating the evolution of C–S microstructures: A
3193
3194 combined $^{40}\text{Ar}/^{39}\text{Ar}$ step–heating and UV laserprobe analysis of the Alpine Roffna shear zone. Chem.
1088 Geol., 197, 3–19. [https://doi.org/10.1016/S0009-2541\(02\)00354-6](https://doi.org/10.1016/S0009-2541(02)00354-6).
3196
1089
3198
1090
3200
1091 Chen, Z., Schellart, W.P., Strak, V., Duarte, J.C., 2016. Does subduction–induced mantle flow drive
3202
3203 back–arc subduction? Earth Planet. Sci. Lett. 441, 200–210.
1092
3204
3205
1093 <https://doi.org/10.1016/j.epsl.2016.02.027>.
3206
3207
1094
3208
3209
1095 Conceição, R.V., Green, D.H., 2004. Derivation of potassic (shoshonitic) magmas by decompression
3210
3211 melting of phlogopite + pargasite lherzolite. Lithos 72, 209–229.
1096
3212
3213
1097 <https://doi.org/10.1016/j.lithos.2003.09.003>.
3215
1098
3217
1099 Conticelli, S., Guarnieri, L., Farinelli, A., Mattei, M., Avanzinelli, R., Bianchini, G., Boari, E.,
3219
3220 Tommasini, S., Tiepolo, M., Prelevic, D., Venturelli, G., 2009. Trace–elements and Sr–Nd–Pb
1100
3221
3222 isotopes of K–rich, shoshonitic, and calc–alkaline magmatism of the Western Mediterranean region:
1101
3223
3224
1102 genesis of ultrapotassic to calcalkaline magmatic association in a post–collisional geodynamic
3225
3226
1103 setting. Lithos 107, 69–92. <https://doi.org/10.1016/j.lithos.2008.07.016>.
3227
3228
1104
3229
3230
1105 Cook, C., Briggs, R.M., Smith, I.E.M., Maas, R., 2005. Petrology and geochemistry of intraplate
3231
3232 basalts in the South Auckland Volcanic Filed, New Zealand: evidence for two coeval magma suites
1106
3233
3234
1107 from distinct sources. J. Petrol. 46, 473–503. <https://doi.org/10.1093/petrology/egh084>.
3235
3236
1108
3237
3238
1109 Dal Piaz, G.V., Bistacchi, A., Massironi, M., 2003. Geological outline of the Alps. Episodes 26, 175–
3239
3240
3241
1110 181.
3242
3243
3244

3245
3246
3247
1111
3248
3249
1112 de Boer, J.Z., Defant, M.J., Stewart, R.H., Restrepo, J.P., Clark, L.F., Ramirez, A.H., 1988.
3250
3251
1113 Quaternary calc-alkaline volcanism in western panama: regional variation and implication for the
3252
3253
1114 plate tectonic framework. *Journal of South American Earth Sciences* 1, 275–293.
3254
3255
1115 [https://doi.org/10.1016/0895-9811\(88\)90006-5](https://doi.org/10.1016/0895-9811(88)90006-5).
3256
3257
1116
3258
3259
1117 De Vecchi, G., Gregnanin, A., Piccirillo, E.M., 1976. Aspetti petrogenetici del vulcanesimo terziario
3260
3261
1118 Veneto. *Mem. Ist. Geol. Min. Univ. Pad.* 30, 1–63.
3262
3263
1119
3264
3265
1120 De Vecchi, G., Sedeà, R., 1995. The Paleogene basalts of the Veneto region (NE Italy). *Memorie di*
3266
3267
1121 *Scienze Geologiche* 47, 253–374.
3268
3269
3270
1122
3271
3272
1123 Dewey, J.F., Helman, M.L., Turco, E., Hutton, D.H.W., Knott, S.D., 1989. Kinematics of the western
3273
3274
1124 Mediterranean, in *Alpine Tectonics*. *Geol. Soc. Spec. Publ. London* 45, 265–283.
3275
3276
1125 <https://doi.org/10.1144/GSL.SP.1989.045.01.15>.
3277
3278
1126
3279
3280
1127 Dézes, P., Schmid, S.M., Ziegler, P.A., 2004. Evolution of the European Cenozoic Rift System:
3281
3282
1128 interaction of the Alpine and Pyrenean orogenes with their foreland lithosphere. *Tectonophysics* 389,
3283
3284
1129 1–33. <https://doi.org/10.1016/j.tecto.2004.06.011>.
3285
3286
3287
1130
3288
3289
1131 Dixon, J., Clague, D.A., Cousens, B., Monsalve, M.L., Uhl, J., 2008. Carbonatite and silicate melt
3290
3291
1132 metasomatism of the mantle surrounding the Hawaiian plume: evidence from volatiles, trace
3292
3293
1133 elements, and radiogenic isotopes in rejuvenated-stage lavas from Niihau, Hawaii. *Geochem.*
3294
3295
1134 *Geophys.* 9. <https://doi.org/10.1029/2008GC002076>.
3296
3297
1135
3298
3299
1136 Duret, T., Gerya, T.V., May, D.A., 2011. Numerical modelling of spontaneous slab breakoff and
3300
3301
3302
3303

3304
3305
3306
1137 subsequent topographic response. *Tectonophysics* 502, 244–256.
3307
3308
1138 <https://doi.org/10.1016/j.tecto.2010.05.024>.
3309
3310
1139
3311
3312
1140 Faccenna, C., Molin, P., Orecchio, B., Olivetti, V., Bellier, O., Funicello, F., Minelli, L., Piromallo,
3313 C., Billi, A., 2011. Topography of the Calabria subduction zone (southern Italy): clues for the origin
3314
1141 of Mt. Etna. *Tectonics* 30, TC1003. <https://doi.org/10.1029/2010TC002694>
3315
1142
3316
1143
3317
1144 Faccini, B., Coltorti, M., Bonadiman, C., 2018. Contemporaneous emission of calcalkaline and
3318
1145 alkaline magmas in subductive geodynamic settings: a mantle xenolith perspective. Book of
3319
1146 Abstracts, 3rd European Mantle Workshop – Pavia, 43.
3320
3321
1147
3322
1148 Ferrari, L., 2004. Slab detachment control on mafic volcanic pulse and mantle heterogeneity in central
3323
1149 Mexico. *Geology* 32, 77–80. <https://doi.org/10.1130/G19887.1>.
3324
1150
3325
1151 Ferrari, L., Petrone, C.M., Francalanci, L., 2001. Generation of oceanic–island basalt–type volcanism
3326
1152 in the western Trans–Mexican volcanic belt by slab rollback, asthenosphere infiltration, and variable
3327
1153 flux melting. *Geology* 29, 507–510. [https://doi.org/10.1130/0091-7613\(2001\)029<0507:
3328
1154 GOOIBT>2.0.CO;2](https://doi.org/10.1130/0091-7613(2001)029<0507:GOOIBT>2.0.CO;2).
3329
1155
3330
1156 Frascari Ritondale Spano, F., 1969. Serie Paleogeniche nell’area pedemontana a Sud dell’Altopiano
3331
1157 di Asiago (Vicenza, Italia) *Mémoires du Bureau des Recherches géologiques et Minières* 69, 173–
3332
1158 182.
3333
1159
3334
1160 Frascari Ritondale Spano, F., Bassani, P., 1973. Ricerche geologiche nei dintorni di Bassano del
3335
1161 Grappa (Vicenza). *Memorie Museo Trid. Scienze Naturali* 19, 65–112.
3336
1162
3337
3338
3339
3340
3341
3342
3343
3344
3345
3346
3347
3348
3349
3350
3351
3352
3353
3354
3355
3356
3357
3358
3359
3360
3361
3362

3363
3364
3365
1163 Freeburn, R., Bouilhol, P., Maunder, B., Magni, V., van Hunen, J., 2017. Numerical models of the
3366
3367
1164 magmatic processes induced by slab breakoff. *Earth Planet. Sci. Lett.* 478, 203–213.
3368
3369
1165 <https://doi.org/10.1016/j.epsl.2017.09.008>.
3370
3371
1166
3372
3373
1167 Frezzotti, M.L., Peccerillo, A., Panza G., 2009. Carbonate metasomatism and CO₂ lithosphere–
3374
3375
1168 asthenosphere degassing beneath the Western Mediterranean: an integrated model arising from
3376
3377
1169 petrological and geophysical data. *Chem. Geol.* 262, 108–120.
3378
3379
1170 <https://doi.org/10.1016/j.chemgeo.2009.02.015>.
3380
3381
1171
3382
3383
1172 Frisch, W., Dunkl, I., Kuhlemann, J., 2000. Post–collisional orogen–parallel large–scale extension in
3384
3385
1173 the Eastern Alps. *Tectonophysics* 327, 239–265. [https://doi.org/10.1016/S0040-1951\(00\)00204-3](https://doi.org/10.1016/S0040-1951(00)00204-3).
3386
3387
1174
3388
3389
1175 Frost, D.J., 2006. The stability of hydrous mantle phases. *Rev. Mineral. Geochem.* 62, 243–271.
3390
3391
1176 <https://doi.org/10.2138/rmg.2006.62.11>.
3392
3393
1177
3394
3395
1178 Frost, D.J., 2008. The upper mantle and transition zone. *Elements* 4, 171–176.
3396
3397
1179 <https://doi.org/10.2113/GSELEMENTS.4.3.171>.
3398
3399
1180
3400
3401
1181 Funiciello, F., Moroni, M., Piromallo, C., Faccenna, C., Cenedese, C., Bui, H.A., 2006. Mapping
3402
3403
1182 mantle flow during retreating subduction: Laboratory models analysed by feature tracking. *J.*
3404
3405
1183 *Geophys. Res.* 111, B03402. <https://doi.org/10.1029/2005JB003792>.
3406
3407
1184
3408
3409
1185 Furman, T., Graham, D., 1999. Erosion of lithospheric mantle beneath the East African Rift system:
3410
3411
1186 geochemical evidence from the Kivu volcanic province. *Lithos* 48, 237–262.
3412
3413
1187 [https://doi.org/10.1016/S0024-4937\(99\)00031-6](https://doi.org/10.1016/S0024-4937(99)00031-6).
3414
3415
1188
3416
3417
3418
3419
3420
3421

3422
3423
3424
1189 Fytikas, M., Innocenti, F., Manetti, P., Peccerillo, A., Mazzuoli, R., Villari, L., 1984. Tertiary to
3425
3426
1190 Quaternary evolution of volcanism in the Aegean region. *Geol. Soc. Spec. Publ. London* 17, 687–
3427
3428
1191 699. <https://doi.org/10.1144/GSL.SP.1984.017.01.55>.
3429
3430
1192
3431
3432
1193 Gasperini, D., Bosch, D., Braga, R., Bondi, M., Macera, P., Morten, L., 2006. Ultramafic xenoliths
3433
3434 from the Veneto Volcanic Province (Italy): Petrological and geochemical evidence for multiple
3435
1194 metasomatism of the SE Alps mantle lithosphere. *Geochem. J.* 40, 377–404.
3436
3437
1195 <https://doi.org/10.2343/geochemj.40.377>.
3438
3439
1196
3440
3441
1197
3442
3443
1198 Gatta, G.D, McIntyre, G.J., Sassi, R., Rotiroti, N., Pavese, A., 2011. Hydrogen-bond and cation
3444
3445
1199 partitioning in muscovite: A single-crystal neutron-diffraction study at 295 and 20 K. *Am. Mineral.*
3446
3447
1200 96, 34–41. <https://doi.org/10.2138/am.2011.3595>.
3448
3449
1201
3450
3451
1202 Gavioli, G., 1972. Ricerche stratigrafiche e tettoniche nei dintorni di Malo (Vicenza). Tesi di laurea,
3452
3453 Istituto di Geologia Università di Bologna.
3454
1203
3455
1204
3456
3457
1205 Gemmi, M., Merlini, M., Pavese, A., Curetti, N., 2008. Thermal expansion and dehydroxylation of
3458
3459
1206 phengite micas. *Phys. Chem. Minerals* 35, 367–379. <https://doi.org/10.1007/s00269-008-0230-x>.
3460
3461
3462
1207
3463
3464
1208 Giacomuzzi, G., Chiarabbia, C., De Gori, P., 2011. Linking the Alps and Apennines subduction
3465
3466
1209 systems: New constraints revealed by high-resolution teleseismic tomography. *Earth Planet. Sci.*
3467
3468
1210 *Lett.* 301, 531–543. <https://doi.org/10.1016/j.epsl.2010.11.033>.
3469
3470
1211
3471
3472
1212 Giese, P., Bunn, H., 1992, Moho depth, atlas map 2, in Blundell, D., Freeman, R., and Müller, S.
3473
3474
1213 (Eds.), *A Continent Revealed: The European Geotraverse*: New York, Cambridge University Press,
3475
3476
1214 p. 275, scale 1:2,500,000.
3477
3478
3479
3480

3481
3482
3483
1215
3484
3485
1216 Giusberti, L., Del Favero, L., Roghi, G., 2014. The Purga di Bolca–Vegroni sites, in: Papazzoni C.A.,
3486
3487
1217 Giusberti, L., Carnevale, G., Roghi, G., Bassi, D., Zorzin R. (Eds.), The Bolca Fossil–Lagerstätten:
3488
3489
1218 A window into the Eocene World. *Rendiconti della Società Paleontologica Italiana* 4, pp. 95–103.
3490
3491
1219
3492
3493
1220 Glodny, J., Ring, U., Kühn, A., 2008. High–pressure metamorphism, thrusting, strike–slip and
3494
3495
1221 extensional shearing in the Tauern Window, Eastern Alps: All starting at the same time? *Tectonics*,
3496
3497
1222 27, TC4004. <https://doi.org/10.1029/2007TC002193>.
3498
3499
3500
1223
3501
3502
1224 Grad, M., Tiira, T., ESC Working Group, 2009. The Moho depth map of the European Plate.
3503
3504
1225 *Geophys. J. Int.* 176, 279–292. <https://doi.org/10.1111/j.1365-246X.2008.03919.x>.
3506
3507
1226
3508
1227 Green, D.H., Blundy, J.D., Adam, J., Yaxley, G.M., 2000. SIMS determination of trace element
3509
3510
1228 partition coefficients between garnet, clinopyroxene and hydrous basaltic liquids at 2–7.5 GPa and
3511
3512
1229 1020–1200°C. *Lithos* 53, 165–187. [https://doi.org/10.1016/S0024-4937\(00\)00023-2](https://doi.org/10.1016/S0024-4937(00)00023-2).
3514
3515
1230
3516
3517
1231 Green, D.H., Ringwood, A.E., 1970. Mineralogy of peridotitic compositions under upper mantle
3518
3519
1232 conditions. *Phys. Earth Planet. Inter.* 3, 359–371. [https://doi.org/10.1016/0031-9201\(70\)90076-2](https://doi.org/10.1016/0031-9201(70)90076-2).
3520
3521
1233
3522
3523
1234 Greenough J. D., Hayatsu A., Papezik V. S., 1988. Mineralogy, petrology and geochemistry of the
3524
3525
1235 alkaline Malpeque Bay sill, Prince Edward Island. *Canad. Mineral.* 26, 97–108.
3526
3527
1236
3528
3529
1237 Harangi, S., Downes, H., Seghedi, I., 2006. Tertiary–Quaternary subduction processes and related
3530
3531
1238 magmatism in the Alpine–Mediterranean region. *Geol. Soc. London, Memoirs* 32, 167–190.
3532
3533
1239 <https://doi.org/10.1144/GSL.MEM.2006.032.01.10>.
3534
3535
3536
1240
3537
3538
3539

3540
3541
3542
1241 Hellebrand, E., Snow, J.E., Hoppe, P., Hofmann, A.W., 2002. Garnet–field melting and late–stage
3543
3544
1242 refertilization in “residual” abyssal peridotites from the Central Indian Ridge. *J. Petrol.* 43, 2305–
3545
3546
1243 2338. <https://doi.org/10.1093/petrology/43.12.2305>.
3547
3548
1244
3549
3550
1245 Heuret, A., Lallemand, S., 2005. Plate motions, slab dynamics and back–arc deformation. *Phys. Earth*
3551
3552
1246 *Planet. Inter.* 149, 31–51. <https://doi.org/10.1016/j.pepi.2004.08.022>.
3553
3554
1247
3555
3556
1248 Hua, Y., Zhao, D., Xu, Y., 2017. P wave anisotropic tomography of the Alps. *J. Geophys. Res.: Solid*
3557
3558
1249 *Earth* 122, 4509–4528. <https://doi.org/10.1002/2016JB013831>.
3559
3560
1250
3561
3562
1251 Ionov, D. A., O’Reilly, S. Y., Kopylova, M. G., Genshaft, Y. S., 1996. Carbonate–bearing mantle
3563
3564
1252 peridotite xenoliths from Spitsbergen: phase relationships, mineral compositions and trace element
3565
3566
1253 residence. *Contrib. Mineral. Petrol.* 125, 375–392. <https://doi.org/10.1007/s004100050229>.
3567
3568
1254
3569
3570
1255 Irvine, T.N., Baragar, W.R.A., 1971. A guide to the chemical classification of the common volcanic
3571
3572
1256 rocks. *Can. J. Earth. Sci.* 8, 523–548. <https://doi.org/10.1139/e71-055>.
3573
3574
1257
3575
3576
1258 Jolivet, L., Faccenna, C., 2000. Mediterranean extension and the Africa– Eurasia collision. *Tectonics*
3577
3578
1259 19, 1095–1106. <https://doi.org/10.1029/2000TC900018>.
3580
3581
1260
3582
3583
1261 Jourdan, F., Féraud, G., Bertrand, H., Watkeys, M.K., 2007. From flood basalts to the onset of
3584
3585
1262 oceanization: Example from the $^{40}\text{Ar}/^{39}\text{Ar}$ high–resolution picture of the Karoo large igneous
3586
3587
1263 province. *Geochem. Geophys.* 8, Q02002. <https://doi.org/10.1029/2006GC001392>.
3588
3589
1264
3590
3591
3592
3593
3594
3595
3596
3597
3598

3599
3600
3601
1265 Kagami, H., Ulmer, P., Hansmann, W., Dietrich, V., Steiger, R.H., 1991. Nd–Sr isotopic and
3602
3603
1266 geochemical characteristics of the southern Adamello (Northern Italy) intrusives: implications for
3604
3605
1267 crustal versus mantle origin. *J. Geophys. Res.* 96, 14331–14346. <https://doi.org/10.1029/91JB01197>.
3606
3607
1268
3608
3609
1269 Kay, S.M., Ardolino, A.A., Gorrington, M., Ramos, V., 2007. The Somuncura Large igneous province
3610
3611
1270 in Patagônia: interaction of a transient mantle thermal anomaly with a subducting slab. *J. Petrol.* 48,
3612
3613
1271 43–77. <https://doi.org/10.1093/petrology/egl053>.
3614
3615
1272
3616
3617
1273 Kay, S.M., Jones, H.A., Kay, R.W., 2013. Origin of Tertiary to Recent EM – and subduction – like
3618
3619
1274 chemical and isotopic signatures in Auca Mahuida region (37°–38°S) and other Patagonian plateau
3620
3621
1275 lavas. *Contrib. Mineral. Petrol.* 166, 165–192. <http://dx.doi.org/10.1007/s00410-013-0870-9>.
3622
3623
3624
1276
3625
3626
1277 Kay, S.M., Mancilla, O., Copeland, P., 2006b. Evolution of the backarc Chachahuén volcanic
3627
3628
1278 complex at 37°S latitude over a transient Miocene shallow subduction zone under the Neuquén Basin.
3629
3630
1279 Geological Society of America, Special Paper 407, 215–246. [https://doi.org/10.1130/2006.2407\(10\)](https://doi.org/10.1130/2006.2407(10)).
3631
3632
1280
3633
3634
1281 Kincaid, C., Griffiths, R.W., 2003. Laboratory models of the thermal evolution of the mantle during
3635
3636
1282 rollback subduction. *Nature* 425, 58–62. <https://doi.org/10.1038/nature01923>.
3637
3638
3639
1283
3640
3641
1284 Kissling, E., Schlunegger, F., 2018. Rollback orogeny model for the evolution of the Swiss Alps.
3642
3643
1285 *Tectonics* 37, 1097–1115. <https://doi.org/10.1002/2017TC004762>.
3644
3645
1286
3646
3647
1287 Konzett, J., Sweeney, R.J., Thompson, A.B., Ulmer, P., 1997. Potassium amphibole stability in the
3648
3649
1288 upper mantle: an experimental study in a peralkaline KNCMASH system to 8.5 GPa. *J. Petrol.* 38,
3650
3651
1289 537–568. <https://doi.org/10.1093/etroj/38.5.537>.
3652
3653
1290
3654
3655
3656
3657

3658
3659
3660
1291 Konzett, J., Ulmer, P., 1999. The stability of hydrous potassic phases in lherzolitic mantle. An
3661
3662
1292 experimental study to 9.5 GPa in simplified and natural bulk compositions. *J. Petrol.* 40, 629–652.
3663
3664
1293 <https://doi.org/10.1093/petroj/40.4.629>.
3665
3666
1294
3667
3668
1295 LaTourette, T., Hervig, R.L., Holloway, J.R., 1995. Trace element partitioning between amphibole,
3669
3670
1296 phlogopite, and basanite melt. *Earth Planet. Sci. Lett.* 135, 13–30. <https://doi.org/10.1016/0012->
3671
3672
1297 [821X\(95\)00146-4](https://doi.org/10.1016/0012-821X(95)00146-4).
3673
3674
1298
3675
3676
1299 Le Maitre, R.W., Streckeisen, A., Zanettin, B., Le Bas, M.J., Bonin, B., Bateman, P. Bellieni, G.,
3677
3678
1300 Dudek, A., Efremova, S., Keller, J., Lamere, J., Sabine, P.A., Schmid, R., Sorensen, H., Woolley,
3679
3680
1301 A.R. 2002. *Igneous Rocks: A Classification and Glossary of Terms, Recommendations of the*
3681
3682
1302 *International Union of Geological Sciences Subcommittee of the Systematics of Igneous Rocks*, ed.
3683
3684
1303 Cambridge University Press, UK.
3685
3686
1304
3687
3688
1305 Lee, J.Y., Marti, K., Severinghaus, J.P., Kawamura, K., Yoo, H.-S., Lee, J.B., Kim, J.S., 2006. A
3689
3690
1306 redetermination of the isotopic abundance of atmospheric Ar. *Geochim. Cosmochim. Acta* 70, 4507–
3691
3692
1307 4512. <https://doi.org/10.1016/j.gca.2006.06.1563>.
3693
3694
3695
1308
3696
3697
1309 Lippitsch, R., Kissling, E., Ansorge, J., 2003. Upper mantle structure beneath the Alpine orogen
3698
3699
1310 from high-resolution teleseismic tomography. *J. Geophys. Res.* 108(B8), 2376.
3700
3701
1311 <https://doi.org/10.1029/2002JB002016>.
3702
3703
3704
1312
3705
3706
1313 Long, M.D., Silver, P.G. 2008. The subduction zone flow field from seismic anisotropy: A global
3707
3708
1314 view. *Science* 319, 315–318. <https://doi.org/10.1126/science.1150809>.
3709
3710
3711
1315
3712
3713
3714
3715
3716

3717
3718
3719
1316 Lowrie, W., Alvarez, W., 1975. Paleomagnetic evidence for rotation of the Italian Peninsula. *J.*
3720
3721
1317 *Geophys. Res.* 80, 1579–1592. <https://doi.org/10.1029/JB080i011p01579>.
3722
3723
1318
3724
3725
1319 Lucente, F.P., Margheriti, L., Piromallo, C., Barruol, G., 2006. Seismic anisotropy reveals the long
3726
3727 route of the slab through the western–central Mediterranean mantle. *Earth Planet. Sci. Lett.* 241, 517–
1320 529. <https://doi.org/10.1016/j.epsl.2005.10.041>.
3728
3729
1321
3730
3731
1322
3732
3733
1323 Luciani, V., 1989. Stratigrafia sequenziale del Terziario nella Catena del Monte Baldo (Province di
3734
3735 Verona e Trento). *Memorie di Scienze Geologiche* 41, 263–351.
3736
1324
3737
3738
1325
3739
3740
1326 Macera, P., Gasperini, D., Piromallo, C., Blichert–Toft, J., Bosch, D., Del Moro, A., Martin, S., 2003.
3741
3742 Geodynamic implications of deep mantle upwelling in the source of Tertiary volcanics from the
1327 Veneto region (Southern–Eastern Alps). *J. Geodyn.* 36, 563–590.
3743
3744
1328
3745
3746
1329
3747
3748
1330
3749
3750
1331 Macera, P., Gasperini, D., Ranalli, G., Mahatsente, R., 2008. Slab detachment and mantle plume
3751
3752 upwelling in subduction zones: an example from the Italian South–Eastern Alps. *J. Geodyn.* 45, 32–
1332 48. <https://doi.org/10.1016/j.jog.2007.03.004>.
3753
3754
1333
3755
3756
1334
3757
3758
3759
1335 Maierov, P., Schulmann, K., Gerya, T., 2018. Relamination styles in collisional orogenes. *Tectonics*
3760
3761 37, 224–250. <https://doi.org/10.1002/2017TC004677>.
1336
3762
3763
1337
3764
3765
1338 Malusà, G.M., Frezzotti, M.L., Ferrando, S., Brandmayr, E., Romanelli, F., Panza, G.F., 2018. Active
3766
3767 carbon sequestration in the Alpine mantle wedge and implications for long–term climate trends. *Sci.*
1339
3768
3769
1340 *Rep.* 8, 1–8. <https://doi.org/10.1038/s41598-018-22877-7>.
3770
3771
1341
3772
3773
3774
3775

3776
3777
3778
1342 Mandler, B.E., Grove, T.L., 2016. Controls on the stability and composition of amphibole in the
3779 Earth's mantle. *Contrib. Mineral. Petrol.*, 171 (8–9). <https://doi.org/10.1007/s00410-016-1281-5>.
3780
1343
3781
3782
1344
3783
3784
1345 Manzotti, P., Ballèvre, M., Zucali, M., Robyr, M., Engi, M., 2014. The tectonometamorphic evolution
3785 of the Sesia–Dent Blanche nappes (internal Western Alps): review and synthesis. *Swiss J. Geosci.*
3786 107, 309–336. <https://doi.org/10.1007/s00015-014-0172-x>.
3787
1346
3788
3789
1347
3790
3791
1348
3792
3793
1349 McDonough, W.F., Rudnick, R.L, 1998. Mineralogy and composition of the upper mantle. *Rev.*
3794 *Mineral. Geochem.* 37, 139-164.
3795
1350
3796
3797
1351
3798
3799
1352 McDonough, W.F., Sun, S.S, 1995. The composition of the Earth. *Chem. Geol.* 120, 223–253.
3800
1353 [https://doi.org/10.1016/0009-2541\(94\)00140-4](https://doi.org/10.1016/0009-2541(94)00140-4).
3801
3802
3803
1354
3804
3805
1355 McDougall, I., Harrison, TM. 1999. *Geochronology and Thermochronology by the ⁴⁰Ar/³⁹Ar method.*
3806 Oxford University Press, New York.
3807
1356
3808
3809
1357
3810
3811
1358 Medizza, F., 1980. Il giacimento della Purga di Bolca (Verona), in: *I vertebrati fossili italiani.*
3812 Catalogo della Mostra, Verona, pp. 147–148.
3813
1359
3814
3815
1360
3816
3817
1361 Merle, R., Marzoli, A., Aka, F.T., Chiaradia, J.M., Reisberg, L., Castorina, F., Jourdan, F., Renne,
3818 P.R., N'ni, J., Nyobe, J.B., 2017. Mt. Bambouto Volcano, Cameroon Line: Mantle source and
3819
1362 Differentiation of Within-plate Alkaline Rocks. *J. Petrol.* 58, 933–962.
3820
1363 <https://doi.org/10.1093/petrology/egx041>.
3821
1364
3822
3823
1365
3824
3825
3826
3827
3828
3829
3830
3831
3832
3833
3834

3835
3836
3837
1366 Meyzen C.M., Marzoli A., Bellieni G., Levresse G., 2016. Magmatic activity on a motionless plate:
3838
3839 the case of East Island, Crozet Archipelago (Indian Ocean). *J. Petrol.* 57, 1409–1436.
3840
3841 <https://doi.org/10.1093/petrology/egw045>.
3842
3843
1369
3844
3845
1370 Milani, L., Beccaluva, L., Coltorti, M., 1999. Petrogenesis and evolution of the Euganean magmatic
3846
3847 complex, north eastern Italy. *Eur. J. Mineral.* 11, 379–399. <https://doi.org/10.1127/ejm/11/2/0379>.
3848
3849
1371
3850
1372
3851
3852
1373 Mollo, S., Blundy, J.D., Giacomoni, P.P., Nazzari, M., Coltorti, M., Langone, A., Andronico, D.,
3853
3854 2017. Clinopyroxene-melt element partitioning during interaction between trachybasaltic magma and
3855
3856 siliceous crust: clues from quartzites enclaves at Mt. Etna volcano. *Lithos* 284-285, 447-461.
3857
1375
3858 <http://dx.doi.org/10.1016/j.lithos.2017.05.003>.
3859
3860
1377
3861
3862
1378 Mollo, S., Putirka, K., Misiti, V., Soligo, M., Scarlato, P., 2013. A new test for equilibrium based on
3863
3864 clinopyroxene-melt pairs: clues on the solidification temperatures of Etnean alkaline melts at post-
3865
3866 eruptive conditions. *Chem. Geol.* 352, 92–100. <http://dx.doi.org/10.1016/j.chemgeo.2013.05.026>.
3867
3868
1380
3869
1381
3870
3871
1382 Morten, L., Taylor, L.A., Durazzo, A., 1989. Spinel in harzburgite and lherzolite inclusions from the
3872
3873 San Giovanni Ilarione Quarry, Lessini Mountains, Veneto Region, Italy. *Mineral. Petrol.* 40, 73–89.
3874
3875
1384 <https://doi.org/10.1007/BF01162470>.
3876
3877
1385
3878
3879
1386 Neave, D.A., Putirka, K., 2017. Clinopyroxene–liquid barometry revisited: magma storage pressures
3880
3881 under Icelandic rift zones. *Am. Mineral.* 102, 777–794. <http://dx.doi.org/10.2138/am-2017-5968>.
3882
3883
1387
3884
1388
3885
3886
1389 Neumann, F., Vázquez-Serrano, A., Tolson, G., Negrete-Aranda, R., Contreras, J., 2016. Toroidal,
3887
3888 counter-toroidal, and upwelling flow in the mantle wedge of the Rivera and Cocos plates:
3889
3890
3891
3892
3893

3894
3895
3896
1391 implications for IOB geochemistry in the Trans–Mexican Volcanic Belt. *Pure Appl. Geophys.* 176 ,
3897
3898
1392 3395–3417. https://doi.org/10.1007/978-3-319-51529-8_11.
3899
3900
1393
3901
3902
1394 Nievergelt, P., Liniger, M., Froitzheim, N., Mählmann, R., 1996. Early to mid Tertiary crustal
3903
3904 extension in the central Alps: The Turba mylonite zone (eastern Switzerland). *Tectonics* 15, 329–
1395
3905 340. <https://doi.org/10.1029/93TC02312>.
3906
1396
3907
3908
1397
3909
3910
1398 Niu, Y., Wilson, M., Humphreys, E.R., O’Hara, M.J., 2011. The origin of intra–plate ocean island
3911
3912 basalts (OIB): the lid effect and its geodynamic implications. *J. Petrol.* 52, 1443–1468.
3913
1399 <https://doi.org/10.1093/petrology/egr030>.
3914
1400
3915
3916
1401
3917
3918
1402 Oberli, F., Meier, M., Berger, A., Rosenberg, C.L., Gieré, R., 2004. U–Th–Pb and $^{230}\text{Th}/^{238}\text{U}$
3919
3920 disequilibrium isotope systematics: precise accessory mineral chronology and melt evolution tracing
3921
1403 in the Alpine Bergell intrusion. *Geochim. Cosmochim. Acta* 68, 2543–2560.
3922
1404 <https://doi.org/10.1016/j.gca.2003.10.017>.
3923
1405
3924
3925
1406
3926
3927
1407 Oostingh, K.F., Jourdan, F., Matchan, E.L., Phillips, D., 2017. Ar/Ar geochronology reveals rapid
3928
3929 change from plume–assisted to stress–dependent volcanism in the Newer Volcanic Province, SE
3930
1408 Australia. *Geochem. Geophys.* 18, 1–25. <https://doi.org/10.1002/2016GC006601>.
3931
3932
1409
3933
3934
1410
3935
3936
1411 Pacanovsky, K.M., Davis, D.M., Richardson R.M., Coblenz, D.D., 1999. Intraplate stresses and
3937
3938 plate–driving forces in the Philippine Sea plate. *J. Geophys. Res.* 104, 1095–1110.
3939
1412 <https://doi.org/10.1029/98JB02845>.
3940
1413
3941
3942
1414
3943
3944
1415 Pallares, C., Quidelleur, X., Gillot, P.Y., Kluska, J.M., Tchilinguirian, P., Sarda, P., 2016. The
3945
3946 temporal evolution of back–arc magmas from the Auca Mahuida shield volcano (Payenia Volcanic
3947
1416
3948
3949
3950
3951
3952

3953
3954
3955
1417 Province, Argentina). *J. Volcanol. Geotherm. Res.* 323, 19–37.
3956
3957
1418 <https://doi.org/10.1016/j.jvolgeores.2016.04.043>.
3958
3959
1419
3960
3961
1420 Panza, G.F., Suhadolc, P., 1990. Properties of the lithosphere in collisional belts in the
3962
3963 Mediterranean—A review. *Tectonophysics* 182, 39–46. <https://doi.org/10.1016/0040->
3964
3965 1951(90)90340-E.
3966
1422
3967
3968
1423
3969
3970
1424 Papazzoni, C.A., Giusberti, L., Carnevale, G., Roghi, G., Bassi, D., Zorzin, R., 2014. The Bolca
3971
3972 Fossil-Lagerstätten: A window into the Eocene World, ed. *Rendiconti della Società Paleontologica*
3973
3974
1426 *Italiana* 4.
3975
3976
1427
3977
3978
1428 Park, J., Levin, V., 2002. Seismic anisotropy: Tracing plate dynamics in the mantle. *Science* 296,
3979
3980 485–489. <https://doi.org/10.1126/science.1067319>.
3981
1429
3982
3983
1430
3984
3985
1431 Pedersen, T., Ro, H.E., 1992. Finite extension and decompression melting. *Earth Planet. Sci. Lett.*
3986
3987 113, 15–22. [https://doi.org/10.1016/0012-821X\(92\)90208-D](https://doi.org/10.1016/0012-821X(92)90208-D).
3988
3989
1433
3990
3991
1434 Pfänder, J.A., Jung, S., Klügel, A., Münker, C., Romer, R.L., Sperner, B., Rohrmüller, J., 2018.
3992
3993
1435 Recurrent local melting of metasomatised lithospheric mantle in response to continental rifting:
3994
3995 constraints from basanites and nephelinites/melilitites from SE Germany. *J. Petrol.* 59, 667–694.
3996
3997
1436
3998
1437 <https://doi.org/10.1093/petrology/egy041>.
3999
4000
1438
4001
4002
1439 Piccoli, G., Bellati, R., Binotti, C., Di Lallo, E., Sedeà, R., Dal Prà, A., Cataldi, R., Gatto, G.O.,
4003
4004
1440 Ghezzi, G., Marchetti, N., Bulgarelli, G., Schiesaro, G., Panichi, C., Tongiorgi, E., Baldi, P., Ferrara,
4005
4006 G.C., Massari, F., Medizza, F., Iliceto, V., Norinelli, A., De Vecchi, G., Gregnanin, A., Piccirillo,
4007
4008
4009
4010
4011

4012
4013
4014
1442 E.M., Sbettega, G., 1976. Il sistema idrotermale euganeo–berico e la geologia dei Colli Euganei.
4015
4016
1443 Mem. Ist. Geol. Min. Univ. Pad., 30, 266 pp.
4017
4018
1444
4019
4020
1445 Piccoli, G., Sedea, R., Bellati, R., Di Lallo, E., Medizza, F., Girardi, A., De Pieri, R., De Vecchi, Gp.,
4021
4022 Gregnanin, A., Piccirillo, E.M., Norinelli, A., Dal Prà, A., 1981. Note illustrative della carta geologica
4023
1446 dei Colli Euganei alla scala 1: 25.000. Memorie di Scienze geologiche 34, 523–546.
4024
4025
1447
4026
4027
1448
4028
4029
1449 Piromallo, C., Becker, T.W., Funicciello, F., Faccenna, C., 2006. Three-dimensional instantaneous
4030
4031
1450 mantle flow induced by subduction. Geophys. Res. Lett. 33, L08304–
4032
4033
1451 <https://doi.org/10.1029/2005GL025390>.
4034
4035
1452
4036
4037
1453 Piromallo, C., Faccenna, C., 2004. How deep can we find the traces of Alpine subduction?, Geophys.
4038
4039 Res. Lett. 31, L06605. <https://doi.org/10.1029/2003GL019288>.
4040
4041
1454
4042
1455
4043
4044
1456 Piromallo, C., Morelli, A., 2003. P wave tomography of the mantle under the Alpine-Mediterranean
4045
4046
1457 area. J. Geophys. Res. 108 (B2), 2065. <https://doi.org/10.1029/2002JB001757>.
4047
4048
1458
4049
4050
1459 Pleuger, J., Nagel, T.J., Walter, J.M., Jansen, E., Froitzheim, N., 2008. On the role and importance of
4051
4052
1460 orogen–parallel and –perpendicular extension, transcurrent shearing, and backthrusting in the Monte
4053
4054
1461 Rosa nappe and the Southern Steep Belt of the Alps (Penninic zone, Switzerland and Italy), in:
4055
4056
1462 Siegesmund, S., Fügenschuh B., Froitzheim, N. (Eds.). Tectonic aspects of the Alpine–Dinaride–
4057
4058
1463 Carpathian System. Geol. Soc. Spec. Publ. London 298, pp. 251–280.
4059
4060
1464 Putirka, K., 2008. Thermometers and Barometers for Volcanic Systems, in: Putirka, K., Tepley, F.
4061
4062
1465 (Eds.), Minerals, Inclusions and Volcanic Processes, Rev. Mineral. Geochem., Mineral. Soc. Am.,
4063
4064
1466 69, pp. 61–120.
4065
4066
4067
1467
4068
4069
4070

4071
4072
4073
1468 Putirka, K., Kuntz, M., Unruh, D., Vaid, N., 2009. Magma evolution and ascent at the Craters of the
4074
4075
1469 Moon and neighboring volcanic fields, southern ID, USA: implications for the evolution of
4076
4077
1470 polygenetic and monogenetic fields. *J.Petrol.*, 50, 1639–1665.
4078
4079
1471 <https://doi.org/10.1093/petrology/egp045>.
4080
4081
1472
4082
4083
1473 Putirka, K., Ryerson, F. J., Mikaelian, H., 2003. New igneous thermobarometers for mafic and
4084
4085
1474 evolved lava compositions, based on clinopyroxene + liquid equilibria. *Am. Mineral.*, 88, 1542–1554.
4086
4087
4088
1475
4089
4090
1476 Ratschbacher, L., Frisch, W., Linzer, H.G., Merle, O., 1991. Lateral extrusion in the Eastern Alps,
4091
4092
1477 Part 2: Structural analysis, *Tectonics* 10, 257–271. <https://doi.org/10.1029/90TC02623>.
4093
4094
1478
4095
4096
1479 Ratschbacher, L., Frisch, W., Neubauer, F., Schmid, S.M., Neugebauer, J., 1989. Extension in
4097
4098
1480 compressional orogenic belts: the eastern Alps. *Geology* 17, 404–407. [https://doi.org/10.1130/0091-7613\(1989\)017<0404:EICOBT>2.3.CO;2](https://doi.org/10.1130/0091-7613(1989)017<0404:EICOBT>2.3.CO;2).
4100
4101
1481
4102
4103
1482
4104
4105
1483 Ring, U., 1994. The kinematics of the late Alpine Muretto fault and its relation to eastward extension
4106
4107
1484 and to displacement at the Engadine and Periadriatic lines. *Eclog. Geol. Helv.* 87, 811–831.
4108
4109
1485
4110
4111
1486 Ring, U., Gerdens, A., 2016. Kinematics of the Alpenrhein–Bodensee graben system in the Central
4112
4113
1487 Alps: Oligocene/Miocene transtension due to formation of the Western Alps arc. *Tectonics* 35, 1367–
4114
4115
1488 1391. <https://doi.org/10.1002/2015TC004085>.
4116
4117
4118
1489
4119
4120
1490 Robinson, J.A.C., Wood, B.J., 1998. The depth of the spinel to garnet transition at the peridotite
4121
4122
1491 solidus. *Earth Planet. Sci. Lett.* 164, 277–284. [https://doi.org/10.1016/S0012-821X\(98\)00213-1](https://doi.org/10.1016/S0012-821X(98)00213-1).
4123
4124
1492
4125
4126
1493 Rosenbaum, G., Lister, G.S., 2005. The Western Alps from the Jurassic to Oligocene: spatio–
4127
4128
4129

4130
4131
4132
1494 temporal constraints and evolutionary reconstructions. *Earth Sci. Rev.* 69, 281–306.
4133
4134
1495 <https://doi.org/10.1016/j.earscirev.2004.10.001>.
4135
4136
1496
4137
4138
1497 Rosenbaum, G., Lister, G.S., Duboz, C., 2002. Relative motions of Africa, Iberia and Europe during
4139
4140
1498 Alpine orogeny. *Tectonophysics* 359, 117–129. [https://doi.org/10.1016/S0040-1951\(02\)00442-0](https://doi.org/10.1016/S0040-1951(02)00442-0).
4141
4142
1499
4143
4144
1500 Rosenberg, C.L., 2004. Shear zones and magma ascent: a model based on a review of the Tertiary
4145
4146
1501 magmatism in the Alps. *Tectonics* 23, TC3002. doi:10.1029/2003TC001526.
4147
4148
1502
4149
4150
1503 Rubatto, D., Gebauer, D., Fanning, M., 1998. Jurassic formation and Eocene subduction of the
4151
4152
1504 Zermatt–Saas–Fee ophiolites: implications for the geodynamic evolution of the Central and Western
4153
4154
1505 Alps. *Contrib. Mineral. Petrol.* 132, 269–287. <https://doi.org/10.1007/s004100050421>.
4155
4156
1506
4157
4158
1507 Sato, K., Katsura, T., Ito, E., 1997. Phase relations of phlogopite with and without enstatite up to 8
4159
4160
1508 GPa: implication to potassic magmatism and mantle metasomatism. *Earth Planet. Sci. Lett.* 146, 511–
4161
4162
1509 526. [https://doi.org/10.1016/S0012-821X\(96\)00246-4](https://doi.org/10.1016/S0012-821X(96)00246-4).
4163
4164
1510
4165
4166
1511
4167
4168
1512 Savage, M.K., 1999. Seismic anisotropy and mantle deformation: What have we learned from shear
4169
4170
1513 wave splitting?, *Rev. Geophys.* 37, 65–106. <https://doi.org/10.1029/98RG02075>.
4171
4172
1514
4173
4174
1515 Savage, M.K., Aoki, Y., Unglert, K., Ohkura, T., Umakoshi, K., Shimizu, H., Iguchi, M., Tameguri,
4175
4176
1516 T., Ohminato, T., Mori, J., 2016. Stress, strain rate and anisotropy in Kyushu, Japan. *Earth Planet.*
4177
4178
1517 *Sci. Lett.* 439, 129–142. <https://doi.org/10.1016/j.epsl.2016.01.005>.
4179
4180
4181
4182
4183
4184
4185
4186
4187
4188

4189
4190
4191
1518 Savage, M.K., Sheehan, A.F., 2000. Seismic anisotropy and mantle flow from the Great Basin to the
4192
4193
1519 Great Plains, western United States. *J. Geophys. Res.*, 105, 715–734
4194
4195
1520 <https://doi.org/10.1029/2000JB900021>.
4196
4197
1521
4198
4199
1522 Savelli, C., Lipparini, E. 1979. Età K/Ar di basalti del vicentino e la scala dei tempi del Paleogene.
4200
4201
1523 *Bollettino della Società Geologica Italiana* 98, 375–385.
4202
4203
1524
4204
4205
1525 Schaltegger, U., Brack, P., Ovtcharova, M., Peytcheva, I., Schoene, B., Stracke, A., Marocchi, M.,
4206
4207
1526 Bargossi, G.M., 2009. Zircon and titanite recording 1.5 million years of magma accretion,
4208
4209
1527 crystallization and initial cooling in a composite pluton (southern Adamello batholith, northern Italy).
4210
4211
1528 *Earth Planet. Sci. Lett.* 286, 208–218. <https://doi.org/10.1016/j.epsl.2009.06.028>.
4212
4213
1529
4214
4215
1530 Schlunegger, F., Kissling, E. 2015. Slab rollback orogeny in the Alps and evolution of the Swiss
4216
4217
1531 Molasse basin. *Nat. Commun.* 6, 8605, 1–10. <https://doi.org/10.1038/ncomms9605>.
4218
4219
1532
4220
4221
1533 Schmid, S.M., Fügenschuch, B., Kissling, E., Schuster, R., 2004. Tectonic map and overall
4222
4223
1534 architecture of the Alpine orogen. *Eclogae Geol. Helv.* 97, 93–117. <https://doi.org/10.1007/s00015->
4224
4225
1535 004-1113-x.
4226
4227
1536
4228
4229
1537 Schmid, S.M., Kissiling E., Diehl, T., van Hinsbergen D.J.J, Molli, G., 2017. Ivrea mantle wedge,
4230
4231
1538 arc of the Western Alps, and kinematic evolution of the Alps–Apennines orogenic system. *Swiss J.*
4232
4233
1539 *Geosci.* 110, 581–612. <https://doi.org/10.1007/s00015-016-0237-0>.
4234
4235
1540
4236
4237
1541 Schmidt, K.H., Bottazzi, P., Vannucci, R., Mengel, K., 1999. Trace element partitioning between
4238
4239
1542 phlogopite, clinopyroxene and leucite lamproite melt. *Earth Planet. Sci. Lett.* 168, 287–299.
4240
4241
1543 [https://doi.org/10.1016/S0012-821X\(99\)00056-4](https://doi.org/10.1016/S0012-821X(99)00056-4).
4242
4243
4244
4245
4246
4247

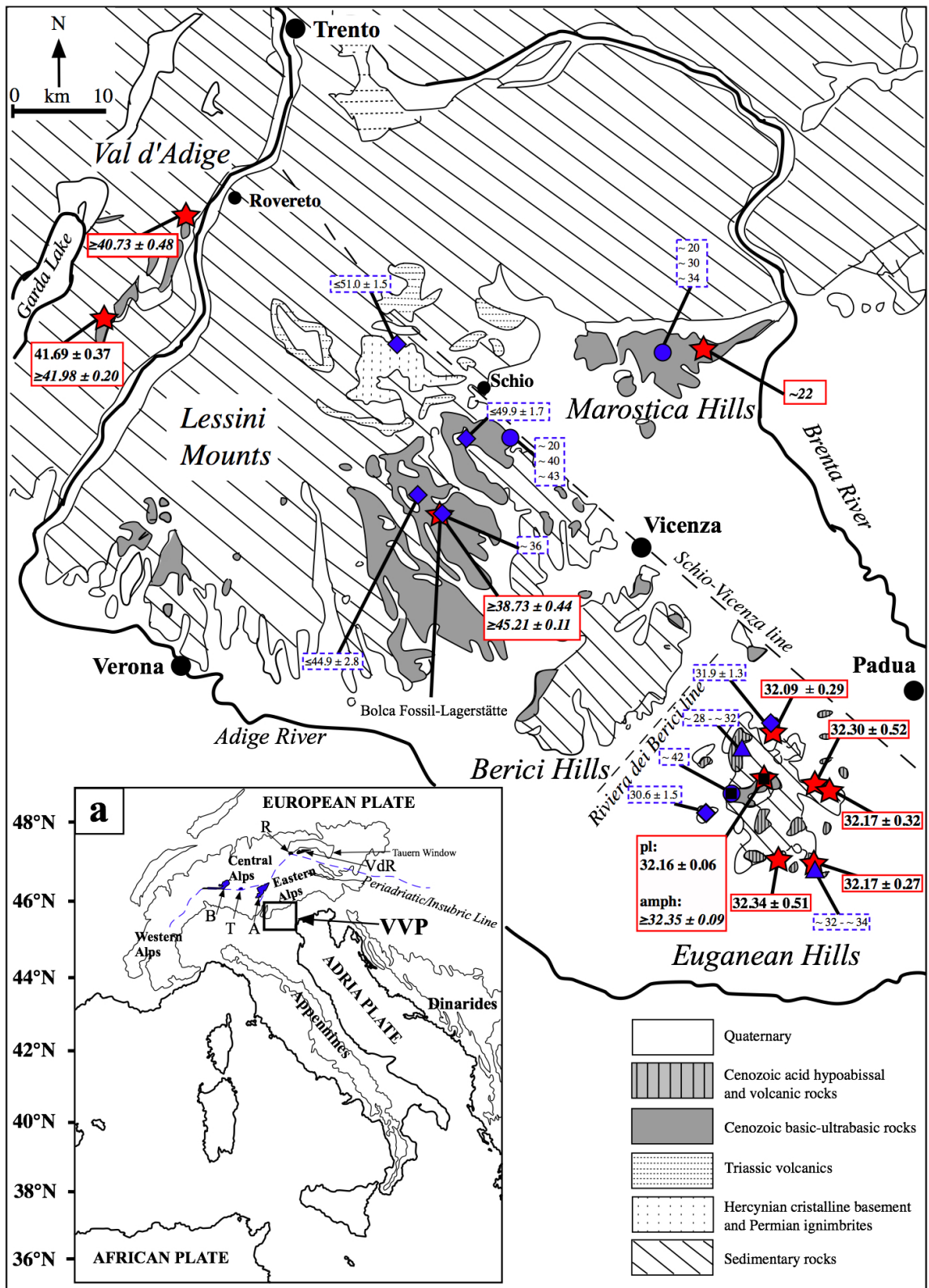
4248
4249
4250
1544
4251
4252
1545 Schmitz, M.D., Bowring, S.A., Ludwig, K.R., Renne, P.R., 2003. Comment on “Precise K–Ar, ⁴⁰Ar–
4253
4254 ³⁹Ar, Rb–Sr and U–Pb mineral ages from the 27.5 Fish Canyon Tuff reference standard” by M.A.
4255
4256 Lanphere and H. Baadsgaard. *Chem. Geol.* 199, 277–280. [https://doi.org/10.1016/S0009–
4258 2541\(03\)00078–0](https://doi.org/10.1016/S0009–
4257 2541(03)00078–0).
4259
4260
4261
1549
4262
4263
1550 Schoene, B., Schaltegger, U., Brack, P., Latkoczy, C., Stracke, A., Günther, D., 2012. Rates of magma
4264
4265 differentiation and emplacement in a ballooning pluton recorded by U–Pb TIMS–TEA, Adamello
4266
4267 batholith, Italy. *Earth Planet. Sci. Lett.* 355, 162–173. <https://doi.org/10.1016/j.epsl.2012.08.019>.
4268
4269
1553
4270
4271
1554 Seghedi I., Matenco L., Downes H., Mason P.R.D., Szakács A., Pécskay Z., 2011. Tectonic
4272
4273 significance of changes in post-subduction Pliocene–Quaternary magmatism in the south east part of
4274
4275 the Carpathian–Pannonian Region. *Tectonophysics* 502, 146–157.
4276
4277 <https://doi.org/10.1016/j.tecto.2009.12.003>.
4278
4279
1558
4280
4281
4282
1559 Shaw, D.M., 1970. Trace element fractionation during anatexis. *Geochim. Cosmochim. Acta* 34,
4283
4284 237–243. [https://doi.org/10.1016/0016–7037\(70\)90009–8](https://doi.org/10.1016/0016–7037(70)90009–8).
4285
4286
1561
4287
4288
1562 Siena, F., Coltorti, M., 1989. Lithospheric mantle evolution: evidences from ultramafic xenoliths in
4289
4290 the Lessinean volcanics (Northern Italy). *Chem. Geol.* 77, 347–364.
4291
4292
1564
4293
4294
1565 Siena, F., Coltorti, M., 1993. Thermobarometric evolution and metasomatic processes of upper
4295
4296 mantle in different tectonic settings: evidence from spinel peridotite xenoliths. *Eur. J. Mineral.* 5,
4297
4298 1073–1090.
4299
4300
1567
4301
4302
1568
4303
4304
1569 Singer, J., Diehl, T., Hunsen, S., Kissiling, E., Duretz, T., 2014. Alpine lithosphere slab rollback
4305
4306

4307
4308
4309
1570 causing lower crustal seismicity in northern foreland. *Earth Planet. Sci. Lett.* 397, 42–56.
4310
4311
1571 <https://doi.org/10.1016/j.epsl.2014.04.002>.
4312
4313
1572
4314
4315
1573 Sokol, A.G., Kruk, A.N., Palyanov, Y.N., Sobolev, N.V., 2017. Stability of phlogopite in
4316
4317 ultrapotassic kimberlite-like systems at 5.5–7.5 GPa. *Contrib. Mineral., Petrol.* 172, 21.
4318
1574
4319
4320
1575 <https://doi.org/10.1007/s00410-017-1341-5>.
4321
4322
1576
4323
4324
1577 Sorbini, L., 1989. *I fossili di Bolca*. Museo Civico di Storia Naturale di Verona, Verona.
4325
4326
1578
4327
4328
1579 Stampfli, G.M., Borel, G.D., Marchant, R., Mosar J., 2002. Western Alps geological constraints on
4329
4330 western Tethyan reconstruction, in: Rosenbaum, G., Lister, G., S., 2002. Reconstruction of the
4331
1580
4332 evolution of the Alpine–Himalayan Orogen. *J. Virt. Expl.* 7, 75–104.
4333
1581
4334
4335
1582
4336
4337
1583 Stampfli, G.M., Mosar, J., Marquer, D., Marchant, R., Baudin, T., Borel, G., 1998. Subduction and
4338
4339 obduction processes in the Swiss Alps. *Tectonophysics* 296, 159–204.
4340
1584
4341
1585 [https://doi.org/10.1016/S0040-1951\(98\)00142-5](https://doi.org/10.1016/S0040-1951(98)00142-5)
4342
4343
1586
4344
4345
1587 Steck, A., 2008. Tectonics of the Simplon massif and Lepontine gneiss dome: Deformation structures
4346
4347 due to collision between the underthrusting European plate and the Adriatic indenter. *Swiss J. Geosci.*
4348
1588
4349
1589 101, 515–546. <https://doi.org/10.1007/s00015-008-1283-z>.
4350
4351
1590
4352
4353
4354
1591 Strak, V., Schellart, W.P., 2014. Evolution of 3–D subduction–induced mantle flow around lateral
4355
4356 slab edges in analogue models of free subduction analysed by stereoscopic particle image velocimetry
4357
1592
4358
1593 technique. *Earth Planet. Sci. Lett.* 403, 368–379. . <https://doi.org/10.1016/j.epsl.2014.07.007>.
4359
4360
1594
4361
4362
4363
4364
4365

4366
4367
4368
1595 Su, B.-X., Zhang, H.-F., Sakyi, P.A., Ying, J.-F., Tang, Y.-J., Yang, Y.-H., Qin, K.-Z., Xiao, Y.,
4369
4370
1596 Zhao, X.-M., 2010. Compositionally stratified lithosphere and carbonatite metasomatism recorded
4371
4372
1597 in mantle xenoliths from Western Qinling (Central China). *Lithos* 116, 111–128.
4373
4374
1598 <https://doi.org/10.1016/j.lithos.2010.01.004>.
4375
4376
1599
4377
4378
1600 Sun, S.S., McDonough, W.F., 1989. Chemical and isotopic systematics of oceanic basalts:
4379
4380
1601 implications for mantle composition and processes, in: Saunders, A.D, Norry, M.J. (Eds.),
4381
4382
1602 *Magmatism in the Oceanic Basins*. Geol. Soc. Spec. Publ. London 42, pp. 313–346.
4383
4384
1603
4385
4386
1604 Thirlwall, M.F., Upton, B.G.J., Jenkins, C., 1994. Interaction between continental lithosphere and the
4387
4388
1605 Iceland plume. Sr–Nd–Pb isotope chemistry of Tertiary basalts, NE Greenland. *J. Petrol.* 35, 839–
4389
4390
1606 897. <https://doi.org/10.1093/petrology/35.3.839>.
4391
4392
4393
1607
4394
4395
1608 Tiepolo, M., Oberti, R., Zanetti, A., Vannucci, R., Foley, S.F., 2007. Trace–element partitioning
4396
4397
1609 between amphibole and silicate melt. *Rev. Mineral. Geochem.* 67, 417–452.
4398
4399
1610 <https://doi.org/10.2138/rmg.2007.67.11>.
4400
4401
1611
4402
4403
1612 van Hunen, J., Allen, M.B., 2011. Continental collision and slab breakoff: a comparison of 3–D
4404
4405
1613 numerical models with observations. *Earth Planet. Sci. Lett.* 302, 27–37.
4406
4407
1614 <https://doi.org/10.1016/j.epsl.2010.11.035>.
4408
4409
4410
1615
4411
4412
1616 van Westrenen, W., Blundy, J.D., Wood, B.J., 2001. High field strength element/rare element
4413
4414
1617 fractionation during partial melting in the presence of garnet: implications for identification of mantle
4415
4416
1618 heterogeneities. *Geochem. Geophys.*, 2000GC000133. <https://doi.org/10.1029/2000GC000133>.
4417
4418
4419
1619
4420
4421
1620 Verati, C., Jourdan, F., 2013. Modelling effect of sericitization of plagioclase on the $^{40}\text{K}/^{40}\text{Ar}$ and
4422
4423
4424

4425
4426
4427
1621 ⁴⁰K/³⁹Ar chronometers: Implication for dating basaltic rocks and mineral deposits, in: Jourdan, F.,
4428
4429
1622 Mark, D.F., Verati, C. (Eds.), *Advances in ⁴⁰Ar/³⁹Ar dating: from archaeology to planetary sciences.*
4430
4431
1623 *Geol. Soc. Spec. Publ. London* 378, pp. 155–174. <https://doi.org/10.1144/SP378.24>.
4432
4433
1624 Verma, S.P., 2002. Absence of Cocos plate subduction related basic volcanism in southern Mexico:
4434
4435
1625 A unique case on Earth?. *Geology* 30, 1095–1098. <https://doi.org/10.1130/0091->
4436
4437
1626 [7613\(2002\)030<1095:AOCPSR>2.0.CO;2](https://doi.org/10.1130/0091-7613(2002)030<1095:AOCPSR>2.0.CO;2).
4438
4439
4440
1627
4441
4442
1628 Visonà, D., Caironi, V., Carraro, A., Dallai, L., Fioretti, A.M., Fanning, M., 2007. Zircon megacrysts
4443
4444
1629 from basalts of the Venetian Volcanic Province (NE Italy): U–Pb, oxygen isotopes and REE data.
4445
4446
1630 *Lithos* 94, 168–180. <https://doi.org/10.1016/j.lithos.2006.06.007>.
4447
4448
1631
4449
4450
1632 von Blanckenburg, F., 1992. Combined high–precision chronometry and geochemical tracing using
4451
4452
1633 accessory minerals: applied to the Central-Alpine Bergell intrusion (central Europe). *Chem. Geol.*
4453
4454
1634 100, 19–40. [https://doi.org/10.1016/0009-2541\(92\)90100-J](https://doi.org/10.1016/0009-2541(92)90100-J).
4455
4456
1635
4457
4458
1636 von Blanckenburg, F., Davies, J.H., 1995. Slab breakoff: a model for syncollisional magmatism and
4459
4460
1637 tectonics in the Alps. *Tectonics* 14, 120–131. <https://doi.org/10.1029/94TC02051>.
4461
4462
1638
4463
4464
1639 Wilson, M., Downes, H., 1992. Mafic alkaline magmatism in the European Cenozoic rift system.
4465
4466
1640 *Tectonophysics* 208, 173–182. [https://doi.org/10.1016/0040-1951\(92\)90343-5](https://doi.org/10.1016/0040-1951(92)90343-5).
4467
4468
1641
4469
4470
1642 Winterer, E.L., Bosellini, A., 1981. Subsidence and sedimentation on a Jurassic passive continental
4471
4472
1643 margin (Southern Alps, Italy). *Bulletin American Association of Petroleum Geologists* 65, 394–421.
4473
4474
1644
4475
4476
1645 Yaxley, G.M., Crawford, A.J., Green, D.H., 1991. Evidence for carbonatite metasomatism in spinel
4477
4478
1646 peridotite xenoliths from western Victoria, Australia. *Earth Planet. Sci. Lett.* 107, 305–317.
4479
4480
4481
4482
4483

4484
4485
4486
1647 [https://doi.org/10.1016/0012-821X\(91\)90078-V](https://doi.org/10.1016/0012-821X(91)90078-V).
4487
4488
1648
4489
4490
1649 Zampieri, D., 1995. Tertiary extension in the southern Trento Platform, Southern Alps, Italy.
4491
4492
1650 *Tectonics* 14, 645–657. <https://doi.org/10.1029/94TC03093>.
4493
4494
1651
4495
4496
1652 Zanazzi, P.F., Pavese, A., 2002. Behavior of micas at high pressure and high temperature. *Rev.*
4498
4499
1653 *Mineral. Geochem.* 46, 98–116. <https://doi.org/10.2138/rmg.2002.46.02>
4500
4501
1654
4502
4503
1655 Zantendeschi, C., 1994. New Rb–Sr radiometric data from Colli Euganei (North Eastern Italy). *Mem.*
4504
4505
1656 *Ist. Geol. Min. Univ. Pad.* 46, 17–22.
4506
4507
1657
4508
4509
1658 Zhao, L., Paul, A., Malusà, M.G., Xiaobing, X., Zheng, T., Solarino, S., Guillot, S., Schwartz, S.,
4510
4511
1659 Dumont, T., Salimbeni, S., Aubert, A., Pondrelli, S., Wang, Q., Zhu, R., 2016. Continuity of the
4513
4514
1660 Alpine slab unraveled by high-resolution P wave tomography. *J. Geophys. Res.: Solid Earth* 121,
4515
4516
1661 8720–8737. <https://doi.org/10.1002/2016JB013310>.
4517
4518
1662
4519
4520
1663 Ziberna, L., Klemme, S., Nimis, P., 2013. Garnet and spinel in fertile and depleted mantle: insights
4521
4522
1664 from thermodynamic modelling. *Contrib. Mineral. Petrol.* 166, 411–421.
4523
4524
1665 <https://doi.org/10.1007/s00410-013-0882-5>.
4525
4526
4527
4528
4529
4530
4531
4532
4533
4534
4535
4536
4537
4538
4539
4540
4541
4542



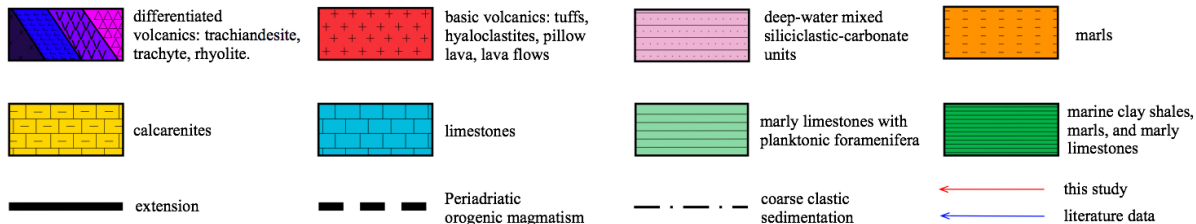
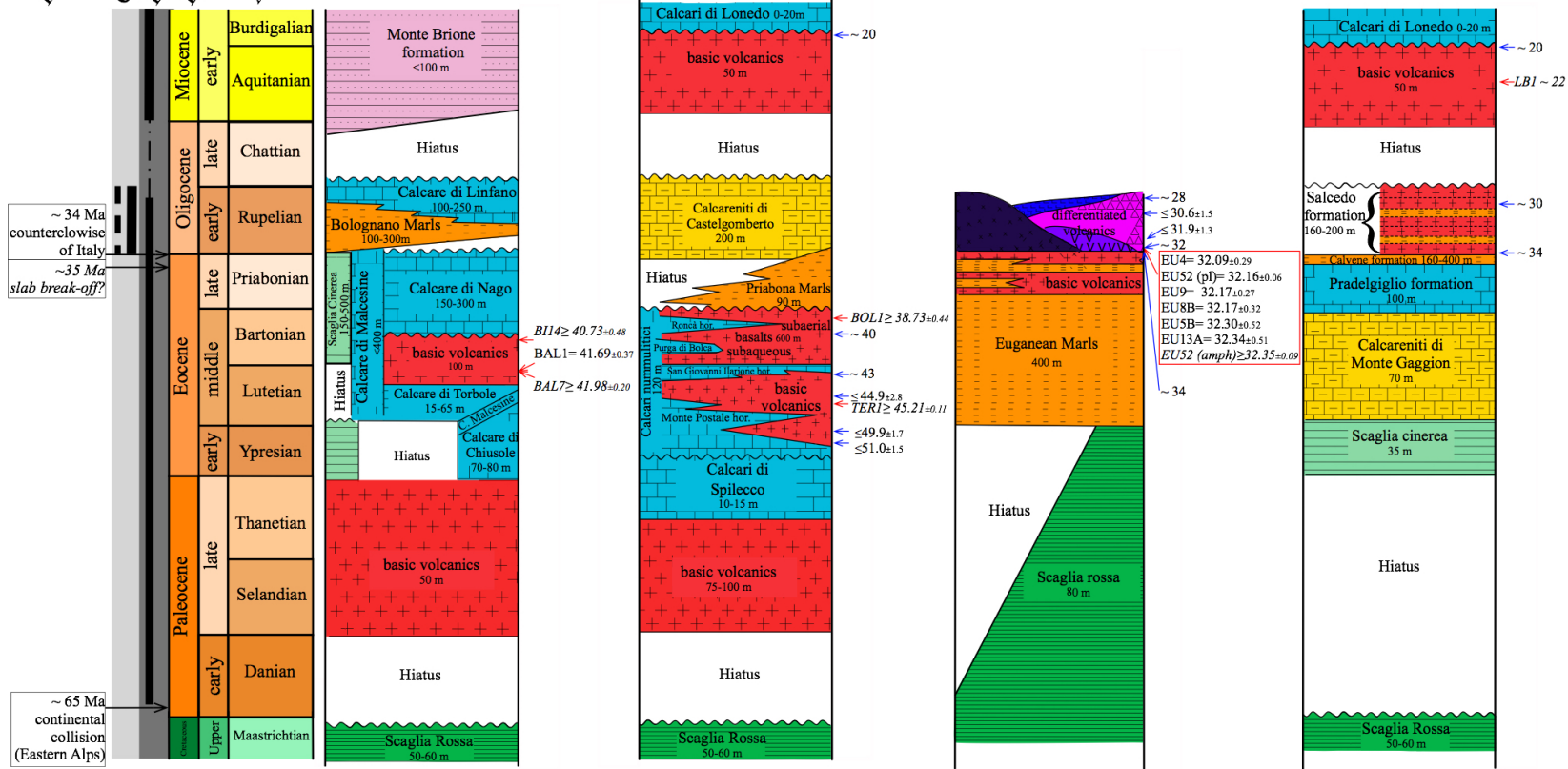
Principal events
Central Alps
Eastern Alps
Epoch
Age

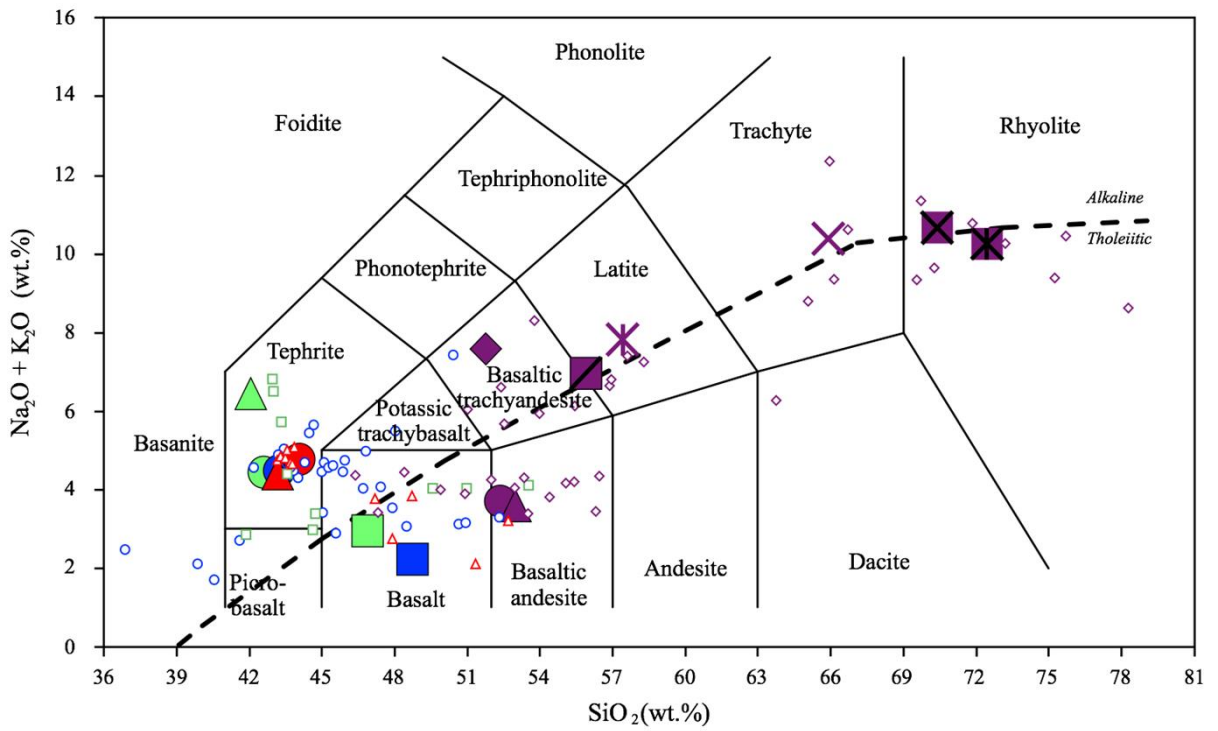
Monte Baldo-
northern sector
(Val d'Adige)

Eastern Lessini Mts.

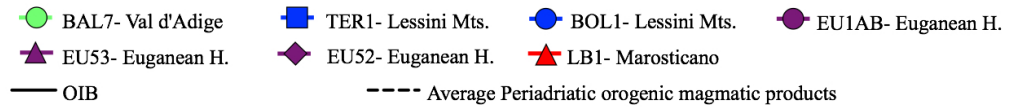
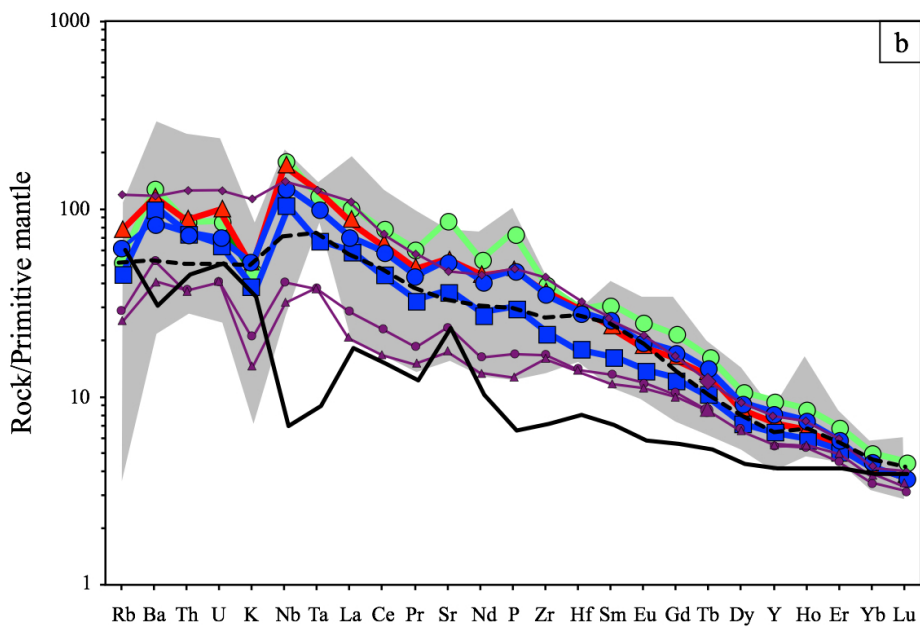
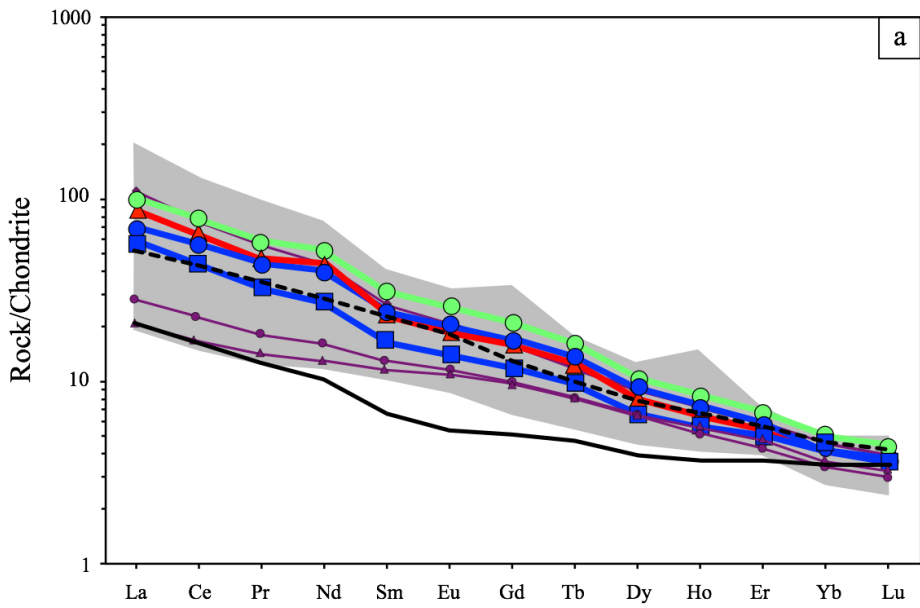
Euganean Hills

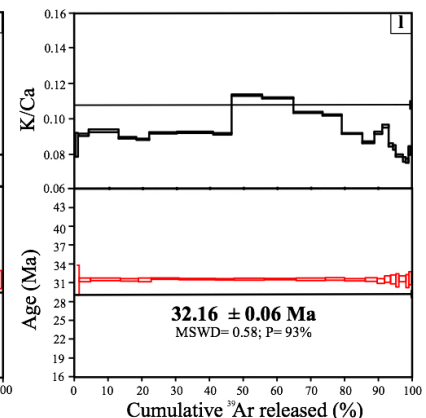
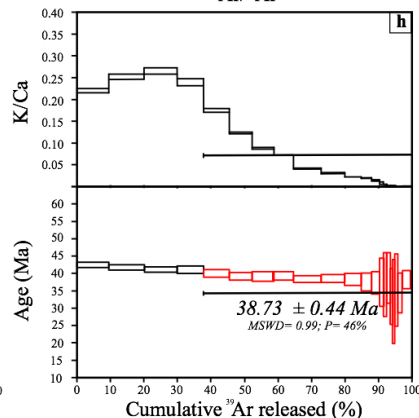
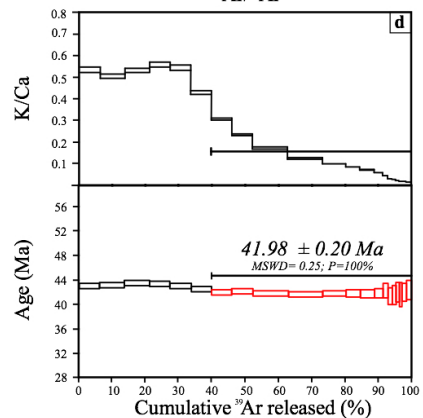
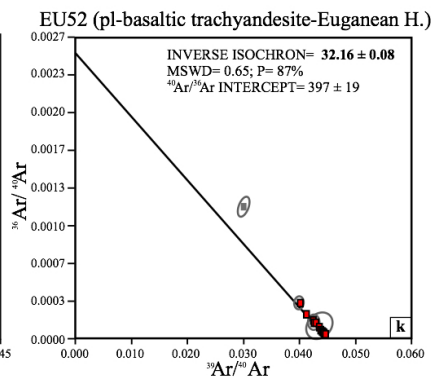
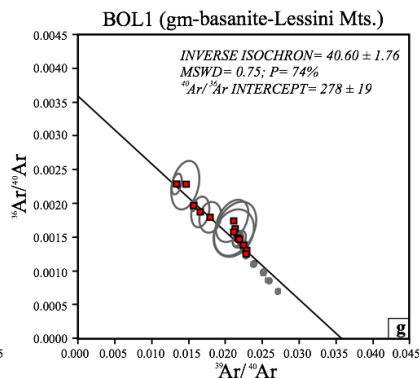
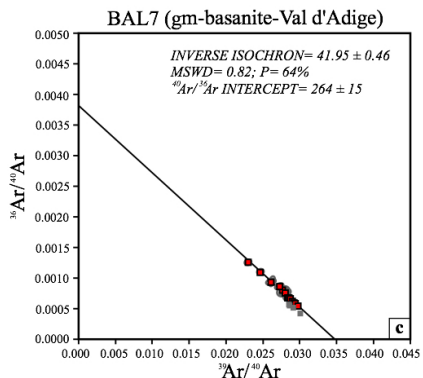
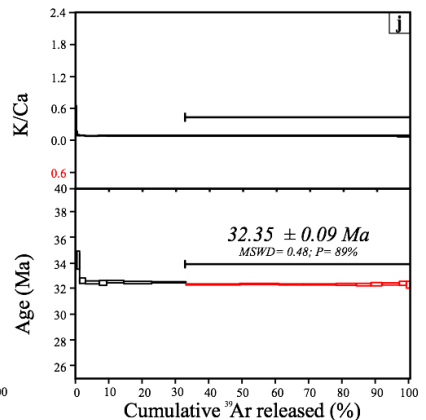
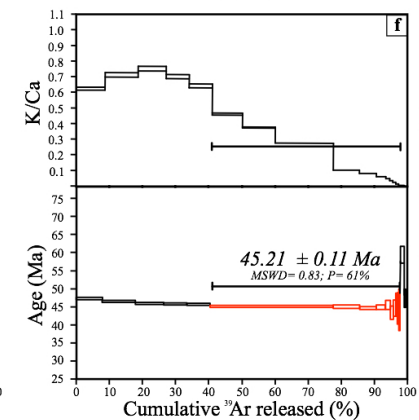
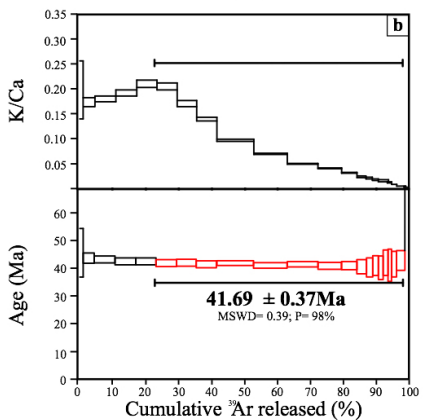
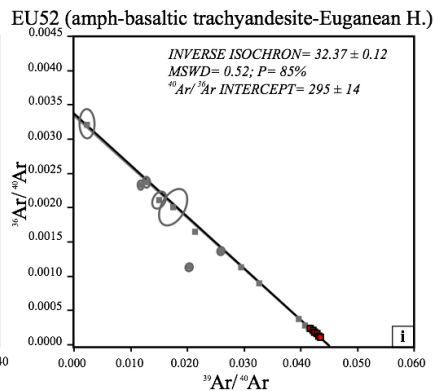
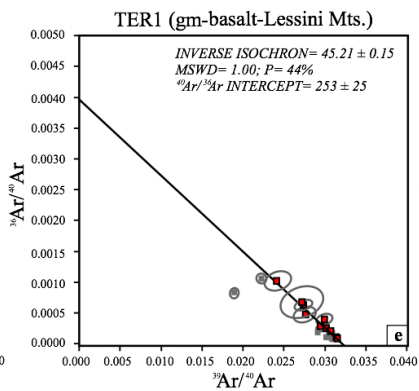
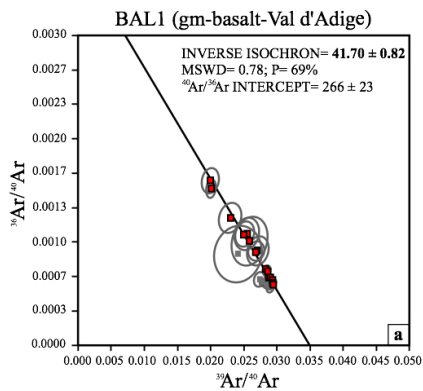
Marosticano



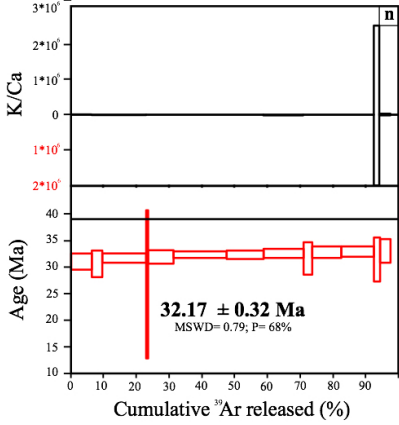
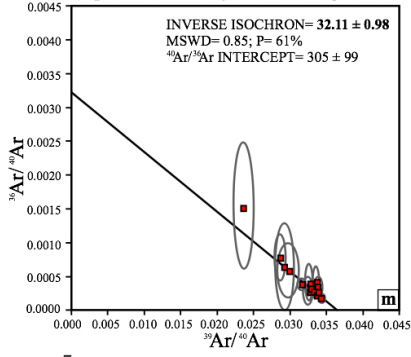


- | | | | | |
|---------------------|---------------------|----------------------|----------------------|----------------------|
| ■ BAL1- Val d'Adige | ● BAL7- Val d'Adige | ▲ BI14- Val d'Adige | ■ TER1- Lessini Mts. | ● BOL1- Lessini Mts. |
| ▲ LB1- Marosticano | ● 25B- Marosticano | ● EU1AB- Euganean H. | ✕ EU4- Euganean H. | ■ EU5B- Euganean H. |
| ■ EU8B- Euganean H. | ✕ EU9- Euganean H. | ✕ EU13A- Euganean H. | ◆ EU52- Euganean H. | ▲ EU53- Euganean H. |
| □ Val d'Adige | ○ Lessini Mts. | △ Marosticano | ◇ Euganean Hills | |

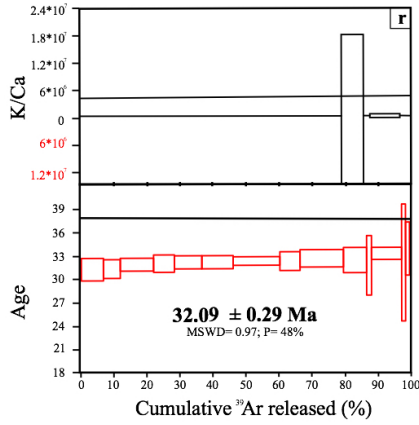
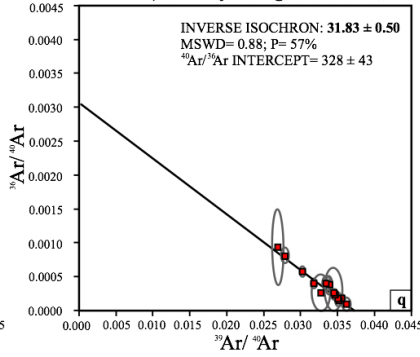




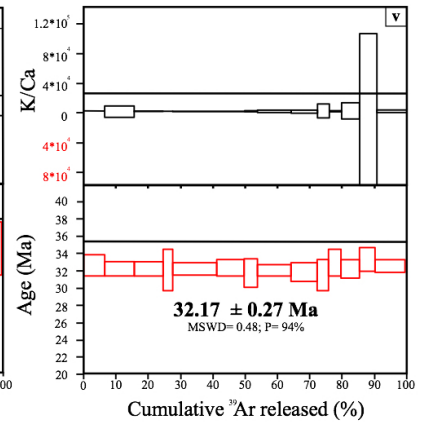
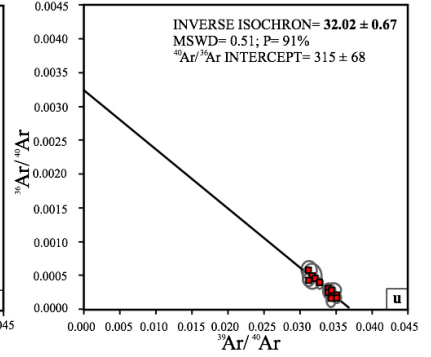
EU8B (fsp-basaltic trachyandesite-Euganean H.)



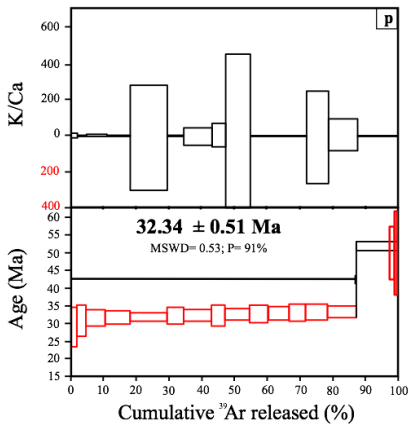
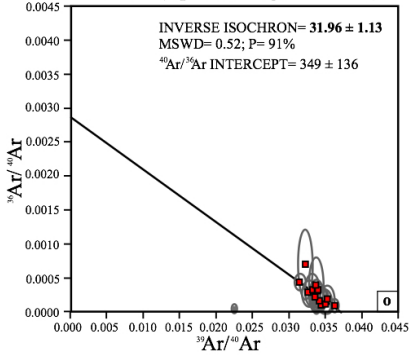
EU4 (bt-trachyte-Euganean Hills)



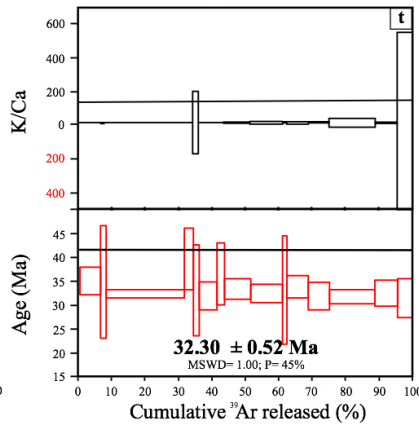
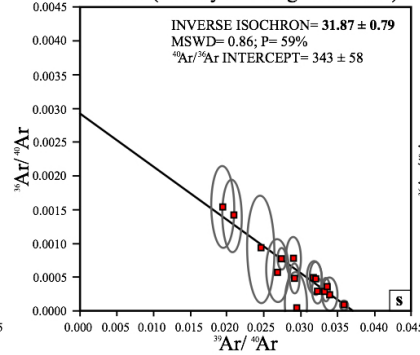
EU9 (san-rhyolite-Euganean Hills)



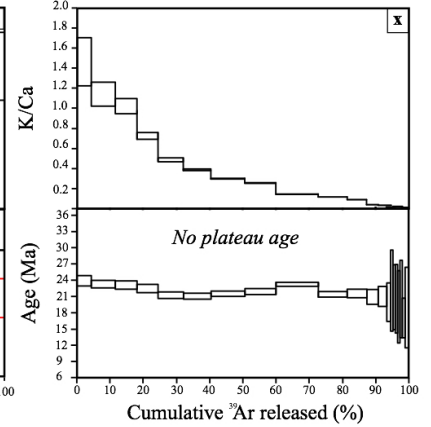
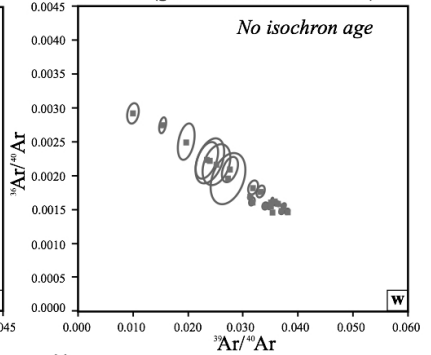
EU13A (fsp-latite-Euganean Hills)

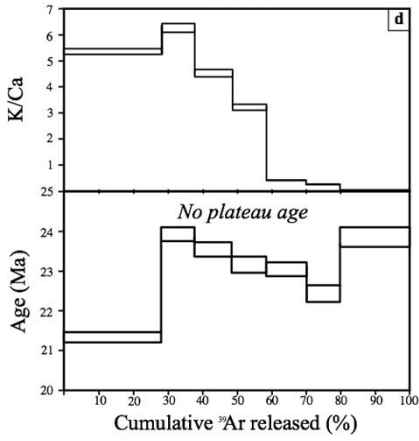
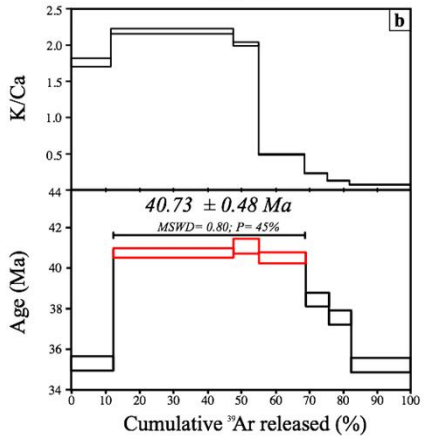
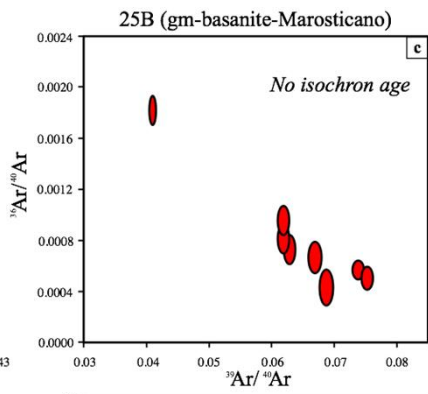
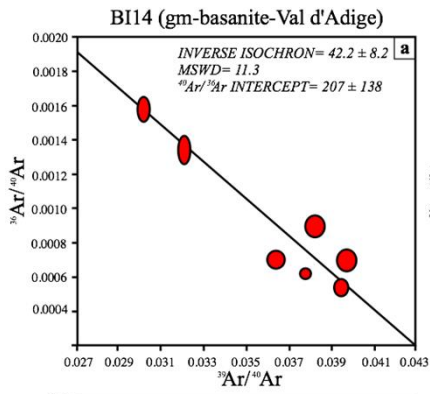


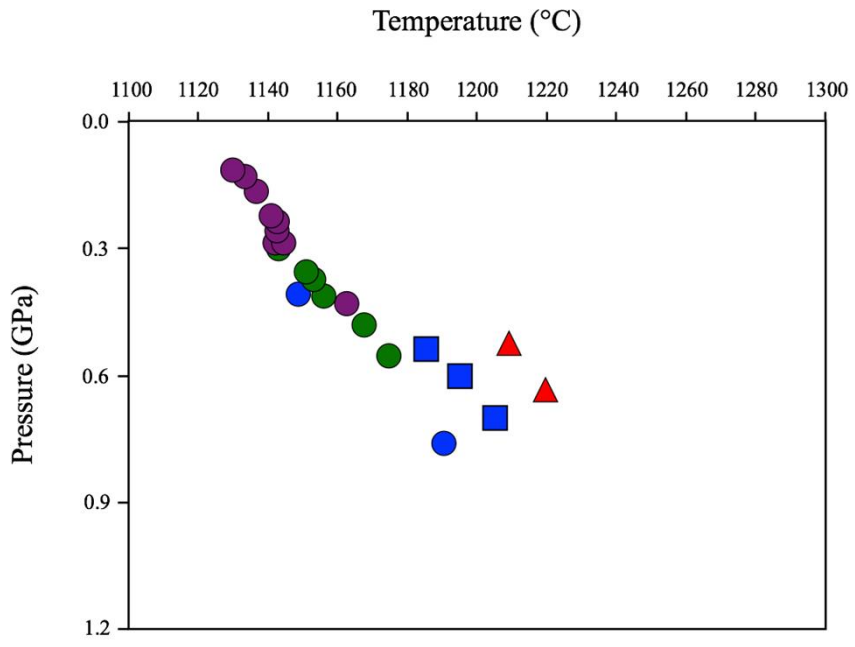
EU5B (san-rhyolite-Euganean Hills)



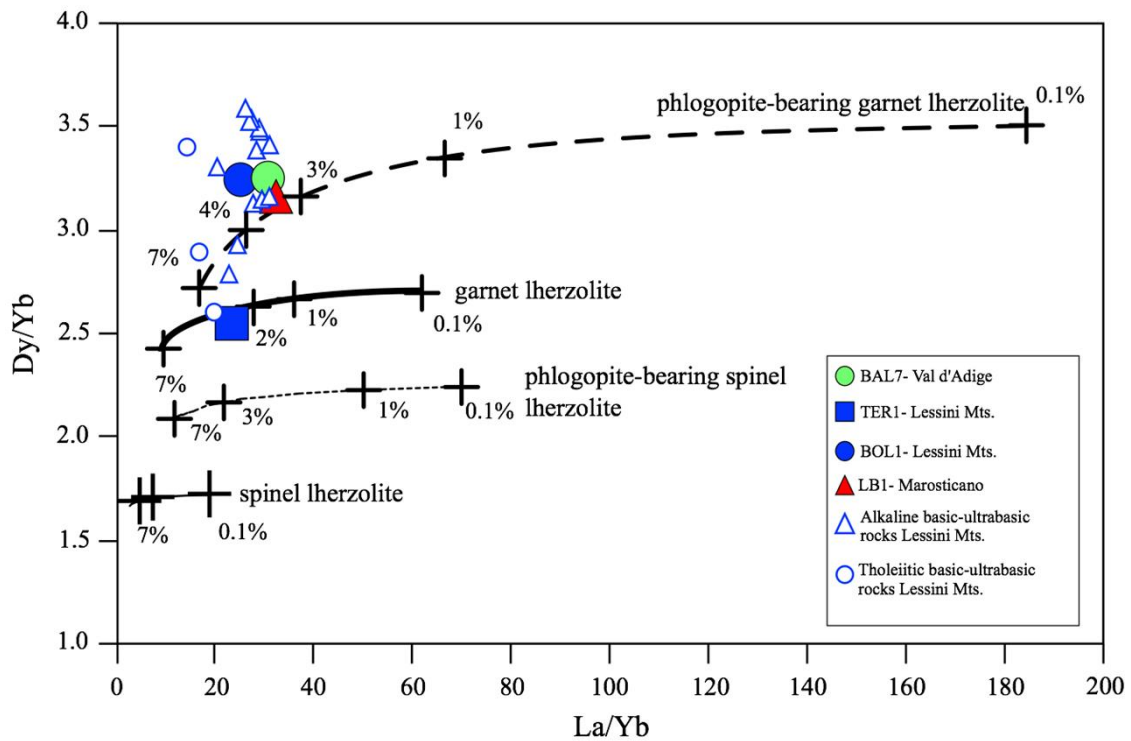
LB1 (gm-basanite-Marosticano)

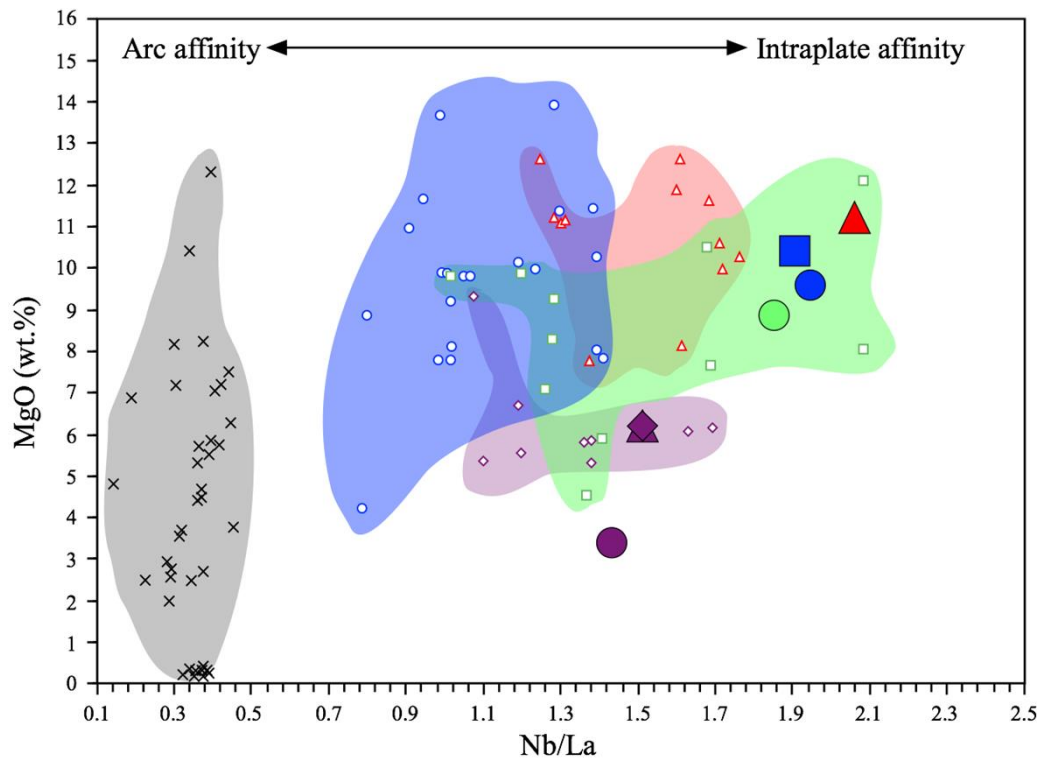




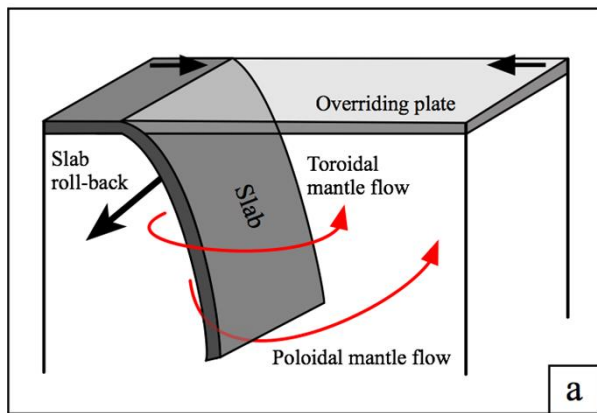


- BAL7- Val d'Adige
- TER1- Lessini Mts.
- BOL1- Lessini Mts.
- EU1AB- Euganean H.
- ▲ LB1- Marosticano





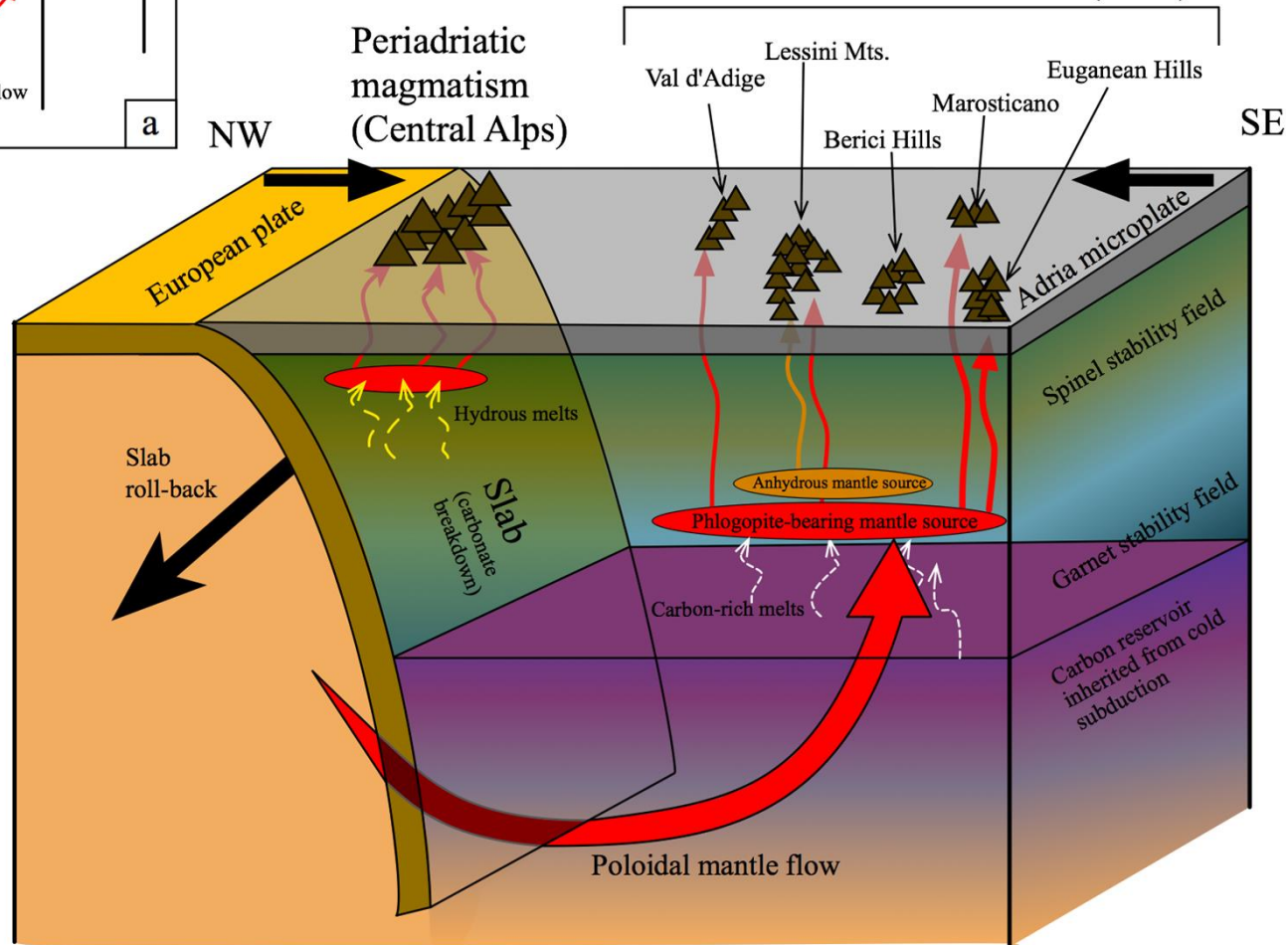
- | | | | |
|---------------------------------------|----------------------|----------------------|----------------------|
| ● BAL7- Val d'Adige | ■ TER1- Lessini Mts. | ● BOL1- Lessini Mts. | ● EU1AB- Euganean H. |
| ▲ EU53- Euganean H. | ◆ EU52- Euganean H. | ▲ LB1- Marosticano | |
| □ Val d'Adige | ○ Lessini Mts. | ◇ Euganean Hills | △ Marosticano |
| × Periadriatic Central Alps magmatism | | | |



Eocene-Oligocene

← Extension →

Veneto Volcanic Province (VVP)



SUPPLEMENTARY MATERIAL

Intraplate magmatism at a convergent plate boundary, the case of the Cenozoic northern Adria magmatism

Valentina Brombin^a, Costanza Bonadiman^{a*}, Fred Jourdan^b, Guido Roghi^c, Massimo Coltorti^a,
Laura E. Webb^d, Sara Callegaro^e, Giuliano Bellieni^f, Giampaolo De Vecchi^f, Roberto Sedeaf^f
Andrea Marzoli^{c,f}

^a *Dipartimento di Fisica e Scienze della Terra, Università di Ferrara, Italy*

^b *Western Australian Argon Isotope Facility, School of Earth and Planetary Sciences & JdL Centre, Curtin University, Perth, Western Australia, Australia;*

^c *Istituto di Geoscienze e Georisorse, CNR, Padova, Italy*

^d *Department of Geology, University of Vermont, Vermont, USA;*

^e *Centre for Earth Evolution and Dynamics, University of Oslo, Norway;*

^f *Dipartimento di Geoscienze, Università di Padova, Italy*

S1. ANALYTICAL METHODS

S1.1. Major and trace elements

Whole-rock major and trace elements of samples BAL1, BAL7, BI14, TER1, BOL1, LB1, and 25B were determined by Wavelength Dispersive X-Ray Fluorescence Spectrometry (WDXRF) on pressed powder pellets at the Department of Physics and Earth Sciences, University of Ferrara (Italy), using an ARL Advant-XP spectrometer, following the full matrix correction method proposed by Lachance and Traill (1966). Accuracy is generally lower than 2% for major oxides and less than 5% for trace

element determinations, whereas the detection limits for trace elements range from 1 to 2 ppm. Volatile contents were determined as loss on ignition (LOI) at 1000 °C.

Whole-rock major and trace elements of samples EU1AB, EU53, EU52, EU8B, EU13A, EU4, EU5B, and EU9, were determined by X-Ray Fluorescence Spectrometry (XRF) on glass bead samples at the Department of Geosciences, University of Padova (Italy), using Phillips PW1404. Analytical uncertainty ranges from 1 to 2% for major elements and from 10 to 15% for trace elements. LOI was measured at 1000 °C. In addition, Rb, Sr, Y, Zr, Nb, Hf, Ta, Th, U, and Rare Earth elements (REEs) of samples BAL7, TER1, BOL1 and LB1 were determined by Inductively Coupled Plasma–Mass Spectrometry (ICP-MS) using a Thermo Series X-I spectrometer at Department of Physics and Earth Sciences, University of Ferrara. Accuracy and detection limits were determined using several international reference standards, as well as internal standards run as unknowns. Same analyses for samples EU4, EU9, EU8B, EU13A, and EU52 were performed using a Thermo Element2 HR-ICP-MS at University of Bretagne Occidentale, Brest (France), after a repeated HF-HClO₄ digestion and HNO₃ dilutions (see Li and Lee, 2006 for details). The repeated analysis of the international standards BCR-2 and BIR-1 demonstrated an external reproducibility better than 5–10 % depending on the element and concentration.

Clinopyroxene compositions of samples BAL7, TER1, BOL1, EU1AB, and LB1 were determined *in-situ* by means of a CAMECA SX50 electron microprobe (EMP) at the IGG–CNR of Padova. using ZAF on-line data reduction and matrix correction procedures.

S1.2. Analytical procedure for ⁴⁰Ar/³⁹Ar radio-isotopic dating

Basaltic and basaltic samples from Val d'Adige, Lessini Mts., and Marosticano districts (BAL1, BAL7, BOL1, TER1, LB1, BI14, and 25B) lack K-rich minerals suitable for geochronology, therefore ⁴⁰Ar/³⁹Ar analyses were performed on groundmass. The sample fraction (30-40 g) was crushed with a rigorously cleaned steel hydraulic press, sieved to a size fraction of 90-250 µm and rinsed in distilled H₂O to remove any dust or powder. In order to collect only the sample grains

constituted by the groundmass, the sample fraction was handpicked under a binocular microscope to remove any phenocrysts (pyroxene and olivine). However, due to the dark color of these grains it was impossible to clearly observe if inclusions were present, and therefore exclude the possibility of alteration. The grains were leached in dilute HF in order to remove at least the alteration phases along the surface and cracks. Samples were then rinsed in distilled H₂O in an ultrasonic cleaner.

As basaltic trachyandesites (EU52, EU8B), latite (EU13A), trachyte (EU4), and rhyolites (EU5B, EU9) from the Euganean district are characterized by phenocrysts that are good candidates for ⁴⁰Ar/³⁹Ar dating, *i.e.*, plagioclase and amphibole in the most basic sample, and biotite, sanidine, or feldspar in the more acid samples, ⁴⁰Ar/³⁹Ar analyses were performed on mineral separates. The sample fraction (>1kg) was crushed with a rigorously cleaned steel hydraulic press, sieved to size fractions of 150-215 µm and 215-315 µm, and rinsed in distilled H₂O to remove any dust or powder. Phenocrysts were separated from these fractions using a Frantz isodynamic magnetic separator and were hand-picked grain-by-grain under the binocular stereomicroscope. Mineralic separates were further leached using diluted HF (2N) for 5 minutes to remove any potential adhering alteration product within superficial cracks that were not removed during hand picking (Jourdan et al., 2009b) and then were rinsed in distilled H₂O in an ultrasonic cleaner.

The Ar isotopic ratios were measured through laser step-heating with i) ARGUS VI (samples BAL1, BAL7, BOL1, TER1, EU52, and EU52) and ii) MAP 215–50 (samples EU4, EU5B, EU8B, and EU13A) mass spectrometers at Curtin University within the Western Australian Argon Isotope Facility (WAAIF) of the John de Laeter Centre and iii) Nu Instruments Noblesse magnetic sector noble gas mass spectrometer (samples BI14 and 25B) at the Noble Gas Lab of the University of Vermont. Irrespective to the instrument used for the analyses, our criteria for the determination of plateau are as follows. Plateaus must include at least 70% of ³⁹Ar. The plateau should be distributed over a minimum of 3 consecutive steps agreeing at 95% confidence level and satisfying a probability of fit (P) of at least 0.05. Plateau ages at the 2σ. All the plateau ages are calculated using the mean of all the plateau steps, each weighted by the inverse variance of their individual analytical error. Mini-

plateaus are defined similarly except that they include between 50% and 70% of ^{39}Ar . Inverse isochrons include the maximum number of steps with a probability of fit ≥ 0.05 . All sources of uncertainties are included in the calculation.

The sample irradiations and the analytical procedures performed are reported in detail below.

S1.3. Sample irradiation and analyses for samples analysed with ARGUS VI mass spectrometer

The cleaned groundmass (BAL1, BAL7, TER1, BOL1, LB1) and mineral separates (EU52) were loaded into several 1.9 cm in diameter by 0.3 cm depth aluminum discs. The discs were then stacked together and placed in quartz tubes. The discs hosting the groundmass included also GA1550 biotite, while the discs hosting plagioclase and amphibole included FCs. GA1550 and FCs were used as neutron fluence monitors, adopting an age of 99.738 ± 0.100 Ma and 28.294 ± 0.036 Ma (1σ), respectively (Renne et al., 2011). The discs were Cd-shielded (to minimize undesirable nuclear interference reactions) and irradiated for 3 hours at the TRIGA Reactor at Oregon State University (USA). The mean J-values computed from standard grains within the small pits range from 0.0008098 ($\pm 0.07\%$) to 0.0008121 ($\pm 0.11\%$) for groundmass sample and yielded values of 0.0008098 ($\pm 0.07\%$) and 0.0008121 ($\pm 0.13\%$) for the plagioclase and hornblende samples, respectively. For all the samples, the mass discrimination was monitored regularly through the analysis using an automated air pipette and provided the mean value is 0.993485 ($\pm 0.02\%$) per dalton (atomic mass unit) relative to an air ratio of 298.56 ± 0.31 (Lee et al., 2006). The correction factors for interfering isotopes were $(^{39}\text{Ar}/^{37}\text{Ar})_{\text{Ca}} = 6.95 \times 10^{-4}$ ($\pm 1.3\%$), $(^{36}\text{Ar}/^{37}\text{Ar})_{\text{Ca}} = 2.65 \times 10^{-4}$ ($\pm 0.84\%$) and $(^{40}\text{Ar}/^{39}\text{Ar})_{\text{K}} = 7.30 \times 10^{-4}$ ($\pm 12.4\%$; Renne et al., 2013). At the WAAIF plagioclase, amphibole crystal and groundmass populations were step-heated using a continuous 100 W PhotonMachine© CO₂ (IR, 10.4 μm) laser fired on the crystals during 60 seconds. Each of the standard crystals was fused in a single step. The gas was purified in an extra low-volume stainless steel extraction line of 240cc and using one SAES AP10 and one GP50 getter. Ar isotopes were measured in static mode using a low volume (600 cc) ARGUS VI mass spectrometer from Thermofisher© set with a permanent resolution of ~ 200 .

Measurements were carried out in multi-collection mode using four faradays to measure mass 40 to 37 and a 0-background compact discrete dynode ion counter to measure mass 36. We measured the relative abundance of each mass simultaneously using 10 cycles of peak-hopping and 33 seconds of integration time for each mass. Detectors were calibrated to each other electronically and using Air shot beam signals. The raw data were processed using the ArArCALC software (Koppers, 2002) and the ages have been calculated using the decay constants recommended by Renne et al. (2011). Blanks were monitored every 2 steps.

S1.4. Sample irradiation and analyses for samples analysed with MAP 215-50 mass spectrometer

Euganean mineral separates (EU8B, EU13A, EU4, EU5B, EU9) were loaded into five large wells of two 1.9 cm diameter by 0.3 cm depth aluminum discs. In one disc the wells were bracketed by small pits that included GA1550 biotite, while in the other disc, the wells were bracketed by seven pits that included Fish Canyon sanidine (FCs). GA1550 and FCs were used as neutron fluence monitors, adopting an age of 99.738 ± 0.100 Ma and 28.294 ± 0.036 Ma (1σ), respectively (Renne et al., 2011). The discs were Cadmium-shielded (to minimize undesirable nuclear interference reactions) and irradiated for 3 hours in the US Geological Survey nuclear reactor (Denver, USA) in central position. The mean J-values computed from standard grains within the small pits is 0.000661 ± 0.00000099 (0.15%) determined as the average and standard deviation of J-values of the small wells for each irradiation disc. Mass discrimination was monitored using an automated air pipette and provided a mean value ranging from 1.006254 ± 0.00030188 (0.03%) to 1.006589 ± 0.00030198 (0.03%) per dalton (atomic mass unit) relative to an air ratio of 298.56 ± 0.31 (Lee et al., 2006). The correction factors for interfering isotopes were $(^{39}\text{Ar}/^{37}\text{Ar})_{\text{Ca}} = 7.30 \times 10^{-4}$ ($\pm 11\%$), $(^{36}\text{Ar}/^{37}\text{Ar})_{\text{Ca}} = 2.82 \times 10^{-4}$ ($\pm 1\%$), and $(^{40}\text{Ar}/^{39}\text{Ar})_{\text{K}} = 6.76 \times 10^{-4}$ ($\pm 32\%$). At the WAAIF the samples were step-heated using a 110 W Spectron Laser Systems, with a continuous Nd-YAG (IR; 1064 nm) laser rastered over the sample during 1 minute to ensure an homogeneously distributed temperature. The gas was purified in

a stainless steel extraction line using two SAES AP10 getters, a GP50 getter and a liquid nitrogen condensation trap. Ar isotopes were measured in static mode using a MAP 215-50 mass spectrometer (resolution of ~ 500 ; sensitivity of 4×10^{-14} mol/V) with a Balzers SEV 217 electron multiplier mostly using 9 to 10 cycles of peak-hopping. The data acquisition was performed with the Argus program written by M.O. McWilliams and ran under a LabView environment. The raw data were processed using the ArArCALC software (Koppers, 2002) and the ages have been calculated using the decay constants recommended by Renne et al. (2010). Blanks were monitored every 3 to 4 steps and typical ^{40}Ar blanks range from 1×10^{-16} to 2×10^{-16} mol.

S1.5. Sample irradiation and analyses for samples analysed with Nu Instruments Noblesse magnetic sector noble gas mass spectrometer

The cleaned groundmass were loaded into aluminum foil packets, arranged in suprasil vial, and placed in an aluminum canister for irradiation. Samples were irradiated with multigrain aliquots of FCs to act as a flux monitor (age: 28.03 Ma; Renne et al., 1998) to monitor the neutron dose, and CaF_2 and KSO_4 were also irradiated to determine corrections for interfering nuclear reactions. Samples were irradiated for four hours at the Cd-Lined In-Core Irradiation Tube (CLICIT) reactor of Oregon State University, USA. Correction factors used to account for interfering nuclear reactions for the irradiated samples are: $(^{40}\text{Ar}/^{39}\text{Ar})_{\text{K}} = 8.87 \times 10^{-3} \pm 5.30 \times 10^{-3}$, $(^{36}\text{Ar}/^{37}\text{Ar})_{\text{Ca}} = 2.7 \times 10^{-4} \pm 0.2 \times 10^{-4}$, $(^{39}\text{Ar}/^{37}\text{Ar})_{\text{Ca}} = 6.7 \times 10^{-4} \pm 0.2 \times 10^{-4}$. At the Noble Gas Lab of the University of Vermont, laser step heating for $^{40}\text{Ar}/^{39}\text{Ar}$ dating was conducted with a Santa Cruz Laser Microfurnace 75 W diode laser system. Flux monitors were loaded into degassed Nb foil packets before being loaded in the wells of the copper planchette sample holder. The volcanic samples were loaded directly into wells of the copper planchette. The gas released during heating was purified with SAES getters and argon isotopes were analysed on a Nu Instruments Noblesse magnetic sector noble gas mass spectrometer during step-heating analyses. Data from samples and flux monitors were corrected for blanks, mass discrimination, atmospheric argon, neutron-induced interfering isotopes, and the decay of ^{37}Ar and

^{39}Ar . Mass discrimination was calculated by analyzing known aliquots of atmospheric argon for which the measured $^{40}\text{Ar}/^{36}\text{Ar}$ was compared with an assumed atmospheric value of 298.56 ± 0.31 (Lee et al., 2006). A linear interpolation was used to calculate J factors for samples based on sample position between flux monitor packets in the irradiation tube. All ages were calculated using the isotope decay constants recommended by Steiger and Jäger (1977). The age calculations for inverse isochron and apparent age data were achieved using both an in-house data reduction program and Isoplot 3.0 (Ludwig, 2003).

S2. RESULTS FROM $^{40}\text{Ar}/^{39}\text{Ar}$ GEOCHRONOLOGICAL ANALYSES

All ages obtained and here reported correspond to plateau ages corrected for deviations from the atmospheric $^{40}\text{Ar}/^{36}\text{Ar}$ ratio of 298.56 ± 0.31 (Lee et al., 2006). For most samples, the $^{40}\text{Ar}/^{36}\text{Ar}$ ratios are above or below the atmospheric values. Supra-atmospheric values can be explained by the presence of excess ^{40}Ar (e.g., Oostingh et al., 2017), whereas the sub-atmospheric values are indicative of fluid circulation and alteration. In fact ^{36}Ar concentrations are extremely low in mantle derived magmas and fluids, therefore $^{40}\text{Ar}/^{36}\text{Ar}$ ratio of a predominantly magmatic fluid is sensitive to trace additions of hydrothermal fluids (Burnard and Polyá, 2004). For these reasons, in this study ages from samples with low $^{40}\text{Ar}/^{36}\text{Ar}$ ratios have been considered as only minimum ages.

The basalt BAL1 from Val d'Adige shows an inverse isochron age of 41.70 ± 0.82 Ma [mean square weighted deviation (MSWD) = 0.78; probability (P) = 69%; Table 3; Fig. 5a]. The measured intercept of the inverse isochron indicates an initial $^{40}\text{Ar}/^{36}\text{Ar}$ value of 266 ± 23 , which is slightly below the atmospheric value (298.56 ± 0.31 ; Lee et al., 2006). Using the $^{40}\text{Ar}/^{36}\text{Ar}$ intercept value, we calculated a plateau age of 41.69 ± 0.37 Ma (MSWD = 0.39; P = 98%; Table 3; Fig. 5b) based on 75% of the total gas. From the same district, the basanite BAL7 yielded an inverse isochron age of 41.95 ± 0.46 Ma (MSWD = 0.82; P = 64; Table 3; Fig. 5c). Like the previous sample, the $^{40}\text{Ar}/^{36}\text{Ar}$ intercept value is sub-atmospheric (264 ± 15 Ma); this allows calculate a mini-plateau age of 41.98 ± 0.20 Ma (MSWD = 0.25; P = 100%), including 60% of the released ^{39}Ar (Table 3; Fig. 5d). Both in BAL1 and

BAL7, the K/Ca spectra show typical trends observed for basaltic rock fragments with relatively high values (0.20-0.55) at the low temperature steps that decrease steadily (0.10 to 0.00) towards higher temperature steps, indicating that the K-rich phases degassed predominantly at lower temperatures and high Ca/K-phases dominate at higher temperatures (Fig. 5b, d). TER1 and BOL1 are a basalt and a basanite, respectively, analysed for the Lessini Mts. district and yielded different ages. TER 1 yielded an inverse isochron age of 45.21 ± 0.15 Ma (MSWD = 1.00; P = 44%; Table 3; Fig. 5e). The sub-atmospheric $^{40}\text{Ar}/^{36}\text{Ar}$ (253 ± 25) defines a mini-plateau age of 45.21 ± 0.11 Ma (MSWD = 0.83; P = 61%) including 57% of the released ^{39}Ar (Table 3; Fig. 5f). In general the K/Ca ratio decrease from 0.75 to 0.01. BOL1 yielded an inverse isochron age of 40.60 ± 1.76 Ma (MSWD = 0.75; P = 74%; Table 3; Fig. 5g). The $^{40}\text{Ar}/^{36}\text{Ar}$ intercept is 278 ± 19 , close to the atmospheric $^{40}\text{Ar}/^{36}\text{Ar}$ ratio. This sample yielded a mini-plateau age of 38.73 ± 0.44 Ma (MSWD = 0.99; P = 46%) based on 62% of the total gas (Table 3; Fig. 5h). The basanite BOL1 shows the lowest K/Ca (0.27 to 0.007) of all analysed samples (Fig. 5h).

The amphibole separate of basaltic trachyandesite EU52 yielded an inverse isochron age of 32.37 ± 0.12 Ma (MSWD = 0.52; P = 85%; Table 3; Fig. 5i), with $^{40}\text{Ar}/^{36}\text{Ar}$ intercept (295 ± 14) indistinguishable from atmosphere and yielded a mini-plateau age of 32.35 ± 0.09 Ma (MSWD = 0.48; P = 89%) based on 67% of ^{39}Ar (Table 3; Fig. 5j). The K/Ca spectrum is flat and the values (0.098 to 0.104) are low, as expected for amphibole (Fig. 5j). The plagioclase inverse isochron age of EU52 is 32.16 ± 0.08 Ma (MSWD = 0.65; P = 87%; Table 3; Fig. 5k). The $^{40}\text{Ar}/^{36}\text{Ar}$ intercept value is 397 ± 19 and may indicate presence of excess ^{40}Ar . Using the latter value we obtained a plateau age of 32.16 ± 0.06 Ma (MSWD = 0.58; P = 93%), based on 99.5% of the gas (Table 3; Fig. 5l). It should however be considered that the low K/Ca makes all steps cluster at very low $^{40}\text{Ar}/^{36}\text{Ar}$ intercepts. The K/Ca values range from 0.079 to 0.114, consistent with the plagioclase separate analysed (Fig. 5l). The alkali-feldspar separate of basaltic trachyandesite EU8B shows an inverse isochron age of 32.11 ± 0.98 Ma (MSWD = 0.85; P = 61%; Table 3; Fig. 5m). Using its $^{40}\text{Ar}/^{36}\text{Ar}$ intercept value (305 ± 99) we obtained a plateau age of 32.17 ± 0.32 Ma (MSWD = 0.79; P = 68%;

Table 3; Fig. 5n), defined by 100% of the released ^{39}Ar . The high K/Ca values (10-5478) are consistent with the mineral phase analysed (Fig. 5n). For the feldspar separate of the latite EU13A we obtained an inverse isochron age of 31.96 ± 1.13 (MSWD = 0.52; P = 91%; Table 3; Fig. 5o). The $^{40}\text{Ar}/^{36}\text{Ar}$ intercept is 349 ± 136 and defines a plateau age of 32.34 ± 0.51 Ma (MSWD = 0.53; P = 91%) that includes 88% of the total ^{39}Ar (Table 3; Fig. 5p). Despite their large uncertainties, the K/Ca values (0.58-12.50) are consistent with the low-Ca plagioclase phase analysed (Fig. 5p). The inverse age for the biotite separate of trachyte EU4 is 31.83 ± 0.50 Ma (MSWD = 0.88; P = 57%; Table 3; Fig. 5q). The $^{40}\text{Ar}/^{36}\text{Ar}$ intercept is 328 ± 43 and defines a plateau age of 32.09 ± 0.29 Ma (MSWD = 0.97; P = 48%) based on 100% of the total released gas (Table 3; Fig. 5r). The K/Ca spectrum is flat and the high ratios (157-3762) are consistent with the mineral phase analysed (Fig. 5r). The sanidine separate of rhyolite EU5B yielded an inverse isochron age of 31.87 ± 0.79 Ma (MSWD = 0.86; P = 59%; Table 3; Fig. 5s) with $^{40}\text{Ar}/^{36}\text{Ar}$ intercept slightly supra-atmospheric (343 ± 58 ; Fig. 5s). The calculated plateau age is 32.30 ± 0.52 Ma (MSWD = 1.00; P = 45%) defined by 100% of the released ^{39}Ar (Table 3; Fig. 5t). The K/Ca spectrum is flat with typical ratios for sanidine (0.02-2.48) (Fig. 5t). The sanidine separate of rhyolite EU9 shows inverse isochron ages of 32.02 ± 0.67 Ma (MSWD = 0.51; P = 91%; Table 3; Fig. 5u). With the $^{40}\text{Ar}/^{36}\text{Ar}$ intercept value (315 ± 68) indistinguishable from atmosphere, the calculated plateau age is 32.17 ± 0.27 Ma (MSWD = 0.48; P = 94%; Table 3; Fig. 5v), defined by 100% of the gas released. The K/Ca spectrum is flat and exhibits typical values for the mineral phase analysed (42-2233; Fig. 5v). It is clear that irrespective to the lithology all analysed Euganean samples yielded nearly indistinguishable ages, which allow us to calculate a mean weighted age of 32.21 ± 0.09 Ma.

The basanite from Marosticano district, LB1, it is the most recent aged VVP sample analysed at WAAIF using the ARGUS VI mass spectrometer. It did not return isochron and plateau ages, but almost all the steps indicate apparent ages between 20.5 and 23.2 Ma (Table 3; Fig. 5w, x). The K/Ca diagram shows a monotonically decreasing plot from 1.69 to 0.003 (Fig. 5x).

The samples BI14 and 25B, two basanites from Val d'Adige and Marosticano, respectively, were analysed at the Noble Gas Geochronology Laboratory of the University of Vermont using the Nu Instruments Noblesse magnetic sector noble gas mass spectrometer with the purpose to expand the VVP geochronological dataset. Despite the poor fit of the measured inverse isochrons, the results from these samples are concordant with the Val d'Adige and Marosticano samples analysed at the WAAIF. For the sample BI14 the $^{40}\text{Ar}/^{36}\text{Ar}$ intercept of the inverse isochron is 207 ± 138 (Table 4; Fig. 6a) defining a mini-plateau age (40.73 ± 0.48 Ma; MSWD = 0.80; Table 4; Fig. 6b) based on 57% of the released ^{39}Ar . The calculated age is similar to BAL1 and BAL7 ages. In the first three steps the K/Ca ranges from 1.8 to 2.3, while in the last steps it decrease from 0.5 to 0.1 (Fig. 6b). As the LB1, also the sample 25B did not provide isochron and plateau ages and the K/Ca decreases (0.06-6.27; Table 4; Fig. 6c, d). In fact, for both Marosticano samples, almost all the steps indicate apparent ages of $\sim 22 - 23$ Ma.

REFERENCES

- Burnard, P.G., Polya, D.A. 2004. Importance of mantle derived fluids during granite associated hydrothermal circulation: He and Ar isotopes of ore minerals from Panasqueira. *Geochim. Cosmochim. Acta* 68, 1607-1615. <https://doi.org/10.1016/j.gca.2003.10.008>.
- Jourdan, F., Marzoli, A., Bertrand, H., Cirilli, S., Tanner, L.H., Kontak, D.J., McHone, G., Renne, P.R., Bellieni, G., 2009b. $^{40}\text{Ar}/^{39}\text{Ar}$ ages of CAMP in North America: Implications for the Triassic–Jurassic boundary and the ^{40}K decay constant bias. *Lithos* 110, 167-18. <https://doi.org/10.1016/j.lithos.2008.12.011>.
- Koppers, A.A.P., 2002. ArArCALC-software for $^{40}\text{Ar}/^{39}\text{Ar}$ age calculations. *Comput. and Geosci.* 28, 605–619. [https://doi.org/10.1016/S0098-3004\(01\)00095-4](https://doi.org/10.1016/S0098-3004(01)00095-4).

Lachance, G.R., Traill, R.J., 1966. Practical solution to the matrix problem in X-ray analysis. *Can. J. Spectros.* 11, 43-48.

Lee, J.-Y., Marti, K., Severinghaus, J.P., Kawamura, K., Yoo, H.-S., Lee, J.B., Kim, J.S., 2006. A redetermination of the isotopic abundance of atmospheric Ar. *Geochim. Cosmochim. Acta* 70, 4507-4512. <https://doi.org/10.1016/j.gca.2006.06.1563>.

Li, Z.-X. A., Lee, C.-T. A., 2006. Geochemical investigation of serpentized oceanic lithospheric mantle in the Feather River Ophiolite, California: Implications for the re-cycling rate of water by subduction, *Chem. Geol.* 235, 161–185. <https://doi.org/10.1016/j.chemgeo.2006.06.011>.

Ludwig, K.R., 2003. Isoplot/EX, rev. 3.00, a Geochronological Toolkit for Microsoft Excel. Berkeley Geochronology Center Special Publication 4, 71 pp.

Oostingh, K.F., Jourdan, F., Matchan, E.L., Phillips, D., 2017. Ar/Ar geochronology reveals rapid change from plume-assisted to stress-dependent volcanism in the Newer Volcanic Province, SE Australia. *Geochem. Geophys.* 18, 1-25. <https://doi.org/10.1002/2016GC006601>.

Renne, P. R., Deino, A. L., Hilgen, F. J., Kuiper, K. F., Mark, D. F., Mitchell, W. S., Morgan, L. E., Mundil, R., Smit, J., 2013. Time scales of critical events around the Cretaceous-Paleogene boundary. *Science* 339, 684-687. <https://doi.org/10.1126/science.1230492>.

Renne, P.R. Mundil, R. Balco, G., Min, K., Ludwig, K.R., 2010. Joint determination of ^{40}K decay constants and $^{40}\text{Ar}^*/^{40}\text{K}$ for the Fish Canyon sanidine standard, and improved accuracy for $^{40}\text{Ar}/^{39}\text{Ar}$ geochronology. *Geochim. Cosmochim. Acta* 74, 5349–5367. <https://doi.org/10.1016/j.gca.2010.06.017>.

Renne, P.R., Balco, G., Ludwig, K.R., Mundil, R., Min, K., 2011. Response to the comment by W.H. Schwarz et al. on "Joint determination of K-40 decay constants and Ar-40*/K-40 for the Fish Canyon sanidine standard, and improved accuracy for Ar-40/Ar-39 geochronology" by PR Renne et al. (2010). *Geochim. Cosmochim. Acta* 75, 5097-5100. <https://doi.org/10.1016/j.gca.2011.06.021>.

Renne, P.R., Swisher, C.C., Deino, A.L., Karner, D.,B., Owens, T.L., Depaolo, D.J., 1998. Intercalibration of standards, absolute ages and uncertainties in $^{40}\text{Ar}/^{39}\text{Ar}$ dating. *Chem. Geol.* 145, 117–152. [https://doi.org/10.1016/S0009-2541\(97\)00159-9](https://doi.org/10.1016/S0009-2541(97)00159-9).

Steiger, R.H., Jäger, E. 1977. Subcommittee on geochronology: Convention on the use of decay constants in geo- and cosmochronology. *Earth Planet. Sci. Lett.* 36, 359-362. [https://doi.org/10.1016/0012-821X\(77\)90060-7](https://doi.org/10.1016/0012-821X(77)90060-7).